ABSTRACT

LI, GANG. Probabilistic Damage Size Estimation for Structural Health Management. (Under the direction of Dr. F. G. Yuan).

Airframe structures encounter severe environments, fatigue cyclic loadings, and aging. Micro-defects in structures will nucleate macro-cracks and grow into catastrophic damages after a period of service. Structural health monitoring (SHM) and damage prognosis (DP) have attracted much interest for increasing the reliability and reducing the operative risks of aircraft structures. The SHM techniques are booming for years, while models from fractural mechanics have been applied for damage prognosis in many studies. Damage estimation from online SHM imaging results is mainly studied in this work and tries to fill the gap between the online damage detection and damage prognosis.

A damage image segmentation technique based on Bayesian updating framework is proposed for diagnosis and prognosis in the context of structural health monitoring (SHM). This framework takes into account the prior information of the conditions, e.g. spatial constraints and image smoothness. Markov random field is employed to model the prior due to the spatial constraint in the neighboring grids in SHM images. Results show that the Bayesian segmentation method has the potential to segment damage areas reasonably in SHM images and achieve more accurate damage sizes automatically than the conventional K-means clustering method through eliminating random noises and inhibiting the fuzzy edges. To enhance the image segmentation

by the online SHM detection, the previous detected images and multiple frequency excitations can be employed to achieve more reliable segmentation.

A morphological gradient prior enhanced three-step procedure for extracting a probability density function (PDF) of damage size from a damage image by an structural health monitoring (SHM) system is proposed for providing reliable and comprehensive information about the damage using probabilistic concept. This procedure can fill the gap between damage imaging and damage prognosis. The results can also implicate the accuracy and precision of various damage imaging techniques. Compared to conventional deterministic damage quantification methods, such as threshold crossing, the advantage of the proposed method is that it provides the probability of all possible damage sizes. Since damage size is given as a probability distribution, the failure is defined as a probability of damage being larger that the pre-defined critical damage size. Several examples are presented and compared to illustrate the validity of the proposed PDF extraction method. Results show that the PDF generated reflects not only the most likely damage size but also the confidence of the estimation. The damage prognosis is carried out to obtain the remaining useful life (RUL) to verify the damage estimation procedure, and an improved diagnosis by prognosis model is proposed to reduce the uncertainty of detection based on the previous detections.

Probabilistic Damage Size Estimation for Structural Health Management

by
Gang Li

A dissertation submitted to the Graduate Faculty of
North Carolina State University
in partial fulfillment of the
requirements for the degree of
Doctor of Philosophy

Mechanical Engineering

Raleigh, North Carolina

2011

APPROVED BY:

Dr. Fuh-Gwo Yuan Committee Chair	Dr. Gregory D. Buckner
Dr. Kara Peters	Dr. Murthy N. Guddati

DEDICATION

To my parents

and

my wife Hanlei

BIOGRAPHY

Gang Li was born in Danyang, Jiangsu province, the People's Republic of China on August 12th, 1980. He graduated from Danyang Advanced High School in 1998, received Bachelor degree in Electrical Engineering and Automation from Nanjing University of Aeronautics and Astronautics in 2002, and achieved Master degree in Measurement and Instrument Engineering from Nanjing University of Aeronautics and Astronautics. Since then he continued his research at the Aeronautical Key Laboratory for Smart Materials and Structures. From August 2007 till now, Gang Li worked for his doctor of philosophy degree in the Mechanical Engineering department at North Carolina State University. In the summer semester of 2008, he worked as a research scholar in the Structural & Multidisciplinary Optimization Group in Mechanical Engineering department at University of Florida.

ACKNOWLEDGMENTS

First and foremost I offer my sincerest gratitude to my advisor, Dr. Fuh-Gwo Yuan who has supported me throughout my study and research at NC State from 2007. I very appreciate his patient guidance and enthusiastic encouragement throughout the work. Especially, his insight into cross-disciplinary research and his insistence of pursuing excellence in research influenced me greatly and surely my future academic career will benefit much from that.

I would like to thank all my committee members, Dr. Gregory D. Buckner, Dr. Kara Peters, and Dr. Murthy N. Guddati for their generous help and suggestions in completing this work. I very appreciate the research advice and paper revision from Dr. Raphael T. Haftka and Dr. Nam-Ho Kim from University of Florida.

I also appreciate the support of the project from which my graduate studies were funded. This work was sponsored by U.S. Air Force under Grant FA9550-07-1-0018 and NASA under Grant NNX08AC334.

I would like to express my appreciation to all my colleagues in the Smart Structures and Materials Lab, for providing me help on theoretical modeling, hardware problem solving and etc.

Finally, but not least, I would like to thank my whole family providing me the time, the mental support. Without their considerable understanding, I could never reach so far.

TABLE OF CONTENTS

LIST OF FIGURES

LIST OF TABLES

1 Introduction

1.1 Integrated Structural Health Management System

Airframe components are facing an indispensible issue of the fatigue failure, however it has been demonstrated that the structure can maintain a specific residual strength and be safe for a certain period of usage after a certain severity of damage[1-3]. Integrated structural health management(ISHM) systems with sensors permanently mounted (or embedded in) the structures, data acquisition system, damage identification, and damage prognosis algorithms, have significant impacts on enhancing aviation safety as well as reducing the operating and maintenance costs of airframe structures by providing accurate damage estimation at an early stage to reduce or predict structural failure[4]. In the particular case of the USA Army helicopter fleet, fatigue-critical parts only serve an average of roughly 25% of their designed life before replacement under the current damage allowable[5]. Furthermore, on-line ISHM systems allow estimations of the structure's health status and predictions of the remaining useful life (RUL) without off-line intrusive procedure and time consuming inspections. It is shown that increasing the average replacement interval from 25% to 33% of the design life limit would result in approximately 25% downtime and replacement cost reductions[5]. By advancing the state-of-the-art technology in on-board health state assessment strategy through the concept of condition-based maintenance, ISHM reduces life cycle costs through significantly prolonging the average life of the structures[6], since it identifies a small percentage of high-risk structural components that currently force conservative scheduled maintenance on all structural components.

On-line damage diagnostics module, a vital part in the structural health management system, bases on dynamic processes through the inspection of early damage detection. And damage prognosis process is carried out to estimate the health status and remaining useful life based on those modules[7-8]. Each stage introduces uncertainty into the system because of the sensor data noises, modeling errors, and material and geometric properties[9]. Therefore, a probabilistic framework is introduced to increase the efficiency of the design and implementation of structural health monitoring (SHM). Furthermore, with continual information flow extracted from the raw sensor data measurements on the structural components about damage initiation and damage propagation, a probabilistic framework should allow an SHM system to keep improving the accuracy and precision of both damage diagnosis and prognosis[10]. This will be accomplished by progressively narrowing the distributions of crack locations and sizes, as well as material properties that govern damage propagation, and hence RUL for structural components[11-13]. In essence, SHM systems transform each aircraft into a flying fatigue laboratory that continually improves the accuracy of the damage propagation modeling, damage estimation, and remaining useful life prediction.

Although structural health management system has been under intensive investigated for years, there are still issues and challenges to be resolved[14]. Following lists several of them from the angle of damage detection, damage estimation, and damage prognosis:

1) Sensing (What to measure, and how to measure)
    a. Densely-distributed, fault-tolerant sensing technology[15];
    b. Measurement of local response or global response[16-17];
    c. Information and properties of the sensing systems.
2) Data interrogation
    a. Signal filtering and fusion[18];
    b. Model compression and updating[19];
    c. Large-scale data management and deployment[20].
3) Predictive modeling and damage evolution
    a. Evolution of micro-scale damage initiation[21];
    b. Modeling over varying time scales[22-23];
    c. Quantify uncertainty in predictions.
4) System integration & deployment
    a. Requirement updating[24];
    b. Data fusion and optimization[25];
    c. Hardware and software development.

1.2 Damage Diagnosis

1.2.1 Damage Detection

The implement of a damage detection and characterization strategy for aircraft structures is referred to as Structural Health Monitoring (SHM)[26]. Damage can be defined as changes of the material and/or geometric properties of a structural system, including the changes of the boundary conditions and system connectivity, which adversely affect the response of the detected structure/system[27]. The SHM process involves the observation of a system over time using periodically sampled dynamic response measurements from sensors [28] or sensor arrays[29-34], the extraction of damage-sensitive features from these measurements, and the data analysis of these features to determine the current state of system health. For long-term SHM, the output of this process is the periodically updated information regarding the ability of the structure to perform its intended function in light of the inevitable aging and degradation resulting from operational environments. After extreme events, such as bird hitting or blast loading, SHM is used for rapid condition screening and aims to provide, nearly in real time, reliable information regarding the integrity of the structure.

Generally, for the purpose of on-line structural health monitoring, damage detection system can be constructed by following elements,

1) Structures to be monitored;
2) Sensors or sensor arrays;
3) Automatic controlled data acquisition systems;

4) Data pre-processing and data fusion;

5) Graphic user interface.

In this study, damage imaging techniques focus on detecting damages on plate-like structures. Among the versatile sensing and damage characterizing techniques, ultrasonic Lamb wave based damage imaging provides high confidence of detection[35-38], which not only reflects the damage location, damage size, but also damage severity and probabilistic information. The damage estimation study in Chapter 2 and damage prognosis study in Chapter 4 are based on damage imaging results.

Lamb wave is one of the elastic waves whose particle motion lies in the plane defined by the plate normal and the direction of wave propagation. As early as 1917, Lamb [39] firstly published his classic analysis of this type of waves. In an infinite medium, there are two wave modes traveling at their unique velocities, but plates have two infinite sets of Lamb wave modes, whose velocities depend on the dispersion relationship between wavelength and plate thickness. Figure 1-1 shows the calculated group velocity dispersion relationship on an aluminum plate. The solid lines represent anti-symmetric modes, and the dash lines represent symmetric modes.

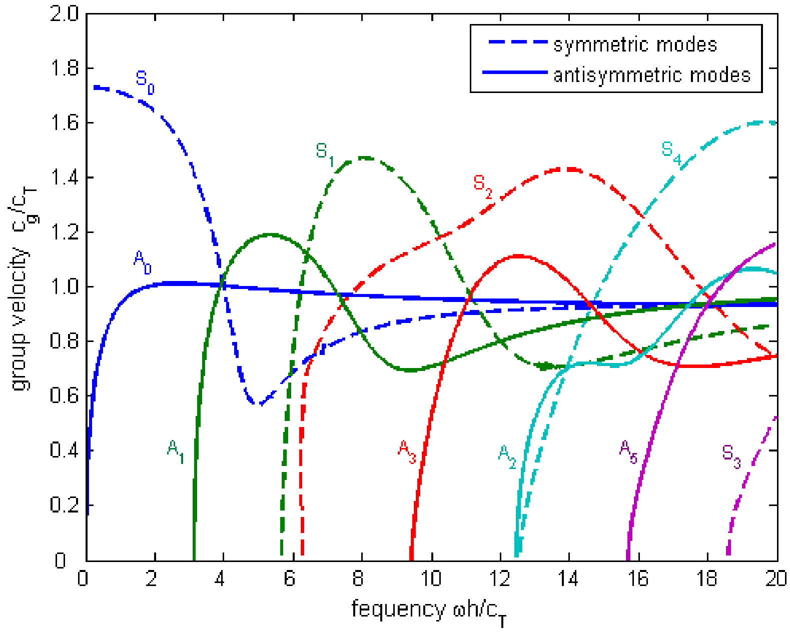

Figure 1-1. Group velocity dispersion of Lamb waves on an aluminum plate.

In addition to damage location, both damage size and damage shape are also desirable in structural health monitoring. Damage imaging becomes popular in indicating comprehensive information of the damage in structures. Ultrasonic Lamb wave method based on piezoelectric sensors and combined with versatile algorithms for imaging provides great window in damage recognition[31, 40-42]. Since the damage image itself is intuitively a 2D distribution function, the damage estimation can be applied to the damage image to evaluate the damage severity. For the purpose of damage prognosis the remaining useful life of the structure can be estimated based on the damage estimation[43]. Much attention has been paid to the damage imaging for plate-like structures using lamb waves. Several techniques are used to determine the size of the damage in finite size aluminum plates and integral stiffened composite structures in real-time from linear or distributed sensor/actuator arrays. The plates are usually installed with piezoelectric sensors bonded on one side of the plate, with one of the PZTs used as an actuator and excited by a narrowband tone-burst signal[44]. The integral formulation is first derived for the scattered wave based on Mindlin plate theory.

Lamb wave detecting is usually considered preferred in scanning large size structures, because it travels long distance along a plate or shell structure with no need to change the position of the sensors during the inspection. Built-in transducer systems consisting of PZT sensor array, which is used to excite Lamb wave in the waveguide (such as plate, shell and rod) for onsite structural monitoring make a structure smart. Quantifying the size, shape and severity as well as the location of the damage in plate or shell like structure is regarded as one of the most important tasks in NDT before the structure fails to perform its intended function. The most convenient way for a non-technician to check the security property of a structure is to inspect the health status image, which can directly show essential information and singular change in the detected structure. In the past twenty years, lots of researchers from various countries and research areas have devoted to signal processing and imaging processing of plate-like or shell-like structures in the NDT area. Yu *et al.* [33] employed phased array and tomography algorithm in order to obtain the damage image of an aircraft structure. Lin and Yuan [45] used finite difference method and the migration technique to image the damage and show its validity for diagnosing composite plates. Cassereau and Fink[46-47] established the TRM principle and developed a numerical method called DORT to separate point-like scattering sources in solid and liquid structures. Park *et al.*[48] introduced the time reversal concept into the waveguide structure and employed damage index in order to detect discontinuity in civil and aerospace structures. Jill and Mark[49] used nearly 200 sensors and a precise controlled step motor system to detect the plate-like aircraft structure by Lamb wave tomography. Most of above imaging methods provide reasonable results and acceptable resolution, however, they use intensive sensor array which is not suitable for practical situations where the aircraft is in service.

There are various types of sensor arrays that have been employed for damage imaging of plate-like structures. Two of them typically are linear sensor array and distributed sensor array, each of which holds their own advantages and disadvantages.

Figure 1-2 shows the demonstrative topographies of the linear sensor array and distributed sensor array.

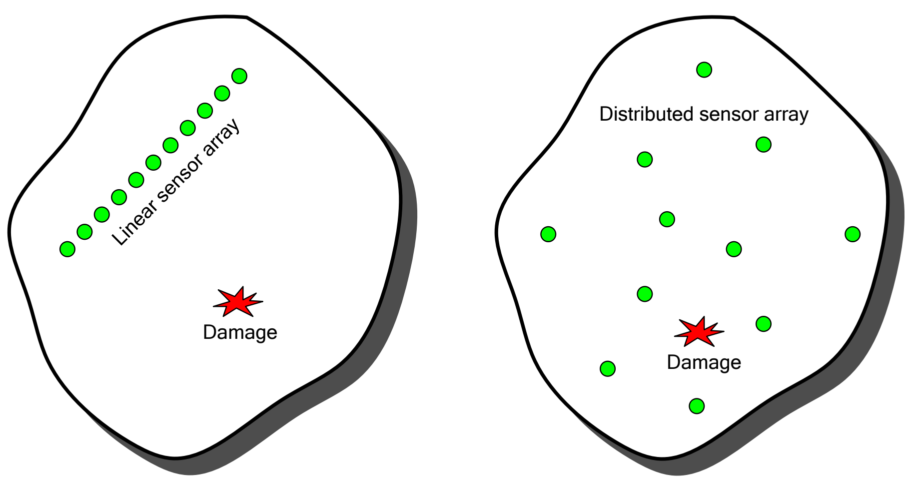

Figure 1-2. Illustration of a linear sensor array and a distributed sensor array.

For linear sensor array, sensors may be mounted on one side of structures, or one surface of the structures, and it is especially convenient for applications where the structures are non-invasive, however, because the sensors are mounted on one side of the damage, the imaging results may have fuzzy shadows caused by the non-symmetric sensor distribution. For the distributed sensor array, sensors are distributed installed. As the number of sensors increases, the distributed sensor array can be seen as omni-orientated. Especially when combined with the time reversal method, distributed sensor arrays can be applied to very complex structures, such as non-even density structures, non-even thickness plate, or structures with non-regular holes.

Algorithms, introduced from other similar imaging applications, such as medical imaging, satellite imaging, and geometric imaging, and etc. are successfully employed by researchers in NDT area, including computed tomography (CT) imaging, time reversed (TR) imaging and migration imaging.

Computed tomography imaging is originally used for medical imaging. Lamb wave tomography has been used successfully in a number of applications ranging from material loss detection to borehole detection. The work to date has been primarily undertaken with contact transducers, air-coupled transducers, immersion transducers, and laser ultrasound. Significant work has also been published on Lamb wave, pipe inspection applications. Researchers show that tomography imaging with limited sensors for SHM can generate images from which the existence of damage can be determined, but it is hard to obtain accurate damage images for accurate damage size estimation.

The time-reversal technique developed by Fink and his group[50] has been widely applied in different disciplines such as medical imaging, ocean sonar imaging, and nondestructive evaluation. Generally, in time reversal acoustics, a series of signals, which are the responses of a source propagating in some kind of structure/medium, are recorded by an array of sensors, time reversed and then re-emitted into the structure at the responsive points. The re-emitted signal propagates back through the same structure/medium and refocuses on the source point. The imaging technique using time reversal concept in acoustics/ultrasonic has been adapted to wave propagation to improve the detection of the defects or discontinuity in liquid and solid materials to overcome shortcomings of other imaging methods.

Migration technique identifies multiple damages in plate-like structures in real time using scattered Lamb waves. Based on Mindlin plate theory, migration algorithm for dispersive flexural wave is deduced. Combined with the time-coincidence imaging condition, damages are imaged by performing cross-correlation to the extrapolated scattered wavefields and excitation wavefields. Numerical simulation study employs an explicit finite difference method to generate synthetic scattered wavefields with damages of different shapes and sizes in the structure. Imaging results for the synthetic wavefields demonstrate that the proposed method has the capability of not only localizing multiple damages but also identifying their sizes; its advantage of fast calculation meets the requirement of real-time damage identification for an on-line structural health monitoring system. The details of the migration based imaging for structural health monitoring were fully studied by Lin and Wang. The damage estimation of this work is based on the images by migration techniques due to the high quality and real-time availability.

1.2.2 Damage Estimation

Damage estimation refers to evaluate the quantification of damage from the damage detection result, such as direct measured data or processed data (e.g. filtered signals, decomposed components or constructed images). The SHM system can be performed continually during the aircraft service although the resolution is generally not as high as traditional offline NDT inspections. Incorporating the continual information from sensor data, a damage propagation model can be employed to assess the structure's condition, predict the damage propagation with the pre-assumed loading, and finally estimate the remaining useful life. The study of damage estimation from the intensity images in a plate fills the gap between the damage image and prognosis.

The damage estimation in this work mainly focuses on the SHM imaging results, extracting damage information from the images with a certain imaging algorithm. The main principle of SHM imaging is to adopt an adaptive or matched filter on the signal array from the sensor networks. A 2D intensity image displayed by the brightness of the pixels provides a probabilistic distribution of damage severity in the structures to be monitored. Although there has been ever-increasing demand in achieving higher accuracy of damage imaging using advanced diagnostic techniques with the latest instruments on the ground under laboratory controlled environments, it is always desirable to size the damage with an on-line SHM system. With the restriction of space, weight, instrumental and environmental complexity involved, the accuracy and precision of the SHM system is usually still not as good as desired. Continual damage imaging by the SHM system accumulates and updates information, which can be fused into more reliable knowledge of the monitored structures.

In SHM, various imaging techniques have different degrees of precision and accuracy [51] in terms of damage severity as shown in Figure 1-3. Even with the same hardware, different excitation configurations (e.g. waveforms and frequencies) may lead to images with various resolutions. The resulting on-line SHM imaging can be more complicated due to the noisy environments, leading to the changing of the probability of detection (POD)[52]. Therefore, a probabilistic estimation of the crack sizing for damage propagation law is indispensible for enhancing the confidence of damage prognosis and providing more comprehensive information.

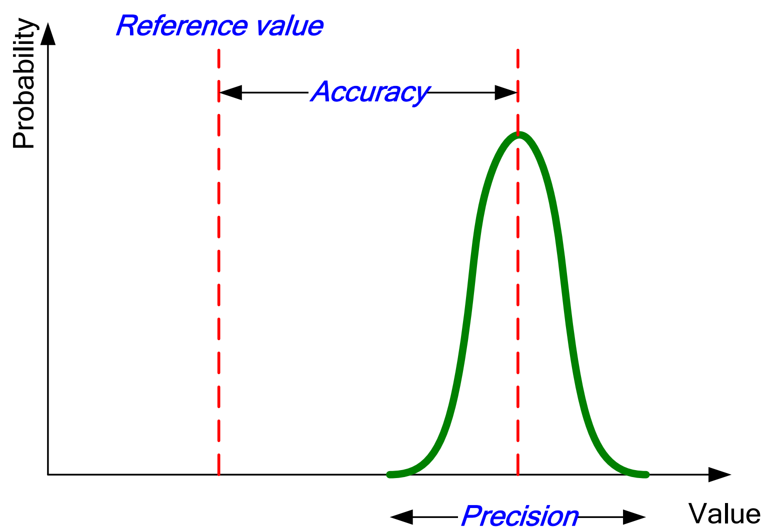

Figure 1-3. Illustration of accuracy and precision in error theory.

While damage diagnosis is concerned with detecting and quantifying the damage in the structure; damage prognosis based on the damage estimation focuses on developing a reliable and accurate damage propagation model for RUL. Damage estimation, which quantifies the damage size, is one of the most important issues in SHM. Various methods have been applied in damage estimation, such as damage index[53], signal difference coefficient[34], as well as image-based techniques, such as threshold crossing [34] and Bayesian based image segmentation[44]. Damage evaluation can be broadly categorized into the following three levels as listed in Table 1-1: (1) damage detection, (2) deterministic damage estimation, and (3) probabilistic damage estimation. Damage detection is the lowest level, which determines whether damage exists or not. Deterministic damage estimation gives the damage location or damage size. Probabilistic damage estimation not only gives the damage location and damage size, but also the probabilistic information of the damage location and damage size. This third level estimation will be the focus of this work, providing probabilistic damage characterization based on SHM images.

Table 1-1. Three levels of damage estimation.

Level	Name	Results	Features
I	Damage Detection	Yes / No	• Determine if there is a detectable damage in the structure
II	Deterministic Damage Estimation	Damage location: (x, y) Damage index: I Damage size: L	• Determine the damage index reflecting the damage severity • Determine the damage location • Determine the damage size
III	Probabilistic Damage Estimation	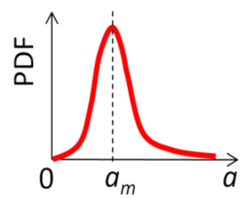	• Estimate the PDF of damage size • Give the most probable damage size • Give the probability of damage more or less than a given size, generally the critical size. • Give the probability of damage at a given location

For different damage detection techniques, there are various types of damage estimation methods developed[54-57]. While considering the issues of damage size estimation, the following questions need to be answered.

1) How much is the uncertainty of estimation?

   a. The dispersion (deviation) of the estimation[58],

   b. The confidence of the conclusion[59-60].

2) Where does the uncertainty come from?

   a. SHM hardware system[24],

   b. Data processing algorithm, or imaging algorithms[61],

   c. Loading, environmental noise and disturbance[60].

3) How to reduce the uncertainty?

   a. Improve or update detecting system,

   b. Improve damage estimation algorithm,

   c. Introduce data fusion technique.

In one word, high quality of damage estimation originated from high quality images/damage detection leads to reliable structural estimation and prediction. Comprehensive damage estimation should not only contain damage size, damage location, but also the probability of damage size equaling to a given possible size. Further information, such as the probability of damage at a given location, could also be characterized.

The damage estimation is the main focus of this dissertation. In section 2.1, an improved histogram analysis method is developed to determine whether the image from an on-line SHM system includes damage or not. In section 2.2, a Bayesian-based image segmentation with Markov random field (MRF) as a prior information is introduced in theory and applied to damage images from numerical damage imaging results. It is true that at the second level, the probabilistic concept is included in the analysis; however, the segmentation result is still a deterministic result. In Chapter 3, a probabilistic crack sizing method is developed to extract more comprehensive information about the damage in images.

1.3 Damage Prognosis

1.3.1 Motivation for damage prognosis

It is known that airframe structural components subjected to large stresses and elevated temperature during operation can develop flaws due to material fatigue. These flaws grow with time, and if undetected in time, may cause catastrophic failures[62]. Thus it is critical to monitor flaws within airframe structural components at high-stress or flight-critical areas. Cyclic loadings (including stress and thermal variation) applied on the engineering structures may cause inbred micro-defects to nucleate macro-cracks, and those existing cracks to propagate. The initiation and propagation of fatigue cracks may lead to the failure of structural components at loads below design levels, reducing their useful life.

Structural components undergoing fatigue loadings can be divided into two categories based on their cyclic loading environments: (1) Dynamic components, and (2) Airframe components[63]. On the one hand, Dynamic components are subjected to high-frequency, low-amplitude loading during all operations of the aircraft, and examples include shafts, drive-train components, and rotor parts. On the other hand, the load spectra of airframe components are dominated by higher-amplitude, non-vibratory loads, such as taking-off and landing cycles. The useful life of a dynamic component is dominated by the crack initiation process, whereas crack propagation occupies a larger part of an airframe component's lifetime. This is the reason why people pay much attention to the remaining useful life under the fatigue loading of the airframe structures.

Figure 1-4 illustrates the potential benefits using structural health monitoring and damage prognosis. Design life without SHM is dictated by a small number of structures at high-risk due to severe usage or damage incidents. Among other benefits, SHM can not only identify high-risk aircraft but also significantly prolong the average life of structural components.

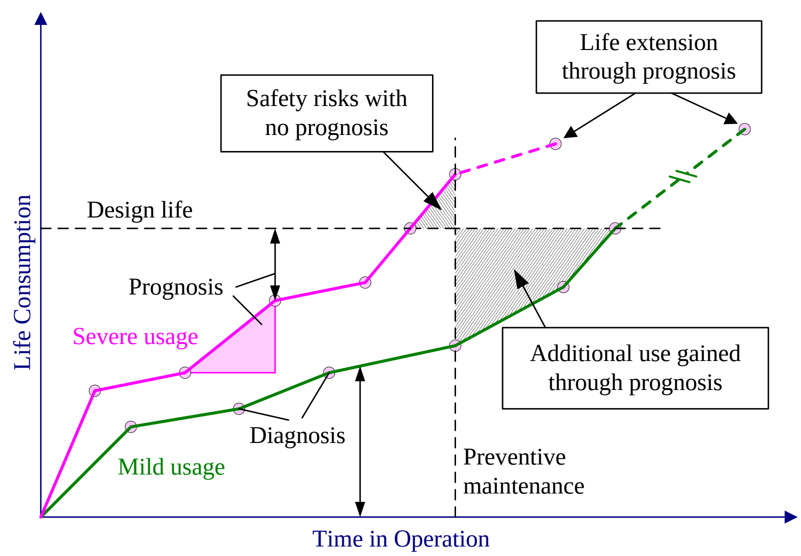

Figure 1-4. Potential benefits using SHM.

Materials or structures used in engineering systems have some inherent initial flaws at various levels[63]. For airframe structures with many components, micro-flaws may coalesce and grow to the level where they produce component level failure under appropriate loading[64]. Further loading may cause additional component failures which can lead to airframe failure[65]. In some cases this evolution or damage propagation may occur over relatively long time scales though the form of corrosion or fatigue crack growth. Other cases cause the damage evolution to dangerous level in relatively short time scales (e.g. earthquake loading[66], and impact-related damage[67]). So we must consider both the damage size scale and time scale associated with the damage initiation and evolution. To provide a basis of this work, the fundamental consensus of structural health management is given as the following:

1) All materials and structures have inherent flaws or defects;
2) The assessment of damage requires a comparison between two system states;
3) Identification of the existence and location of damage can be done in an unsupervised learning mode, but identifying the type of damage present and the damage severity can generally only be done in a supervised learning mode;
4) Sensors cannot measure damage. Feature extraction through signal processing and statistical classification is necessary to convert sensor data into damage information;
5) Without intelligent feature extraction, the more sensitive a measurement is to damage, the more sensitive it is to changing operational and environmental conditions;
6) The length scale and time scale associated with damage initiation and evolution dictate the required properties of the SHM sensing system;

7) There is a trade-off between the sensitivity to damage of an algorithm and its noise rejection capability;
8) The size of damage that can be detected from changes in system dynamics is inversely proportional to the frequency range of excitation.

1.3.2 Probabilistic Damage Prognosis Procedure

Probabilistic concepts have long been introduced in fatigue analysis for damage prognosis. Due to the uncertainty of measurement and testing, damage qualification algorithm and parameters of damage propagation models, it is almost impossible to predict damage deterministically in practice. Various probabilistic methods have been developed to analysis damage prognostic procedure. Lin and Yang [10] obtained the analytical expression for probability distribution of crack size at any given time and the probability distribution of the time at which a given crack size is reached, based on the knowledge of the initial crack size. Achenbach's group [68] developed a probabilistic procedure to predict the macro-crack initiation and calculated a probability of detection (POD). Coppe *et al*. [11]applied a Bayesian based method to narrow the distribution of the material parameters in Paris law. A kernel-based Gaussian random process was used for the time series prediction of fatigue crack growth function under variable loading by Mohanty *et al*.[69]. However, these methods started with a pre-assumed probabilistic model or based on a large amount of data from time and costly experiments. The purpose of this paper is to use the online SHM system to provide probabilistic estimation, and enhance the estimation and prediction.

There are mainly two types of models used in the damage prognosis process, physics-based modeling and data-based modeling[70-73]. The damage prognosis process begins with collecting as much initial system information as possible including inspection and analyses which are carried out during period of the structure design, service, and maintenance.

What is collected from the inspection and analysis can be used to initialize physics-based models of the structures[73]. The physics-based models will also be used to define the necessary sensing system properties, i.e. the resolution of the detecting system. The physics-based models can be used as a part of an optimization study that will maximize the utilization of collected signals from SHM system. As further data are collected by the SHM system when the structure is in service, they are going to be used to update the physics-based models again. These data and the output from the physics-based models can be used to apply to structural health monitoring, providing information such as the geometry, boundary condition, material properties and etc. Data from the operational and environmental sensors can be used to develop and update data-based models to predict the future structural performance[11]. The statistical loading model, damage detecting system model, and the physics-based model can be put into a reliability-based predictive model that estimates the remaining useful life of the structures[73]. This combination of physics-based and data-based models is the essential feature of an integrated structural health management system rather than a previous defect inspection system.

1.4 Summary

The main content in this work is covered in Chapter 2 through Chapter 4 based on damage detection with ultrasonic imaging method. The damage identification is investigated in Chapter 2. A probabilistic damage sizing will be developed in Chapter 3 and followed by the damage prognosis part in Chapter 4.

In Chapter 2, three levels of damage estimation are introduced based on the damage imaging technique. Three types of damage estimation techniques are developed in this chapter to quantify the damage in the damage images. At low level, an improved histogram-based damage identification method is developed to make a decision whether an image contains damage or not. At medium level, a Bayesian-based image segmentation method is developed to segment damage area from the background. Probabilistic concept is involved in the procedure to calculate the probability of each pixel belongs to the damaged class or undamaged class. However, the result of image segmentation is the clusters, which means the final result is deterministic. Therefore, Bayesian-based image segmentation achieves optimized damage size with Markov random field and other prior information. At the high level, a 3-step procedure is developed to extract more comprehensive information of the damage from the image. The result can indicate the probability of damage size equal to any possible size. An improvement is also carried out for the original 3-step procedure, and narrows the resultant distribution by introducing morphological gradients as a prior, which results in a narrow distribution with high precision.

In Chapter 4, a basic damage propagation model, Paris law, is introduced to simulate the damage growth on an aluminum plate. Distribution of remaining useful life can be achieved based on the probabilistic damage estimation discussed in the Chapter 2. From the distribution of remaining useful life, the probability of the structure failing until a given moment can be calculated. Bayesian updating is employed to combine the prior information with the new data, achieving more reliable estimation and prediction.

Chapter 5 concludes the work on damage estimation and damage prognosis. Future work is recommended based on current studies for the future researchers.

2 Damage Identification

2.1 Histogram Based Damage Identification

Once the images are obtained from the on-line structural health monitoring (SHM) system, the first task is to detect whether the image contains damage or not. If the image contains damage, further analysis needs to be carried out to estimate the damage severity, damage size or damage region. If the image does not contain damage, the on-line SHM system should continually inspect the structure periodically until the detectable damage appears. Therefore the three levels of damage estimation mentioned in Chapter 1 are not independent.

Since the intensity image of damage is a distribution of intensity value in a 2D space, statistical analysis can be carried out to determine if obtained images contain damage or not. Histogram analysis is a widely used image processing technique to reflect the statistical information of intensity values in the damage image. A histogram is a graphical display of tabular frequencies, shown as adjacent rectangles. Each rectangle is erected over an interval, with an area equal to the frequency of the interval. The height of a rectangle also equals to the frequency density of the interval, i.e. the frequency divided by the width of the interval. The total area of the histogram equals to the number of data.

2.1.1 Definition of Histogram

For a mathematical definition, a histogram is a mapping m_i that counts the number of observations that fall into various disjoint categories (known as bins), whereas the graph of a histogram is merely one way to represent a histogram. Thus, if n is the total number of observations and k the total number of bins, the histogram m_i meets the following conditions:

$$n = \sum_{i=1}^{k} m_i. \tag{2-1}$$

The number of bins k can be calculated directly, or from a suggested bin width h:

$$k = \left\lceil \frac{\max x - \min x}{h} \right\rceil. \tag{2-2}$$

2.1.2 Improved Histogram Analysis for Damage Identification

In a clean damage image without noise, if the close-up observation is carried out, the histogram will clearly reflect the existence of damage by the components indicating the damaged level. However, the noise-polluted images from SHM detection, such as the ones in Figure 2-1, do not hold these distinguishable features, because the noise in the overall domain will dominate the histogram, which makes the damage information weak compared with the noise environments. For some specific operation by randomly redistributing the aggregate light pixels as noise, the histogram of the damage containing noisy image can be exactly the same as the noisy image without damage. Figure 2-3(a) gives the histogram analysis of the whole noisy images with and without damage. It is almost impossible to distinguish the damaged one from the undamaged one. Figure 2-3(b) gives the close-up histogram analysis, which is better for reorganization from each other, but the difference is still not clear. An improved histogram analysis, by carrying out an averaging filter with neighboring system information, is designed to examine the existence of damage. Figure 2-2 shows the framework of this improved histogram analysis procedure. The essence of this procedure is to introduce a spatial neighbor system as a filter before histogram analysis. The comparison shown in Figure 2-3 (c) indicates that the improved image histogram analysis can effectively detect the damage in the image with distinguishable feature.

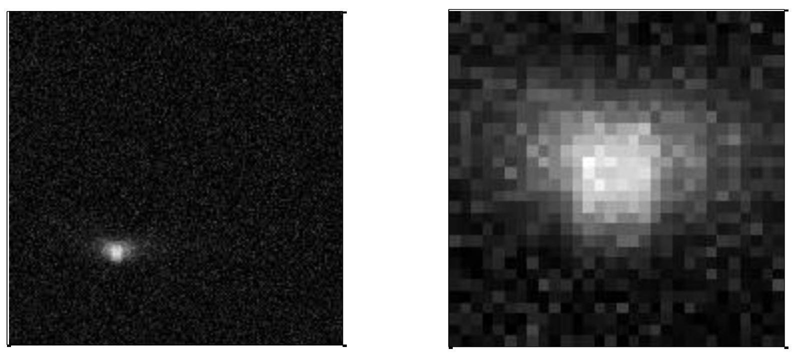

(a) Noise polluted image with damage and the focus-up area

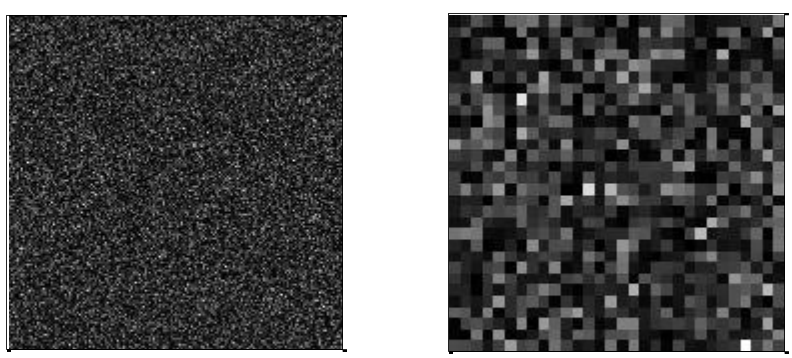

(b) Noise polluted image without damage and the focus up area

Figure 2-1. Noise polluted images with damage or without damage.

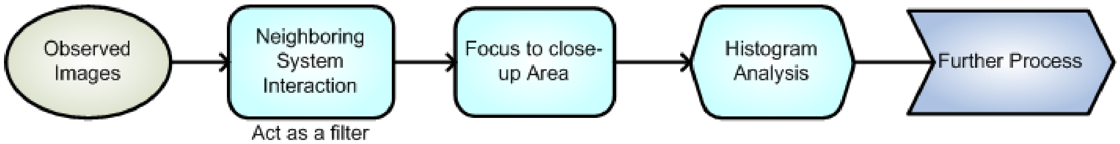

Figure 2-2. Framework of improved histogram analysis.

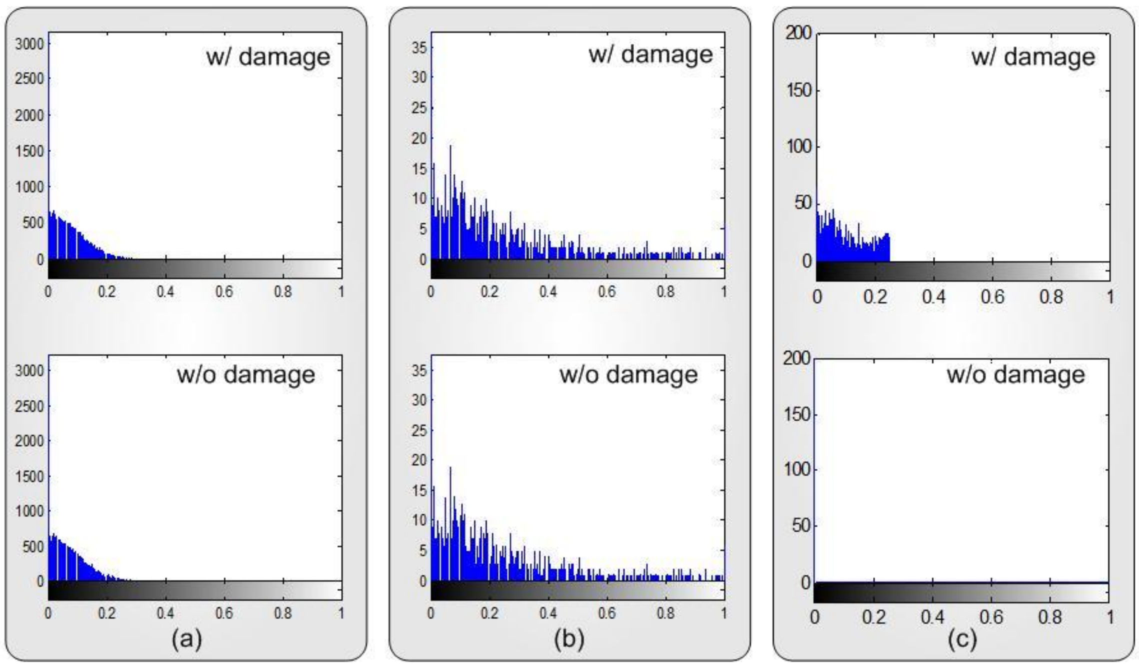

Figure 2-3. (a) Histogram, (b) close-up histogram, and (c) improved histogram.

The procedure of the first level of damage estimation is much simpler than the poster complex damage estimation, but it is important. This procedure should be carried out before any further estimation.

2.2 Image Segmentation based on Bayesian Statistics

Image segmentation refers to the process of partitioning an image into multiple regions with different class labels. The goal of segmentation is to simplify the representation of an image into a class of certain representations, each of which holds distinct attributes. Researchers have developed many methods based on clustering concepts such as fuzzy mathematics, neural network, and statistical models[74-82]. Bayesian based segmentation is one viable approach[74], which takes advantage of a statistical model to combine the current observed data with prior knowledge, such as spatial constraints and smoothness level.

Aircraft plate-like structures are prone to form damages, such as cracks, due to cyclic loads and severely corrosive service environments. Diagnosis and prognosis of damage are essential issues in structural health monitoring and management for preventing catastrophic failures and predicting the remaining useful life (RUL) of structures. Ultrasonic wave imaging with various forms of sensor array have the potential to detect the damage or abnormity on large-scale, complex plate-like structures. Damage location, shape and severity evaluation is one of the most important topics in SHM.

This section aims at estimating the damage region based on the images generated from migration imaging techniques. Since the size of the crack provides the essential information for structural health prognosis to estimate residual life of the structural component according to crack propagation law such as Paris law in metals, which relates stress intensity factor and crack growth to fatigue loading.

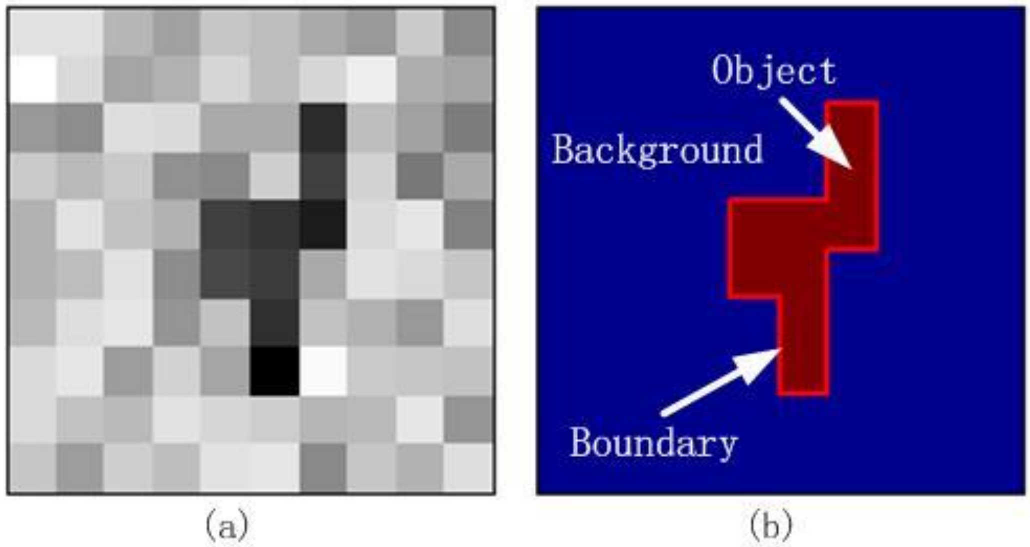

Figure 2-4. (a) An intensity image and (b) its binary segmentation.

Image segmentation is a branch of image processing, which separates the detected image into several meaningful regions with the same attributes, e.g., damaged regions/non-damaged regions, according to the image itself and some prior knowledge. Figure 2-4 shows a typical intensity image and its segmentation. Although well-trained human with experience can identify the segmented regions from the observed image, it is not an easy task for a computer to automatically divide an observed image (especially noisy images with fuzzy information) into meaningful regions. Image segmentation based on statistical models has been well developed in medical image analysis [82] and computer vision[83]. Bayesian updating framework used for image segmentation is introduced to merge the observed image data with the prior knowledge, e.g. spatial constraints, strength and distribution of disturbance, to achieve more reliable segmentation results than those obtained using simple image segmentation method like thresholding and *k*-means clustering as given in Appendix.

Image segmentation has been fully developed for medical image procession, however, the service environments and specific aircraft structures lead to the following three main properties of the detected images using ultrasonic waves when compared to medical imaging technique for human bodies. First, the large scale of aircraft structures and on-line diagnostic require relatively low density of sensor distribution. Second, severe variations of temperature and humidity during the in-flight service impact the dynamic response of detected structures. Third, due to noises, electromagnetic disturbances and random events from the environment and the SHM system itself, the imaging results from the ultrasonic wave based diagnosis are always of relatively low quality. It is difficult for the traditional image segmentation to effectively separate the damage region from the background. A reliable image segmentation method, which should be immune to noises and fuzzy tails in the SHM images, is imperative to obtain a meaningful segmentation and precise damage estimation.

In this section, an image segmentation method based on Bayesian updating with MRF is investigated to estimate damage region for plate-like structural health monitoring using ultrasonic guided Lamb wave detection. Basic probability concept to Bayesian updating and its application for image segmentation will be reviewed in section 2.2.1. MRF and Gibbs random field (GRF) acting as the prior information in the Bayesian updating framework will be introduced in the first part of section 2.2.2; how to model the image segmentation problem under the Bayesian updating framework, and how to quantify the image segmentation as a problem of maximizing a posterior (MAP) will be discussed in the second part of section 2.2.2. Section 2.2.3 gives the application of the Bayesian image segmentation method on migration images, and damage at multiple locations are given to illustrate the reliability of image segmentation. Further improvement of accuracy is achieved by carrying out multiple-frequency excitation in Bayesian updating framework in section 2.2.4.

2.2.1 Probability Basics to Bayesian Statistics

Recall the basic rules of probability for hypotheses, and let A and B be certain hypotheses. The notation $P(A)$ stands for the probability that A is true. The elementary rules of probability for simple hypotheses are:

$$0 \le P(A) \le 1, \tag{2-3}$$

$$P(\Omega) = 1, \tag{2-4}$$

$$P(A \cup B) = P(A) + P(B) - P(A \cap B), \tag{2-5}$$

$$P(A \cap B) = P(A|B)P(B) = P(B|A)P(A), \tag{2-6}$$

where Ω is the full set. $A \cap B$ is true only under the condition that both A and B are true, and $A \cup B$ is true as long as either A or B is true. $A \cap B$ can also be simplified as $'A, B'$ or AB (a logical product), while $A \cup B$ can also be simplified as $A + B$ (a logical sum). $P(A, B)$ is the joint probability of A and B, i.e. the probability that both event A and B occur. $P(A|B)$ is the conditional probability, i.e. the probability that A occurs given the assumption that event B occurs. Eq. (2-6) shows that the joint probability of two events can be decomposed into conditional probabilities in two different ways. Either way is called the product rule. If the status of B does not change the probability of A, and the other way around, then A and B are independent, probabilistically independent to be precise. In that case, $P(A|B) = P(A)$, and $P(B|A) = P(B)$, which, when substitute in Eq.(2-6), obtains:

$$P(A \cap B) = P(A)P(B). \tag{2-7}$$

Indicate the negation (or opposite) of A with $\bar{A}$, $A \cup \bar{A}$ is a full set, and $A \cap \bar{A}$ is an empty set ($A \cap \bar{A} = \varnothing$). The symbol $\varnothing$ stands for an empty set. Hence, the following can be obtained from Eq. (2-4) and (2-5):

$$P(A) + P(\bar{A}) = 1, \tag{2-8}$$

which indicates that hypotheses A is either true or not true.

Consider a set of hypotheses S_j that all together form a full set and are mutually exclusive:

$$\bigcup_i S_j = \Omega, \tag{2-9}$$

$$\text{and } S_j \cap S_i = \varnothing \text{ if } j \neq i. \tag{2-10}$$

When these conditions apply, the set {S_j} is said to form a complete class. The symbol S has been chosen because {S_j} as a set of hypotheses will be interpreted.

The first property of a complete class is the normalization,

$$\sum_j P(S_j) = 1, \tag{2-11}$$

which is just an extension of Eq. (2-8) to a complete class which contains more than just a single proposition and its negation.

For the complete class S, the generalizations of Eq. (2-8) and the use of Eq. (2-6) yield:

$$P(A) = \sum_j P(A, S_j), \tag{2-12}$$

$$P(A) = \sum_j P(A|S_j)P(S_j). \tag{2-13}$$

Eq. (2-12) is called marginalization, which becomes important when dealing with uncertain variables: the probability of A is obtained by the summation over all possible constituents contained in A. Hereafter, we avoid explicitly writing the limits of the summations, meaning that they extend over all elements of the class. The constituents are $'A, S_j'$, which, based on the complete class of hypotheses $\{S\}$, form a complete class, which can easily be proved. Eq. (2-13) shows that the probability of any proposition is given by a weighted average of all conditional probabilities, subject to hypotheses S_j forming a complete class, with the weight being the probability of the hypothesis.

In general, there are many ways to choose complete classes. Let us denote the elements of a second complete class by T_i. The constituents are then formed by the elements (T_i, S_j) of the Cartesian product $\{T\} \times \{S\}$. Eq. (2-12) and Eq. (2-13) then become the more general statements:

$$P(T_i) = \sum_j P(T_i, S_j), \tag{2-14}$$

$$P(T_i) = \sum_j P(T_i \,|\, S_j) P(S_j). \tag{2-15}$$

For a discrete variable x, the expression $p(x)$, which is a probability function, has the interpretation in terms of the probability of the hypotheses $P(A)$, where A is true when the value of the variable is equal to x. In the case of continuous variables, we use the same notation, but with the meaning of a probability density function. So $p(x)dx$, in terms of a proposition, is the probability $P(A)$, where A is true when the value of the variable lies in the range from x to $x + dx$. In general, the meaning is clear from the context; otherwise it should be stated. Probabilities involving more than one variable, like $p(x, y)$, have the meaning of the probability of a logical product. Table 2-1 summarizes several important definitions and formulae for discrete and continuous variables.

Bayesian updating is statistical inference in which evidence or observations are used to update or to newly infer the probability that a hypothesis is true. It uses aspects of the scientific inference, which involves collecting evidence that is meant to be consistent or inconsistent with a given hypothesis. As evidence accumulates, the degree of belief in a hypothesis should change.

In order to relate the observation y to the estimation x, the joint probability $p(x,y)$ is intuitively considered:

$$p(x, y) = p(x \,|\, y) p(y). \tag{2-16}$$

Table 2-1. Definitions and properties of probability functions.

	Discrete variables	**Continuous variables**
Probability	$P(X = x_i) = p(x_i)$	$dP_{[x \le X \le x+dx]} = p(x)dx$
Normalization	$\sum_i p(x_i) = 1$	$\int p(x)dx = 1$
Expectation of $f(X)$	$E[f(X)] = \sum_i f(x_i)p(x_i)$	$E[f(X)] = \int f(x)p(x)dx$
Expected value	$E(X) = \sum_i x_i p(x_i)$	$E(X) = \int xp(x)dx$
Moment of order r	$M_r(X) = \sum_i x_i^r p(x_i)$	$M_r(X) = \int x^r p(x)dx$
Variance	$\sigma^2 = \sum_i [x_i - E(X)]^2 p(x_i)$	$\sigma^2 = \int [x - E(X)]^2 p(x)dx$
Product rule	$p(x_i, y_j) = p(x_i \vert y_j)p(y_j)$	$p(x, y) = p(x \vert y)p(y)$
Independence	$p(x_i, y_j) = p(x_i)p(y_j)$	$p(x, y) = p(x)p(y)$
Marginalization	$\sum_j p(x_i, y_j) = p(x_i)$	$\int p(x, y)dy = p(x)$
Decomposition	$p(x_i) = \sum_j p(x_i \vert y_j)p(y_j)$	$p(x) = \int p(x \vert y)p(y)dy$

Then divide $p(y)$ at both sides of Eq.(2-16), it can be solved as,

$$p(x \mid y) = \frac{p(x, y)}{p(y)}. \tag{2-17}$$

As is known, the joint probability can also be represented as,

$$p(x, y) = p(y \mid x)p(x). \tag{2-18}$$

Substitute Eq. (2-18) into Eq.(2-17), we can get,

$$p(x \mid y) = \frac{p(y \mid x)\, p(x)}{p(y)}. \tag{2-19}$$

Thus we obtain the famous Bayes' equation. Bayes' equation [84] relates the posterior probability to the likelihood function, which is a conditional probability density function and the prior function which is a marginal probability for the events x and y.

In the Bayes' equation, $p(x)$ is the prior probability of event x before the observation. It is 'prior' in the sense that it does not take into account any information about the current observation y.

$p(x \mid y)$ is a conditional probability of x after the observation, given y. In Bayesian statistics, it is posterior probability because it is derived from or depends upon the specified value of y.

$p(y \mid x)$ is the likelihood, which is a conditional probability of y given x.

$p(y)$ is the marginal probability of y, and acts as a normalizing constant.

The following of this section shows an example to illustrate how Bayes' equation combines the current detected data with the prior information. The example is a source locating problem, which try to determine the location of the emitting source using the data collected from a sensor array.

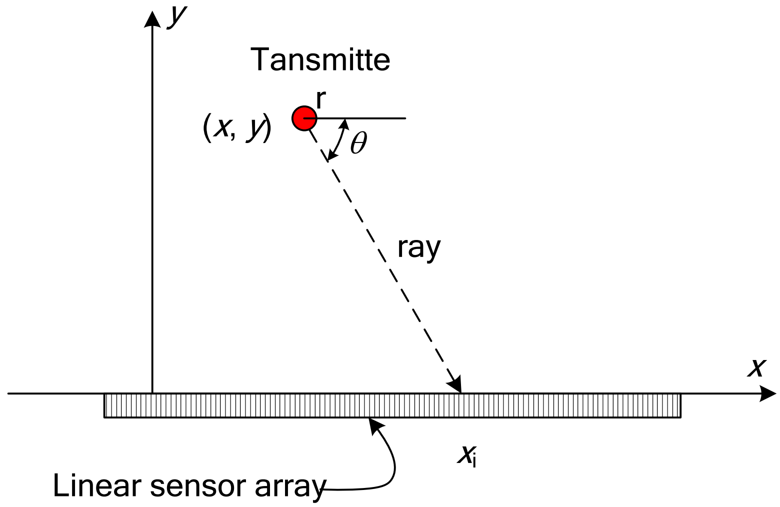

Figure 2-5. Example of estimating source location with Bayes' theorem.

Suppose that a transmitter is located at the position (x, y), as depicted in Figure 2-5. A position sensitive linear sensor array along the x axis, measures the position x_i that the i^{th} ray hits the sensor. The measurements consist of the values x_i, i = 1, ..., N. Assume that the probability density function for the emitting source is *uniform* in the angle θ at which they leave the source, so

$$p(\theta) = \frac{1}{\pi}. \tag{2-20}$$

The transformation property of probability density functions is described as shown in Eq.(2-21),

$$p(x) = p(u)\left|\frac{du}{dx}\right|. \tag{2-21}$$

From the geometry relationship,

$$\tan(\theta) = \frac{y}{(x_i - x)}, \tag{2-22}$$

$$\theta = \arctan\left(\frac{y}{x_i - x}\right), \tag{2-23}$$

$$\begin{aligned}\frac{d\theta}{dx_i} &= \frac{1}{1+\left(\frac{y}{x-x_i}\right)^2} \cdot \frac{-y}{(x_i - x)^2}, \\ &= \frac{-y}{y^2 + (x_i - x)^2},\end{aligned} \tag{2-24}$$

which holds for $-\pi < \theta < 0$, and the probability density function in x_i is obtained by substitute Eq. (2-24) and Eq. (2-20) to the transformation property of density functions in Eq. (2-24),

$$p(x_i \mid x, y) = \frac{y}{\pi\left[y^2 + (x - x_i)^2\right]}, \tag{2-25}$$

which is the likelihood of the event x_i. The likelihood for this problem follows a Cauchy distribution in x. The samples with Cauchy distribution (the source point is at (1, 1)) can be generated as the measurements.

The posterior probability density function for the x position of the source is given by Bayes's law. Let us suppose there is no prior information about the location of the source, then a constant for the prior $p(x)$ should be adopted. The measured x_i clearly follows the likelihood above, and as the emission of one ray cannot effect the emission of another, the x_i are statistically independent. Thus the full posterior probability is:

$$p(x \mid \{x_i\}, y) \propto \prod_i p(\{x_i\} \mid x, y) \propto \prod_i \left[\frac{y}{y^2 + (x - x_i)^2}\right]. \tag{2-26}$$

Two fundamental characteristics of Bayesian analysis can be identified. First, the calculation of the posterior probability is essentially a modeling effort based on the physical situation as we understand it. Second, the evaluation of the posterior probability proceeds through the model in a forward direction; one starts with assumed values of the parameters and predicts the measurements. Therefore, the numerical values of the posterior probability are often easy to calculate even when the model consists of a sequence of stages.

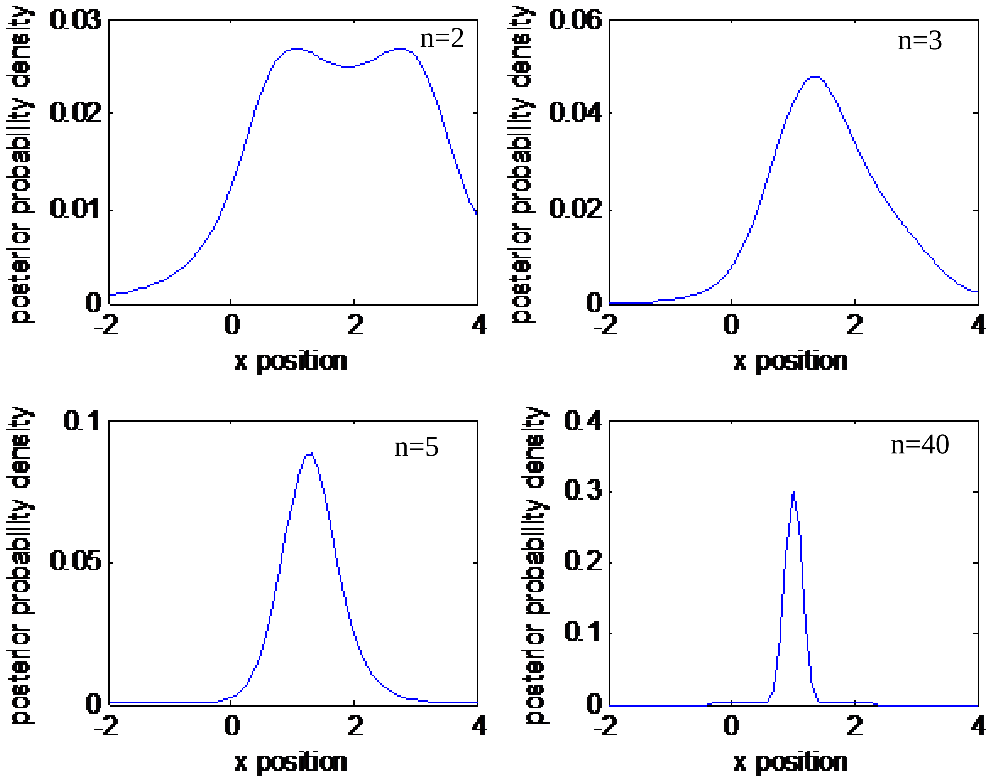

Figure 2-6. The posterior probability density function for the *x* position.

The posterior probability given by Eq. (2-26) is plotted in Figure 2-6 with specific numbers of measurements. The plot for two measurements is bimodal as shown in Figure 2-6(a), making it difficult to use the maximum posterior probability as an estimator for *x*. As the number of measurements increases, the width of the posterior density function decreases, indicating less uncertainty in the knowledge of *x*. The broad tail of the Cauchy likelihood is suppressed as the number of measurements increases because the posterior probability involves a product of likelihoods. As the measures accumulate, the estimated emitting source location in *x*-direction converged to the true source location 1.

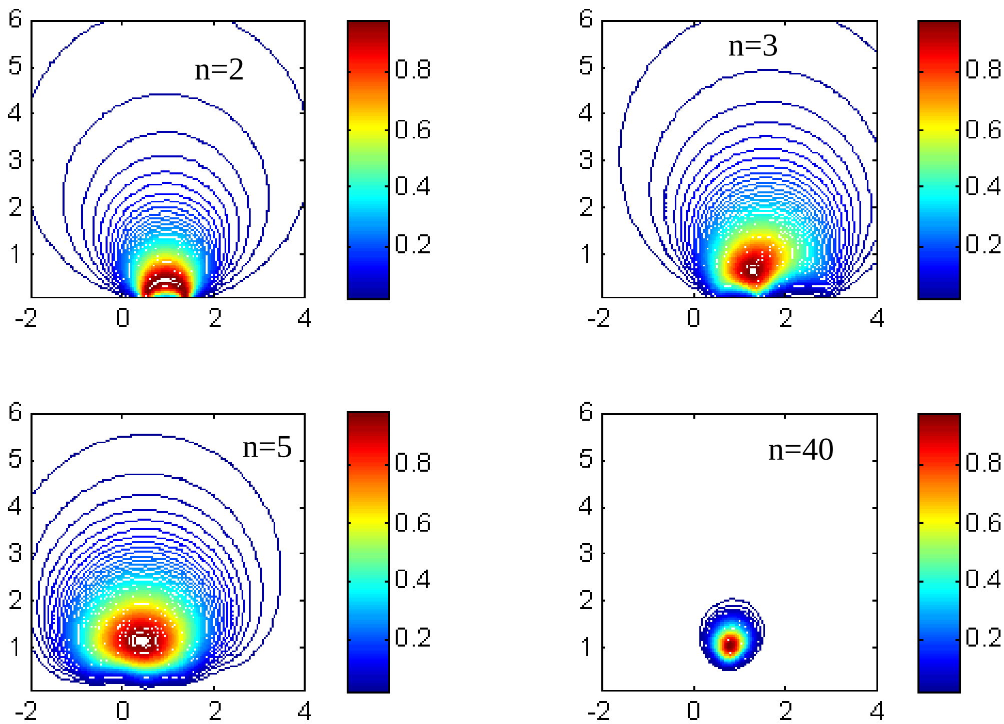

Figure 2-7. The joint posterior density function in both the x and y positions.

To include as part of the problem the determination of the y position, assuming the prior $p(y)$ is a constant the full 2D posterior probability is written as,

$$p(x, y \mid \{x_i\}) \propto p(x \mid \{x_i\}, y)\, p(y) \propto p(x \mid \{x_i\}, y). \tag{2-27}$$

Instead of being a constant that is specified, y becomes a variable. The 2D plots shown in Figure 2-7 demonstrate how the lack of knowledge of y complicates the problem. The prior is assumed to be a constant in the above example to reflect our complete ignorance of the source position. Thus the posterior probability is the same as the likelihood. The likelihood only states the relative probability of obtaining the specific set of measurements, given a particular x. Note that Bayes's law is necessary to gain information about x from the likelihood. If it was known that the source position was limited to a specific region, an appropriate prior would consist of a function that is a nonzero constant inside the region and zero outside. This prior would have the effect of eliminating the tails of the posterior probability outside the legitimate region. The updating result shows that the updating with 40 samples can achieve an accurate result indicating that the source point is approaching the true source location at (1, 1).

2.2.2 Image Segmentation with Markov Random Field Prior

In image segmentation for damage estimation, the prior function $p(x)$ refers to the prior assumptions about the SHM images. One of the most important assumptions is how the pixels spatially constrain or correlated with each other. Images from the other SHM system, the geometry of the structure and the measurements from the environments can also be used as the prior information. The likelihood function relates to the observed information, which is the detected intensity image in diagnosis from the guided Lamb wave imaging with limited sensor array patterns, such as linear sensor array or distributed sensor array. Figure 2-8 shows the Bayesian updating framework for image segmentation.

MRF is employed to model the presumption for image segmentation as a pixel-to-pixel correlated image field. MRF image modeling has been used successfully in many image processing applications as discussed above. The success of MRF modeling mainly arises from its systematic and flexible treatment of the contextual information in the image. Prior knowledge for the image segmentation can be easily quantified by MRF model parameters. Image segmentation processes the property of contextual smoothness of the class labels in the image space so that a pixel with a particular class label is likely to share the label with its immediate neighbors. Moreover a Bayesian framework using MRF provides feasible optimal solutions. The optimization process using spatial local interaction makes parallel and local computations possible. The followings are some basic definitions and derivations for the image segmentation based on Bayesian updating framework with MRF prior.

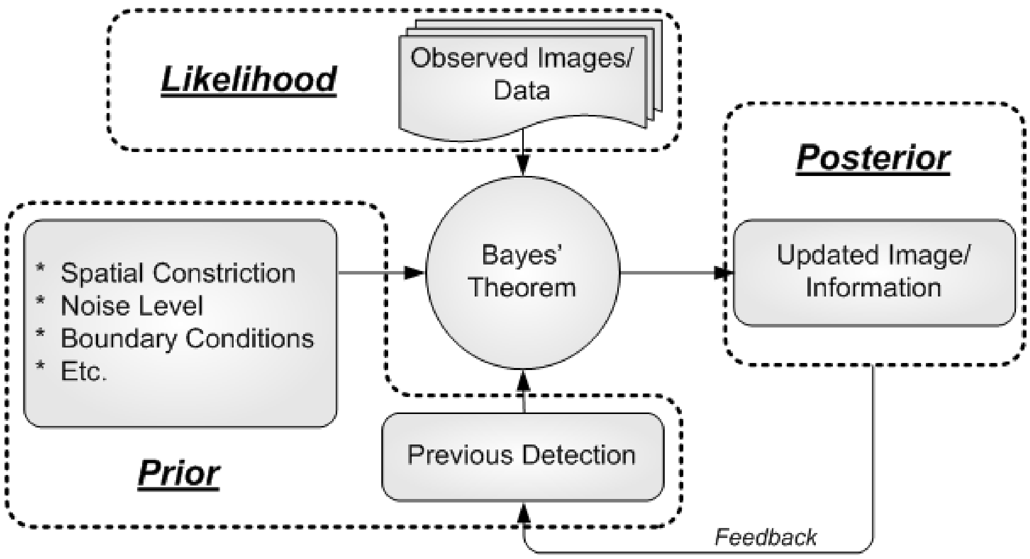

Figure 2-8. Framework of Bayesian based image segmentation.

Neighborhood

In digital image processing, a neighborhood system η associated with the whole image Ω is a collection of its neighborhoods $\eta = \{\eta \mid s \in \Omega\}$, where each η_s is a neighborhood of the pixel at the site of *s* satisfying:

(1) The pixel itself does not belong to its own neighborhood, which means $s \notin \eta_s$, and $\eta = \{\eta \mid s \in \Omega\}$;

(2) The pixel s belonging to the neighborhood of the pixel t implies that the pixel t belongs to the neighborhood of the pixel s, which means if $s \in \eta_t$, $t \in \eta_s$.

Cliques

Considering an image defined on a Cartesian grid, a clique is a subset C of the whole image Ω if two different elements of C are neighbors. Figure 2-9 gives the 2nd order neighborhood, all the available cliques in an 8-element neighboring system, and several non-clique group. The definition of clique system makes the neighboring pixels correlated with certain discipline.

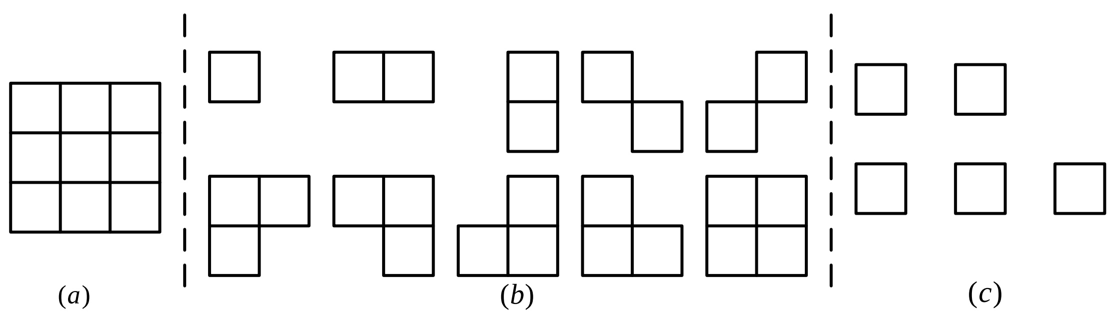

Figure 2-9. (a)2nd order neighborhood and (b) its cliques and (c) non-clique pixels

Markov Random Field

A MRF on (Ω, η) is a random field with its probability property of each pixel in the whole field satisfying the Markovian property described as following,

$$P(X_s = x_s \mid X_t = x_t, \forall t \in \Omega, t \neq s) = P(X_s = x_s \mid X_t = x_t, t \in \eta_s), \forall \in \Omega. \qquad (2\text{-}28)$$

Gibbs Random Field

A random field X with (Ω, η, C), is a GRF if its distribution has the following form,

$$p(x) = \frac{1}{Z}\exp\left(\sum_{c \in C} V_c(x)\right), \qquad (2\text{-}29)$$

where C is the set of all cliques in Ω, Z is the normalizing constant, and Vc(x) is the clique potential associated with clique c. There is no particular restriction on the clique potential definition. As long as the resulting Gibbs distribution satisfies the definition of the probability, the associated clique potentials are valid. The Gibbs potential can be defined such that some specific features of the image can be identified and emphasized. In addition, it is not necessary to use all types of cliques for a given neighborhood system; that is, any specific set of clique types can be selectively used for specific problems.

Prior knowledge in the image segmentation, such as the spatial constraint on the class label, can be incorporated into the Gibbs distribution by the choice of specific clique types and their potentials. For example, the smoothness of the class label in image space can be measured by defining the clique potential such that a high positive clique potential is assigned only when all class label in the clique are identical.

Hammersley-Clifford Theorem

A MRF is characterized by its local property (the Markovianity) whereas a GRF is characterized by its global property (the Gibbs distribution). Hammersley-Clifford Theorem [83] builds a bridge between MRF and GRF. It indicated that a random field X, on (Ω, η, C), is a MRF with respect to η if and only if $p(x)$ has a Gibbs distribution with respect to η. Thus, it is possible to express the conditional probability of a MRF in terms of clique potentials. This is useful in practice because it is easy to choose the clique types and their potentials to describe the desired local behavior. For example, local spatial relationships such as smoothness and continuity of the neighboring pixels can be specified by isotropic pair clique potential $V_C(x)$. It is crucial for the theorem to share the same neighborhood system η and the associate clique c for both MRF and GRF.

The SHM image is constructed by the pixels in the square lattices, which is considered as a MRF as described above for its close-neighboring correlation. Those damage areas are with high grey level pixels in its lattice. Through the GRF, which reflects the property of MRF and has concrete representation – Gibbs potential, this information will be transmitted to the probability of damage, which will affect the determination of whether the pixel belongs to the damaged class or undamaged class.

The image from the structural health monitoring system by the signals of the sensor array for damage detection is usually noisy and with fuzzy tails. The image can be considered as the overlap of some small lattice blocks, in which correlative potential is preset with the form of MRF, which has the potential to eliminate the effect of noise and fuzzy tails in the crack contained images by designating those similar neighbors with higher probability and those different neighbors with lower probability. Thus the segmentation procedure depends on not only the detected image of intensity but also the spatial restriction property of the neighboring system described as MRF.

The maximum a posteriori (MAP) criterion [85] is generally used to make decision for problems which need to include the prior knowledge and current observation. According to the MAP criterion, given a realization of a random field, the goal is to find an optimal realization of $\hat{x}$, which maximizes the posteriori probability $p(x \mid y)$ for all possible realizations of *x*. The maximization procedure can be equivalently expressed as:

$$\hat{x} = \arg\max_{x} \{ p(x \mid y) \}. \tag{2-30}$$

where argmax is an operation to achieve estimation of the given argument for which the value of the given expression attains its maximum value.

The image segmentation problem can be achieved by estimating $\hat{x}$ though maximizing the posterior conditional probability function, $p(x \mid y)$, which indicates the probability of a pixel belonging to a specific segmentation class x given the current observation y. Substitute Eq. (2-19) into Eq.(2-30), the estimation of *x* can be rewrite as,

$$\hat{x} = \arg\max_{x} \left\{ \frac{p(y \mid x) p(x)}{p(y)} \right\}. \tag{2-31}$$

Since the marginal probability $p(y)$ is a normalization item, which will not affect the comparison of probability of the observed pixel belonging to a given class. Therefore, for the purpose of pixel classification, Eq. (2-31) can be simplified.

$$\hat{x} = \arg\max_{x} \{ p(y \mid x) p(x) \}. \tag{2-32}$$

In Eq.(2-32), the estimation of the classification of each pixel is determined by two factors, $p(x)$ and $p(y \mid x)$. $p(x)$ is the prior information, which in the image segmentation problem is the assumed segmentation class label. $p(y \mid x)$ is the observed information, which indicates the probability of a pixel equal to the observed value given the pixel belonging to a specific class. Equivalently, the estimation of x can be achieved by maximizing the natural logarithm of the posterior,

$$\hat{x} = \arg\max_{x} \{ \ln p(y \mid x) + \ln p(x) \}. \tag{2-33}$$

The observed image from a structural health monitoring system acting as the likelihood can be modeled with the Gaussian distribution[80], and the prior assumption is the GRF. Thus the MAP problem can be described as:

$$p(y \mid x) = \frac{1}{\sqrt{2\pi\sigma^2}} e^{\left(-\frac{1}{2\sigma^2}\left(y_s - \mu_s^{x_s}\right)^2\right)}, \tag{2-34}$$

where μ_s and σ^2 are the mean and variation of the Gaussian distribution of the class x_s. Substitute Eq.(2-29) and Eq.(2-34) into Eq.(2-33), the segmentation problem can finally be described as:

$$p(x\mid y)=e^{\left(-\frac{1}{2\sigma^2}\left[y_s-\mu_s^{x_s}\right]^2-\sum_C V_C(x)\right)}\text{-}\ln\sqrt{2\pi\sigma^2}-\ln(Z), \tag{2-35}$$

where x is the segmentation label ranging from 1 to k, s is the position of the estimated grid, y_s is the observed value (gray-value of segmented images), and μ is the mean value in the window with a certain size centered at the observed pixel. Ignore the constant in the equation, and the image segmentation problem can be finally formulated as,

$$\begin{aligned}\hat{x} &= \arg\max_x \left\{ p(x\mid y)\right\},\\ &= \operatorname{argmax}_x \left\{ e^{\left(-\frac{1}{2\sigma^2}\left[y_s-\mu_s^{x_s}\right]^2-\sum_C V_C(x)\right)} \right\},\\ &= \arg\max_x \left(-\frac{1}{2\sigma^2}\left[y_s-\mu_s^{x_s}\right]^2-\sum_C V_C(x)\right).\end{aligned} \tag{2-36}$$

For a binary segmentation for SHM, in which there are only two labels for the damaged class and the undamaged class, 0 and 1, if $p(x = 0 \mid y) > p(x = 1 \mid y)$, the estimated class label x should be 0; and if $p(x = 0 \mid y) < p(x = 1 \mid y)$, the estimated class label x should be 1; thus the estimation of the segmentation $\hat{x}$ for the whole image domain is achieved.

The posterior probability comprises of two parts. The first part is Gaussian distribution likelihood, and the second part is the prior density function -- Gibbs potential. The first part is essentially a k-means method, which calculates the distance between the evaluated pixel value and the clustering center. If the evaluated pixel value is close to one cluster center, the posterior energy function will be enhanced. The second part is the adjustable part according to the Gibbs potential guided neighboring system. If the neighbor clique member is with the same label (from initialization or the previous segmentation), the Gibbs potential $V_c(x)$ should be negative, then the posterior energy density will be enhanced. On the other hand, if the clique members are at different labels, the posterior energy density will be weakened. For a specific case, neglecting the prior distribution by setting the potentials in Gibbs random field zeros, this algorithm degenerates to a *k*-means clustering method, which only counts the distance between each point with the clustering centers.

For computational efficiency, the 2nd order clique is generally adopted, which contains an eight-element neighborhood as in Figure 2-9. According to the MRF-GRF equivalence described by Hammersley-Clifford theorem, the clique potential is given in the form of Gibbs density as Eq.(2-37), and the Gibbs potential value is defined as [80],

$$V_C(x) = \begin{cases} -\beta \ \text{ if } \ x_s = x_q \ \text{ and } \ s, q \in C, \\ +\beta \ \text{ if } \ x_s \neq x_q \ \text{ and } \ s, q \in C, \end{cases} \tag{2-37}$$

where β is positive, and the choice of β will affect the spatial constraint in the GRF. Larger β results in stronger spatial constraint; that is, neighbors are more likely to have the same label. This tendency will lead to the conservation of the real damage area and the cancellation of the random noise area in the segmentation procedure for SHM images.

2.2.3 Application

SHM imaging for damage detection and estimation for plate-like structures have drawn continual interest. The time-reversed algorithm developed in time-space domain and frequency-wavenumber domain has been successfully verified for its effectiveness in this purpose. The migration imaging technique, based on Mindlin plate theory, is one of the most promising methods for the multi-damage identification in plate-like structures using scattered Lamb waves in combination with the time-coincidence imaging condition.

The migration technique can effectively interpret the sensor data recorded by a distributed linear array sensor system and makes it possible to establish an active, in-service, and intelligent monitoring system. The image for segmentation is obtained from an active diagnostic linear array of actuators/sensors, which is used to excite/receive the flexural waves. The wave field scattered from the damage and sensor array data are synthesized using a two-dimensional explicit finite difference algorithm to model wave propagation in the plate. The detailed description about migration algorithm for SHM imaging can be found in[45].

Figure 2-10 (a) is a noisy migration imaging result with a surface-mounted seven-sensor array for aluminum plate structure using a 150kHz central frequency excitation.

When *k*-means segmentation is applied to the migration images, the segmentation result is shown in Figure 2-11(b), which is the result ignoring the neighboring system interaction. The noise cannot be eliminated and some of the medium grey-levels in the fuzzy tails will be segmented as the damaged area. MRF features the property of emphasizing the local constraint by introducing the Gibbs potential in the posterior probability. Thus the damaged area from the segmentation shrinks regardless of the ghost images.

Figure 2-10(b) gives the segmentation result and its region resulting from Bayesian updating framework. The damage size is defined as the maximum measurement of the pixel-pixel distance in the damaged zone. As a comparison, for a 20 mm crack, the crack length obtained from the *k*-means segmentation is 30 mm, while the estimated crack size obtained from the Bayesian updating algorithm is 25 mm due to the inhabitation of fuzzy tails at the two tips of the crack, providing more precise crack size estimation. Furthermore, the crack size estimated is larger than the true crack size, ensuring the conservative measure of the damage.

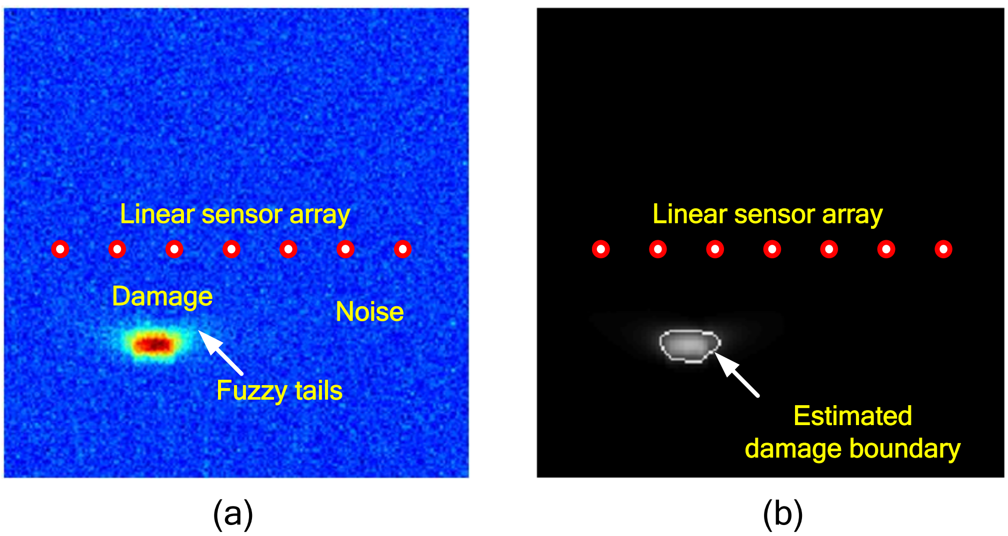

Figure 2-10. (a) An migration image (b) its Bayesian segmentation.

Effects of Markov random field

The MRF affects the segmentation procedure by inducing Gibbs potential as the prior in the Bayesian updating framework. The parameter β in the Gibbs potential plays an important role in the segmentation procedure. It determines how the neighboring system affects the label of the estimated site. For example with the original image as showed in Figure 2-11(a), when $\beta = 0$, the Bayesian segmentation reduces to the k-means clustering, which segments some of the noise area in the same region of the damaged area and the result is given in Figure 2-11(b). It is hard to determine the crack length with such segmentation. With the increscent in β, the noise is suppressed, and the damage area shrinks to the real damaged area as shown in the Figure 2-11(c) and (d). Results show that the segmentation does not change when β varies from 0.9 to 100, which shows the stability of the segmentation procedure. The reason of the convergence phenomenon is that the Gibbs potential plays only an adjustment role in the Bayesian updating procedure, but not a dominating role.

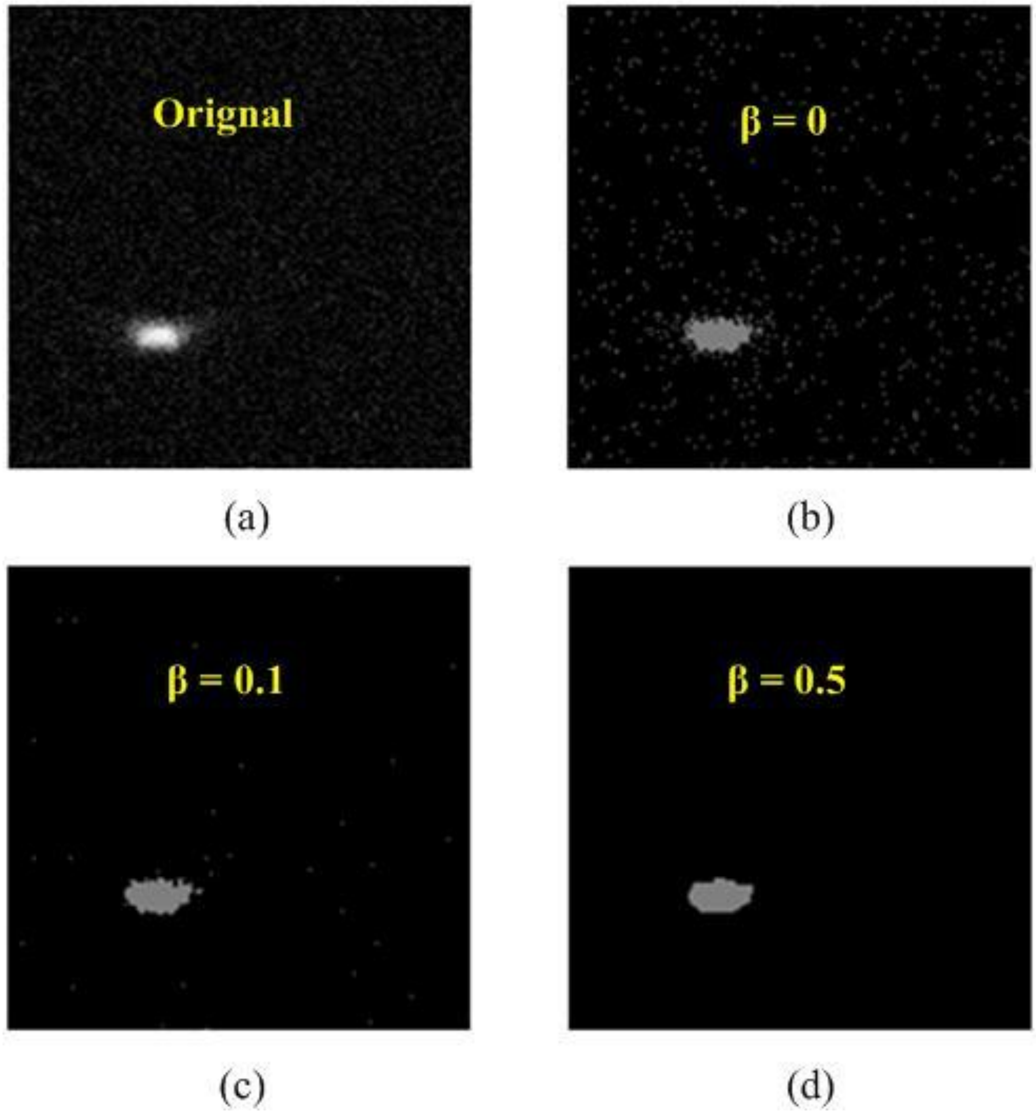

Figure 2-11. Bayesian image segmentation with different Gibbs potentials.

Multi-location simulations are carried out to examine the accuracy and robustness of the image segmentation method. As shown in Figure 2-12, A1~A7 are seven actuators, which equally distributed horizontally as in the previous study. d1~d12 are twelve cracks simulated on the plate, and the interval of them are 60mm horizontally and 30mm vertically. Estimations in Table 2-2 show that the crack size is obtained close to the true crack size, and the estimated crack location, obtained by calculating the global peak of the whole image field is close to the true crack location, since the mesh size of the simulation is 2.5mm per grid as far.

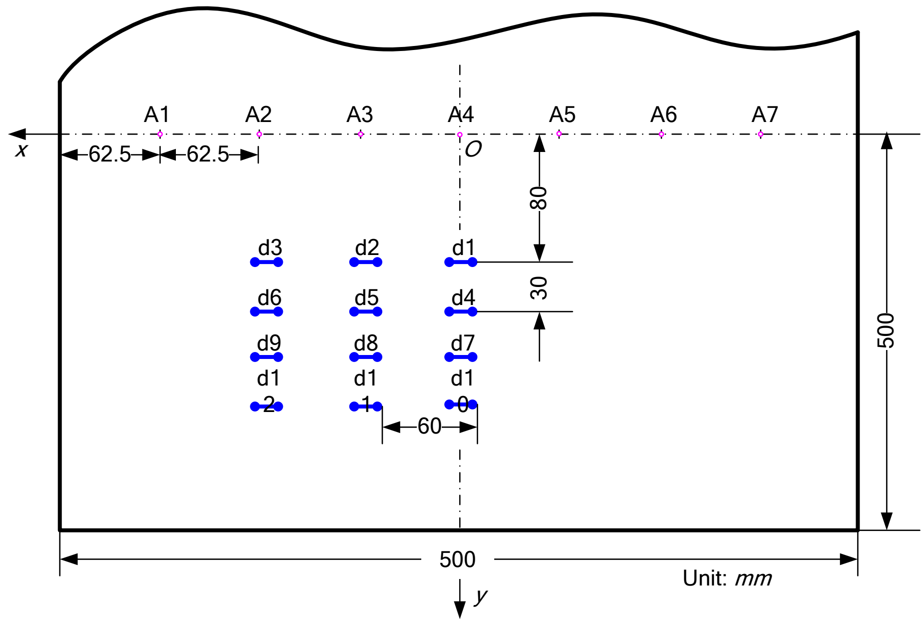

Figure 2-12. Outline of multi-location crack size simulation.

Table 2-2. Center location and damage size for multi-location simulations (Unit: *mm*).

Crack location No.	True values		Estimated value	
	Size	Location	Size	Location
d1	20	(0,80)	27.5	(0,80)
d2	20	(60,80)	25	(60,80)
d3	20	(120,80)	22.5	(117.5,80)
d4	20	(0,110)	27.5	(0,110)
d5	20	(60,110)	27.5	(57.5,110)
d6	20	(120,110)	22.5	(117.5,107.5)
d7	20	(0,140)	27.5	(0,140)
d8	20	(60,140)	25	(57.5,137.5)
d9	20	(120,140)	22.5	(117.5,137.5)
d10	20	(0,170)	27.5	(0,170)
d11	20	(60,170)	22.5	(57.5,167.5)
d12	20	(120,170)	22.5	(117.5,167.5)

2.2.4 Discussion

The damage segmentation with Markov random field achieves accurate and robust estimation from the SHM image results. Improved segmentation result can be achieved by updating the segmentation with the previous posterior distribution as the prior with the new observation behaving as the current likelihood function. Different detection techniques can be implemented for the same diagnosis task. Bayesian updating frame updates the segmentation continually, providing more and more reliable and accurate damage estimation. Carry out detection with multiple frequency excitations is one of the methods, which contains more collected information with versatile techniques of measurement.

For the same geometry model investigated in the section 2.2.3, the central frequency of the excitation is 150 kHz. However, the cracks in the structures are generally frequency-sensitive. High frequency excitation generates high resolution images with sharp edges, but low signal noise ratio (SNR). On the other hand, low frequency excitation generates low resolution but clear images with fuzzy edges. The segmentation contains more information when a frequency range is applied for excitation. It is more reliable for diagnosing a complex structure by choosing a frequency range as the excitation, because it easier to choose the frequency band for a structure for its complex geometries and homogeneous distribution of materials. In a numerical simulation, for a preset 20mm crack, the best result for individual excitation frequency is 25mm, which is of 150 kHz. For clear image from a lower frequency, the resolution error is large. And for the fuzzy image from a higher frequency, it is hard to determine the crack size for its irregular distribution of image. When Bayesian updating framework is used to update these images (with excitation frequency, 50kHz, 100kHz, 150kHz, 200kHz, 250kHz, and 300kHz), the estimated crack size from the final segmentation is 23mm, which is much closer to the true crack size than the 150kHz result and still conservative in reflecting the true crack size.

The investigated image segmentation method based on Bayesian updating for damage size estimation has shown to possess the following advantages:

(1) Spatial constraint introducing the constraint in the neighboring system performs better than *k*-means clustering, which only considers the grey-level distance between the pixels and the clustering centers. As a result, the damage region is focused on suppressing the fuzzy tails that may appear on both crack tips.

(2) Bayesian based segmentation holds the promise of reducing noise by applying the GRF, which assumes that neighboring pixels more likely belong to be the same class.

(3) The segmentation result gives damage shape and region estimation of the damaged area.

In summary, the Bayesian updating with the MRF as a prior can efficiently segment an image into multiple regions, which distinguishes damaged regions from undamaged regions.

3 Probabilistic Damage Sizing

The structural health monitoring system is designed to monitor the structures continually and rapidly during the service although the resolution is generally lower than traditional offline nondestructive testing (NDT) inspections. Incorporating the cumulating information collected from sensor array, damage propagation models can be used to accurately assess the structure's condition, predict the damage propagation with the pre-assumed loading condition, and calculate the remaining useful life (RUL). Damage imaging provides intuitive method for quantifying the damage for SHM[31, 86]. The method proposed in this section focuses on extracting the probabilistic damage sizes from the intensity of the damage image for plate-like structural detection, thus fills the gap between the damage image and prognosis. A premise behind the method is that a two-dimensional image intensity displayed by the brightness of the pixels provides a probabilistic distribution of damage severity in the structures to be monitored. Although there are ever-increasing demand to achieve higher accuracy of damage imaging using advanced diagnostic techniques and latest instruments on the ground under laboratory controlled environments, it is always desirable to size the damage with an on-line SHM system. With the constraints of space, weight, instrumental and environmental complexity involved, the accuracy and precision of the SHM system is not as good as desired. However accumulated damage images by the SHM system have the potential to provide more reliable knowledge of the monitored structures.

The fatigue life spent constitutes crack initiation, followed by crack growth, and leading to the structure failure. The crack growth, representing a major portion of the fatigue life of many structures, is the focus in this study. Models have been developed for damage propagation, such as Paris law, Forman equation, and Walker equation[62]. Since the main objective of this work is to develop a damage sizing technique for damage prognosis, a simple Paris law, is employed to govern the crack growth and predict the RUL of the structure panel, however, more complicated damage growth models can be readily substituted for implementation if required.

Probabilistic concepts have been introduced in fatigue analysis, recently in damage prognosis. Lin and Yang[10] obtained an analytical expression for probability distribution of crack size at any given time and the probability distribution of the time at which a given crack size is reached based on the knowledge of the initial crack size. The time dependent crack size is approximated by a Markov process. [7, 68]'s group developed a probabilistic procedure to predict the macro-crack initiation and calculate a probability of detection (POD). Coppe *et al*.[11] applied a Bayesian based method to narrow the distribution of the material parameters in the Paris law. A kernel-based Gaussian random process was used for the time series prediction of fatigue crack growth function under variable loading by Mohanty *et al*.[69]. However, these studies started with a pre-assumed probabilistic model of damage size or based on a large amount of data from time and expensive experiments. However, in damage prognosis with structural health monitoring, various imaging techniques have different degrees of precision and accuracy in terms of damage severity. Even with the same hardware, different excitation configurations, such as waveforms and frequencies, may lead to varied image resolutions. The resulting on-line SHM imaging can be more complicated due to the noisy environments, leading to the change of the probability of detection (POD)[69]. Therefore, a probabilistic representation of the crack sizing for damage propagation law is indispensible in enhancing the confidence of damage prognosis and providing more comprehensive information.

In this chapter, a 3-step procedure is developed to quantify damage from SHM images, and morphological gradients of the image data is employed to enhance the damage sizing to obtain narrower distribution for damage prognosis. This chapter is organized as follows. Section 3.1 is to define the problem of PDF extraction from damage image and its motivation. Section 3.2 develops a basic 3-step procedure for extracting PDF from an intensity image. In Section 3.3, illustrative examples are given, and comparisons are carried out to validate the procedure. A correlation based detection and migration imaging technique are employed to generate damage detections. The damage sizes used to generate images are simulated by Paris law for each 1000 fatigue cycles. Section 3.4 will improve the 3-step procedure by introducing a morphological gradient, an inherent feature of images, as a prior in Bayesian updating framework, reducing the uncertainty of crack size estimation, and an extension to 2D probabilistic estimation of damage area is also been discussed.

3.1 Motivation for Probabilistic Damage Sizing

The image intensity generated by structural health monitoring imaging algorithms in a plate is a 2D intensity map, whose values are used to represent the probability of the damage severity and location of the plate. However the image intensity obtained from the SHM system may be ambiguous due to the limited number of sensors and is often contaminated by noise. Consequently, unwanted images such as ghost shadow and fuzzy tails reveal. A statistical image segmentation method developed in Section 2.2 utilizes the prior Markov random field to evaluate the boundary of damage from SHM images by reducing random noises and suppressing fuzzy tails. However, the method utilizes the maximum a posterior (MAP) to yield a deterministic damage size, which loses important information – the confidence on damage size and location. For example, Figure 3-1(a)-(c) shows hypothetical image intensities of a damage detected by three different techniques. The sharp image (a) is obtained by a high resolution detecting technique; while the diffused one (c) by a low resolution detecting technique. If a threshold method is applied, the three images may yield different damage sizes, depending on the threshold used, which is obviously inappropriate. For the image segmentation technique developed in the last chapter, the damage sizing result is exactly the same, which is true, but no more information about the confidence of the estimated size. For illustration purpose, the PDFs of the damage size that will be exploited later are also plotted below the Figure 3-1 (a)-(c), in which the sharp image yields narrower distribution than the diffused one. These

PDFs can provide confidence levels of the estimated damage size and can be used to rank different damage detection methods.

For the purpose of remaining useful life calculation for cracked plates, the crack length is essential, so the following work are going to focus on how to extract the probability density function (PDF) of crack size from intensity curve cut in a detected image. It is possible to find the crack orientation by image processing methods, e.g. ridge detection and Eigen-value method. In our study, an intensity curve is cut from the 2D imaging map along the damage orientation, e.g. the dotted curves cut from the middle of the damage shown in Figure 3-1(a)-(c). The damage orientation can be found using eigenvalue analysis using image intensity. The objective of the proposed 3-step procedure is to obtain the PDFs of crack sizes from cut intensity curves. Assuming the intensity curve cut from an SHM image represents a single damage, the PDF of the damage size should satisfy the following general PDF properties as well as application-specific properties:

(1) The probability of damage size is no less than 0, which means

$$P(a_i) \geq 0, \tag{3-1}$$

for all possible damage size ranging from 0 to $a_{\max}$, here $a_{\max}$ is the maximum length of the intensity curve.

(2) The integration of all possible damage size is unity, which means,

$$\int_0^{a_{\max}} f(a)\ \mathrm{d}a = 1, \tag{3-2}$$

here, $f(a)$ is the PDF of the damage size.

(3) With the specific assumption that the probability of the damage size less than 0 or larger than the maximum image size is 0,

$$\begin{aligned} &P(a \le 0) = 0, \\ &P(a \ge a_{\max}) = 0. \end{aligned} \tag{3-3}$$

(4) Sharper detection with clear damage boundary (generally from high resolution techniques) should have more focused PDF (smaller standard deviation or dispersion), while diffused detection with fuzzy boundary (generally from low resolution techniques) should have less focused PDF (larger standard deviation or dispersion).

Features (1) and (2) are inherent properties of general PDFs, and features (3) and (4) are specific ones for extracting PDFs from SHM images. These features will be used to check the validity of the extracted PDF of damage size in the following Sections.

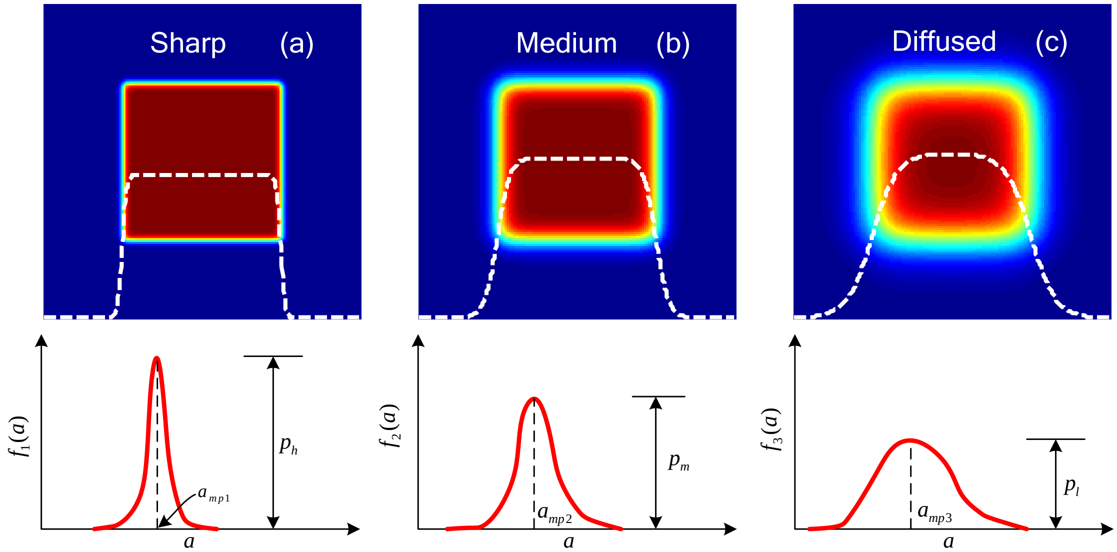

Figure 3-1. Images with various resolutions and expected PDFs of damage size.

A 3-step PDF extraction procedure is designed as shown in Figure 3-2 to quantify cracks in the image with probabilistic concept: (1) evenly spaced sampling, (2) empirical cumulative density function (ECDF) calculation, and (3) CDF to PDF conversion.

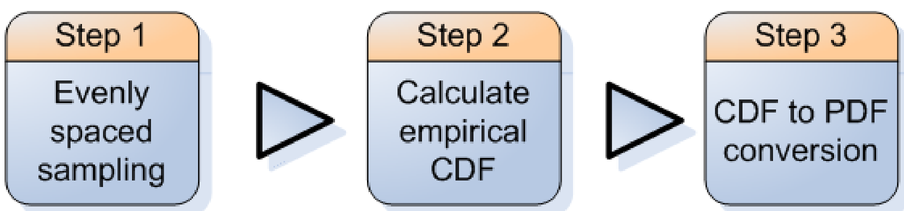

Figure 3-2. 3-step procedure proposed to extract PDF of damage size.

3.2 3-step Procedure for Determining PDFs of Crack Size

3.2.1 Evenly Spaced Sampling

This study focuses on a straight through-the-thickness crack with half crack sizes ranging from 10 to 50mm. In such a case, the 1D intensity curve can be extracted by making a cut along the crack orientation from the intensity image. The center location of the damage may be defined as the peak pixel level in the 2D image. The orientation of crack is estimated by ridge detection. Other studies about determining crack orientation can be found in Lu *et al.*[87]. Cutting along the crack orientation, a normalized intensity curve, $G(x)$, can be formed from the SHM images. For a pixel-based image intensity, $G(x)$ can be formulated as a piecewise linear polynomial or a piecewise step function. It is assumed that the cracked region is confined within the imaging domain such that the image intensity is zero at both ends. In the evenly spaced sampling scheme, the vertical range of $G(x)$ is evenly divided by n intervals, and the value of $G(x)$ corresponding to the k-th location is normalized and denoted by $\Psi(k)$

$$\Psi(k) = \frac{n-k}{n}, \quad k = 0,1,\cdots,n. \tag{3-4}$$

which decreases linearly from 1 to 0, acting as a cross-threshold. This measure can be considered as spaced sampling in horizontal direction to extract the damage size. In the case of continuous $G(x)$, the accuracy of estimated damage size is proportional to the number of intervals.

The fundamental idea of the proposed approach is that the difference between these two cross points provides the estimated damage size when the given level of image intensity is used for a cross-threshold. Thus at the intensity level $\Psi(k)$, the damage size is estimated by

$$\begin{aligned} a(k) &= \Delta x\left[\Psi(k)\right] \\ &= x_{\max}\left[\Psi(k)\right] - x_{\min}\left[\Psi(k)\right]. \end{aligned} \tag{3-5}$$

Figure 3-3(a) illustrates the evenly spaced sampling procedure. The normalized intensity curve cut from an intensity image is evenly sampled between 0 and 1 to estimate damage size $a(k)$, and the samples of damage sizes are listed in the increasing order shown in Figure 3-3(b) for further analysis.

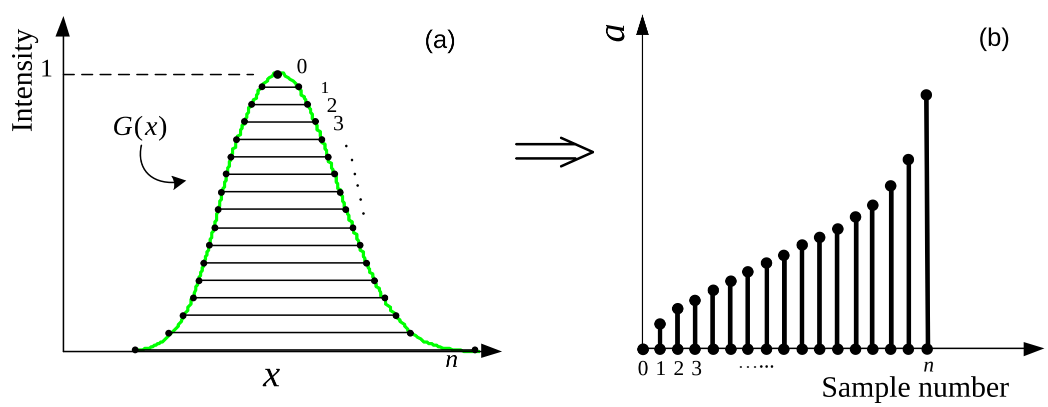

Figure 3-3. An illustrative intensity curve and its damage size samples.

3.2.2 Empirical CDF Determination

An empirical cumulative density function (ECDF) is then used to describe the distribution of measured samples in Eq. (3-5), providing probabilistic information about the crack size. The CDF is defined as in Eq. (3-6), which is the integration of the PDF, a monotonically increasing function with the maximum value being unity. The cumulative probability of crack size a_i is the summation of all the probability of the crack length less than a_i, formulated as in Eq. (3-6):

$$F(a_i) = P(a \le a_i), \tag{3-6}$$

$$F(a_i) = \frac{M\{a \mid a \le a_i\}}{M\{a \in \Omega\}}. \tag{3-7}$$

For a discrete sample set, the CDF of crack size a_i is given in Eq. (3-7). $M\{a \mid a \le a_i\}$ is the number of samples with size less than a_i, and $M\{a \in \Omega\}$ is the total number of samples. Figure 3-4(a) gives the samples from evenly spaced sampling, and the CDF by smoothing the empirical CDF is given in Figure 3-4 (b).

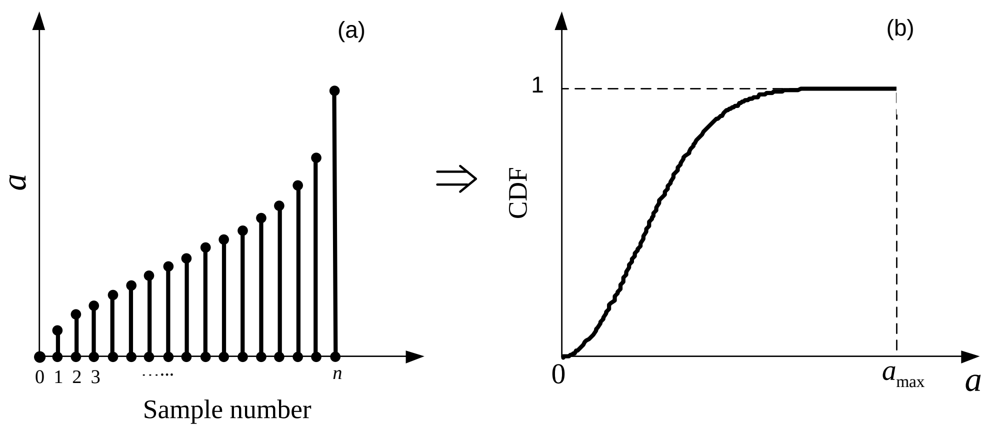

Figure 3-4. Illustrative samples of damage size and its CDF.

3.2.3 CDF to PDF Conversion

The PDF can be obtained by differentiating the CDF using Eq.(3-8),

$$f(a) = \frac{d[F(a)]}{da}. \tag{3-8}$$

Since the CDF is given as discrete values, the PDF also needs to be normalized and smoothed. Figure 3-5(a) is an illustrative CDF obtained from the previous step in Figure 3-4(b), and the converted PDF is shown in Figure 3-5(b). The area under the PDF curve should be one.

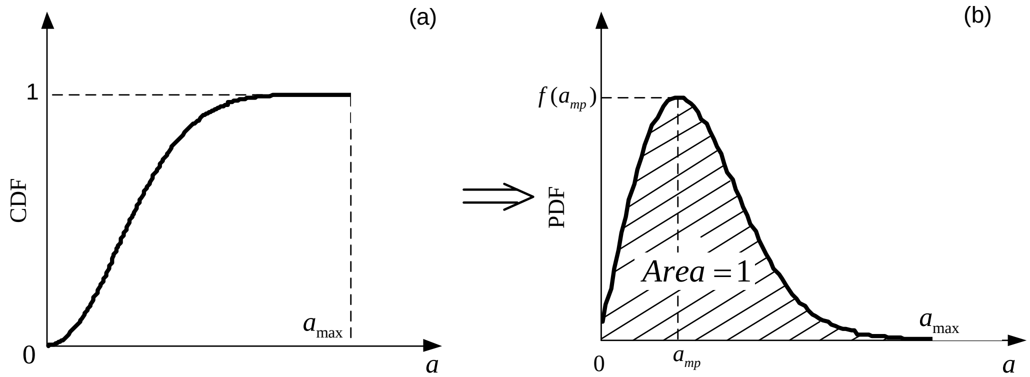

Figure 3-5. Illustrative CDF and converted PDF.

The above unified 3-step procedure is potential to convert an intensity curve from image intensity into the PDF of the damage size. The evenly spaced sampling step not only provides its simplicity but also reveals the sharp damage boundary, resulting in more concentrated PDF. In addition, the probability of damage size larger than the pre-defined critical damage size can be calculated by integration. These features will be verified in the following sections.

To start with a simple case study, a correlation-based damage image example is given as follows to illustrate the PDF extraction procedure because many damage imaging algorithms are more or less based on the cross-correlation [31] of sensed signals.

A cross-correlation is used to model the damage detection procedure, which can be described as a linear system and formulated as in Eq. (3-9),

$$R(n) = S(n) \otimes D(n), \tag{3-9}$$

where $S(n)$ is the structural mapping with damage assignment and n is the sampling index along the position. $D(n)$ is the transfer function of the detector. $R(n)$ is the response. And, $\otimes$ is a correlation operator. In view of linear systems, they are inputs, transfer functions of the system and outputs, respectively. Figure 3-6 (a) is assumed to be a rectangular function of the damage assignment, in which 0 designates health regions and 1 designates the damaged regions. Therefore the damaged region is from 600*mm* to 1400*mm*, giving the damage size being 800*mm*. Various detectors with high ($\sigma = 50$), medium ($\sigma = 120$) and low ($\sigma = 200$) resolutions, as in Figure 3-6(b), are used to detect the damage. These three detectors are formulated by transfer functions in Gaussian type, which are commonly used in signal modulation for SHM. The detector with narrower Gaussian envelope has higher resolution, and vice versa. Figure 3-6(c) shows the normalized correlation-based measures (intensity curves) with the three types of Gaussian detectors with low, medium and high resolutions with standard deviation 200, 120 and 50, respectively. Narrower detector leads to steep responsive boundary and higher resolution detection. With the 3-step procedure, Figure 3-6(d) shows the extracted PDF reflecting the size of damage from the original assignment. The narrower the detector is, the more concentrated the PDF of damage size will be. Thus, the dispersion of the PDF reflects the resolution of the damage detection technique.

Figure 3-6. An example of correlation-based damage detection.

(a) Damage assignment; (b) Gaussian detector with different resolutions;

(c) Correlated responses; (d) Extracted PDFs

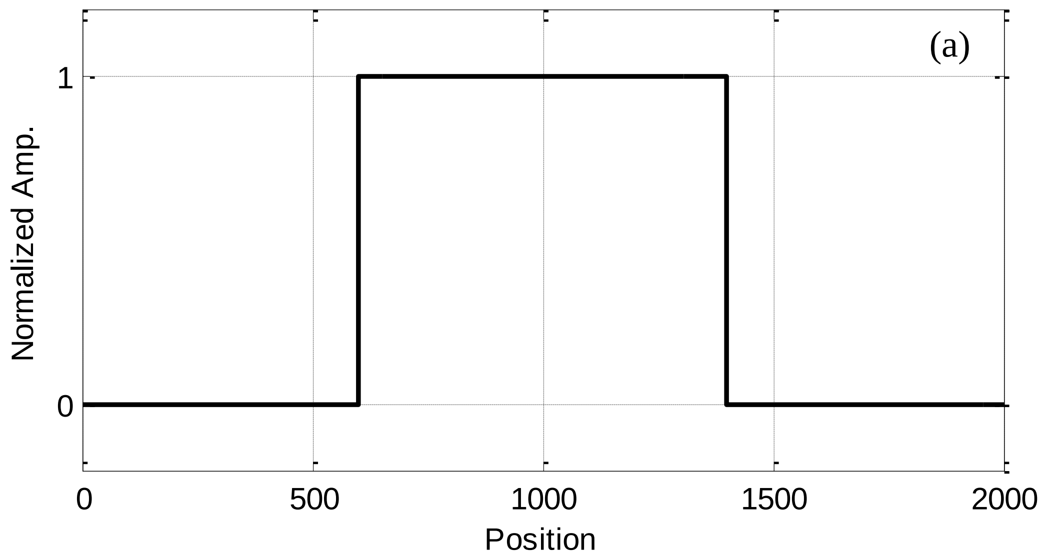
(a)
1
0
Normalized Amp.
0
500
1000
1500
2000
Position

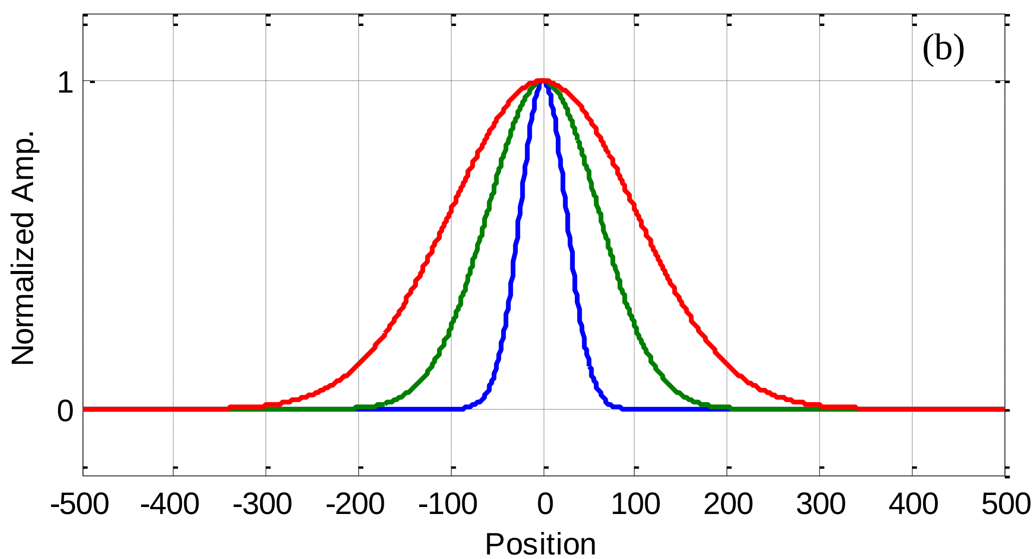
(b)
1
0
Normalized Amp.
-500
-400
-300
-200
-100
0
100
200
300
400
500
Position

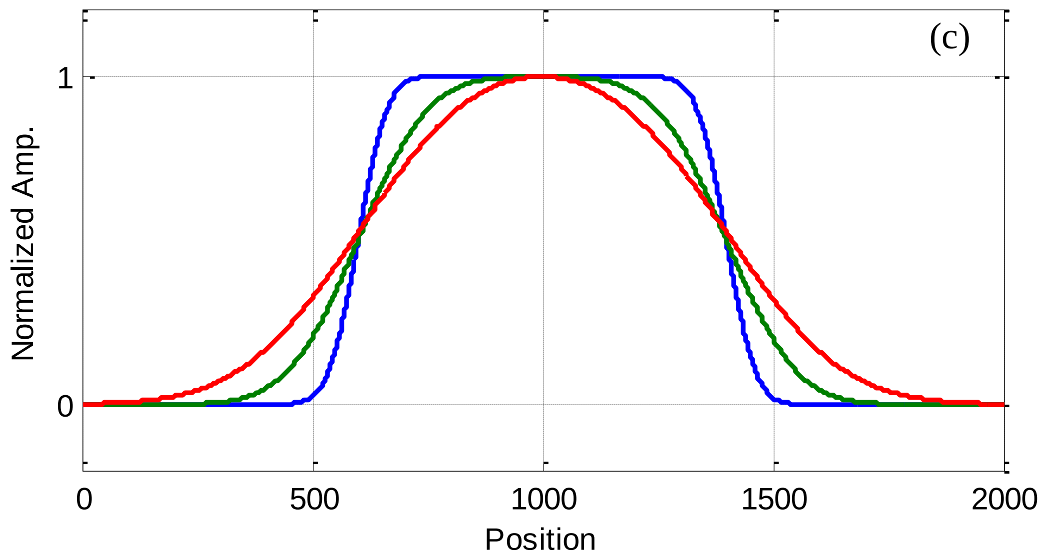
(c)
Normalized Amp.
1
0
0
500
1000
1500
2000
Position

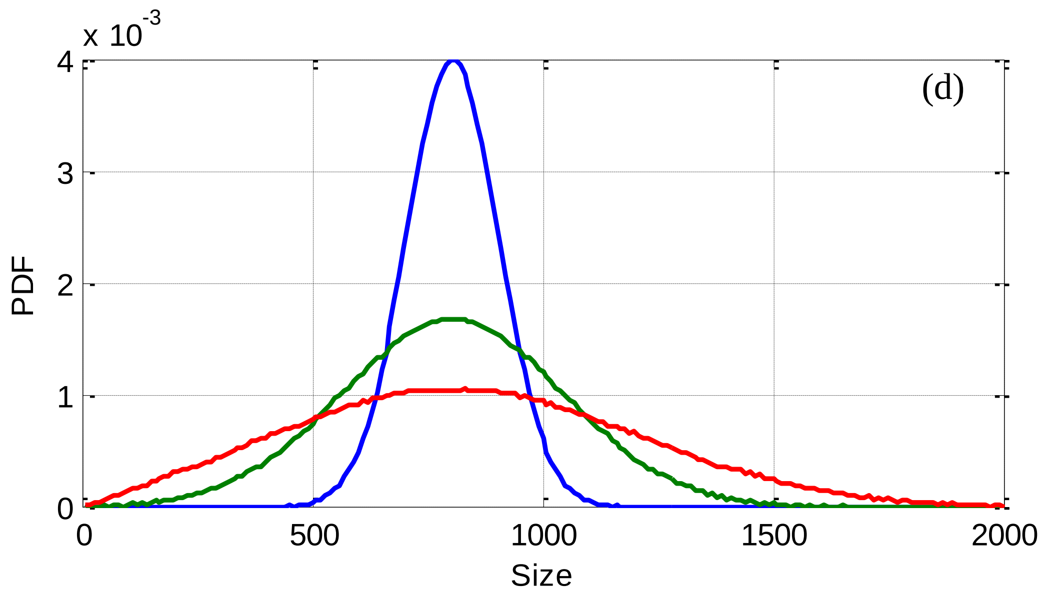
(d)
x 10^-3
PDF
4
3
2
1
0
0
500
1000
1500
2000
Size

For an extreme case where the idea detector is a unit impulse function, the procedure will have the sharpest resolution and can ideally detect the exactly damage boundary. The correlation response will be exactly the same as the normalized intensity curve itself, and the CDF is a step function starting from the damage length. Thus the PDF is the delta function located at the damage size. This phenomenon shows that the 3-step procedure for extracting PDF of damage size works for the ideal detecting techniques.

Four illustrative cases are given as shown in Figure 3-7 for comparison to evaluate the 3-step PDF extraction procedure. Case 1 and Case 2 are two intensity curves for two different damage sizes with the same detector resolution (standard resolution 50). Case 1 and Case 3 have the same damage but with different resolutions (standard deviation 50 and 120, respectively). Case 2 and Case 4 have the same damage size and resolution (standard resolution 50) but at different locations. Since the extracted PDF of Case 2 and Case 4 are exactly the same, the PDF curves are overlapped in the Figure 3-7(b). This is because the damage location has been eliminated in the 3-step procedure. Table 3-1 lists the similarity, dissimilarity and comments about the four cases. The comparison shows that the 3-step procedure can not only find the most possible size, but also indicate the confidence of estimation. Also, the location information is lost in the 3-step procedure, which cannot distinguish between two cracks with the same crack size but at different locations.

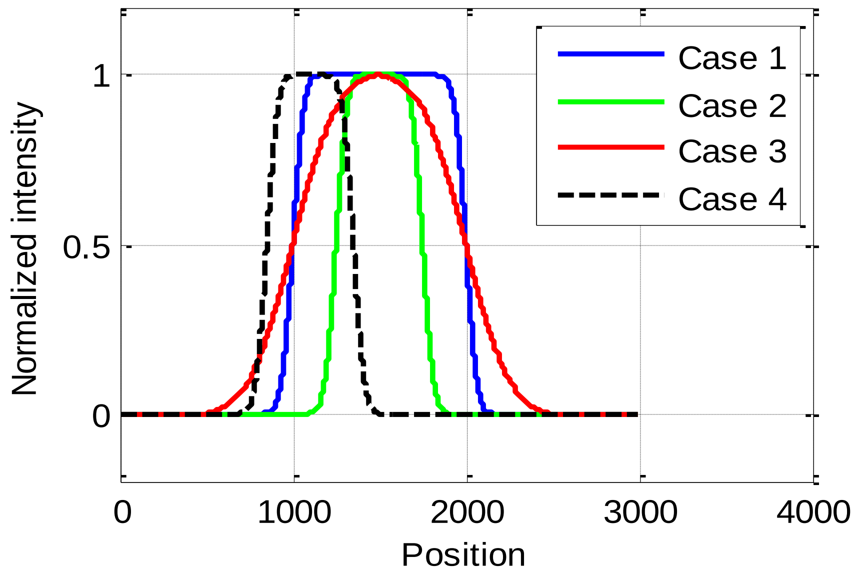

(a) Four illustrative intensity curves with different features

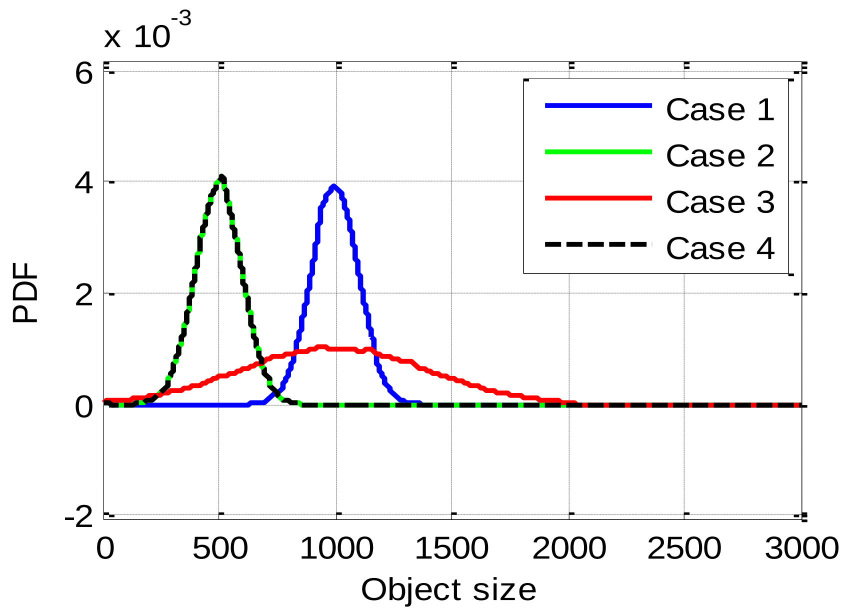

(b) Extracted PDF from the intensity curves

Figure 3-7. Four typical cases for comparison study.

Table 3-1. Comparison about four typical PDF extraction cases.

Case A	Case B	Similarity	Dissimilarity	Comments
1	2	Resolution location	Damage size	Sharper damage boundary leads to higher confidence in PDF
1	3	Damage size location	Resolution	Extracted PDFs indicate the damage size
2	4	Damage size resolution	Location	PDF extraction procedure ignores the information of damage location

3.3 Application for SHM

In this section, the 3-step PDF extraction procedure is applied to damage diagnostics. Paris law is used to model crack growth under a periodical fatigue loading. Two detecting methods, correlation-based detection (e.g. in the last section) and *f*-*k* migration imaging, are then used to illustrate the probabilistic damage sizing for the purpose of damage prognosis. Using simulated damage growth, the true damage sizes at different loading cycles are generated by Paris law. After obtaining the PDF by 3-step procedure, the distribution of RUL can be calculated based on the crack growth model.

The first detection method is the 1D correlation-based detection with the detector's standard deviation 120.

Figure 3-8 is the 1D correlation based intensity curves for seven crack sizes, which are calculated from crack growth model discussed in detail in Chapter 4. Figure 3-9 is the PDFs of damage size extracted from the intensity curves with the 3-step PDF extraction procedure. Since the intensity curves are calculated from the same transfer function, the shape of PDFs of damage sizes is similar, and this feature will be lost in the 2D imaging detection in the next subsection, because the limitation of the sensor number and data processing scheme will introduce more uncertainties.

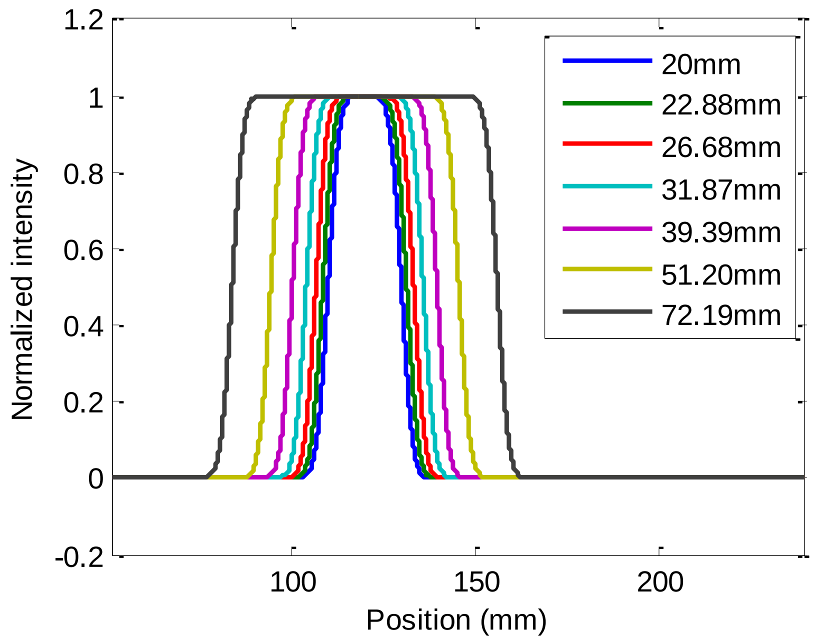

Figure 3-8. 1D correlation-based detection of given crack sizes.

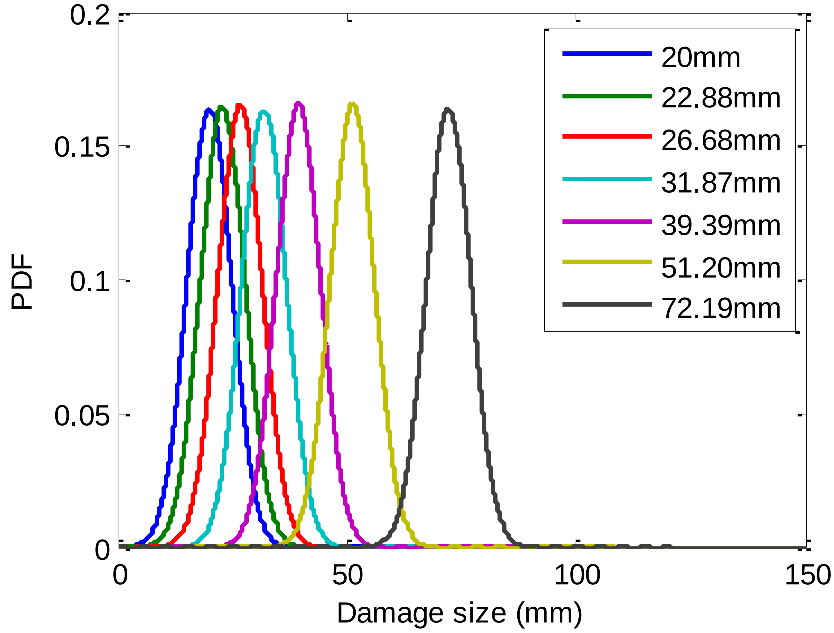

Figure 3-9. Extracted PDFs of crack size from correlation-based detection.

The second detection method is *f*-*k* migration imaging, which is 2D correlation-based damage detection method. The detail of this method can be traced back to the geology imaging [88] and the algorithm is developed for the purpose of SHM. The basic idea of migration procedure is that the image intensity can be represented by the cross-correlation of the excitation wave field and the scattered wave field propagating backwards. In this study, the central frequency of five-peaked tone-burst excitation, which is a typical temporal-spaced compactly-supported excitation for SHM Lamb wave detection, is 150 kHz[44].

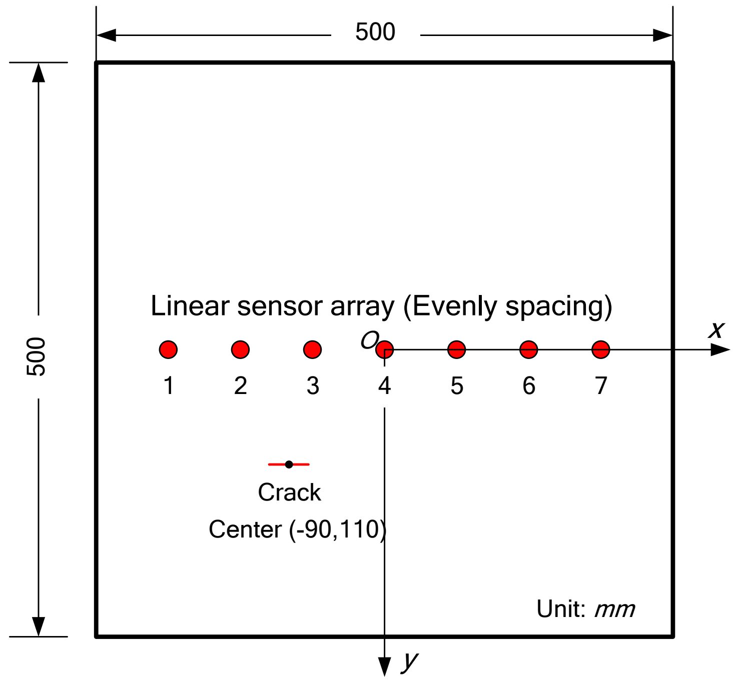

Figure 3-10. Geometric dimension of migration imaging.

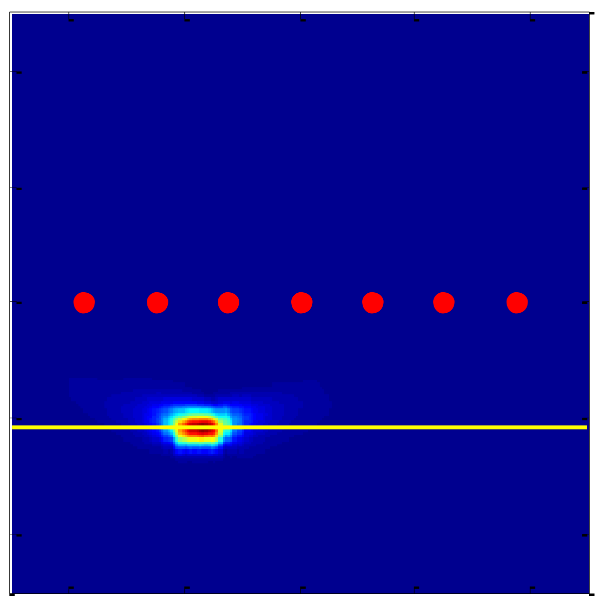

Figure 3-11. Migration image with a single crack.

The simulation to generate the damage image is carried out with the geometry as indicated in Figure 3-10, and the plate is made of aluminum with 500mm length, 500mm width and 3.2mm thickness. The origin of the coordinate is set at the center of the plate with the given coordinate system and seven sensors are evenly distributed along the x-axis. The center point of crack is set at point (-90mm, 110mm). With the crack sizes discussed in Table 4-2, the damage image can be generated from the migration algorithm. As observed, the 2D correlation-based damage images are not as good as the 1D correlation-based response because of the limitation of sensor number and the imaging algorithm. The intensity curves cut from the preset damage center of coordinate (-90mm, 110mm) are shown in Figure 3-12. With the 3-step procedure applied, the PDF of crack size is calculated and shown in Figure 3-13. It is observed that the estimated PDF of damage size becomes wider with damage propagating.

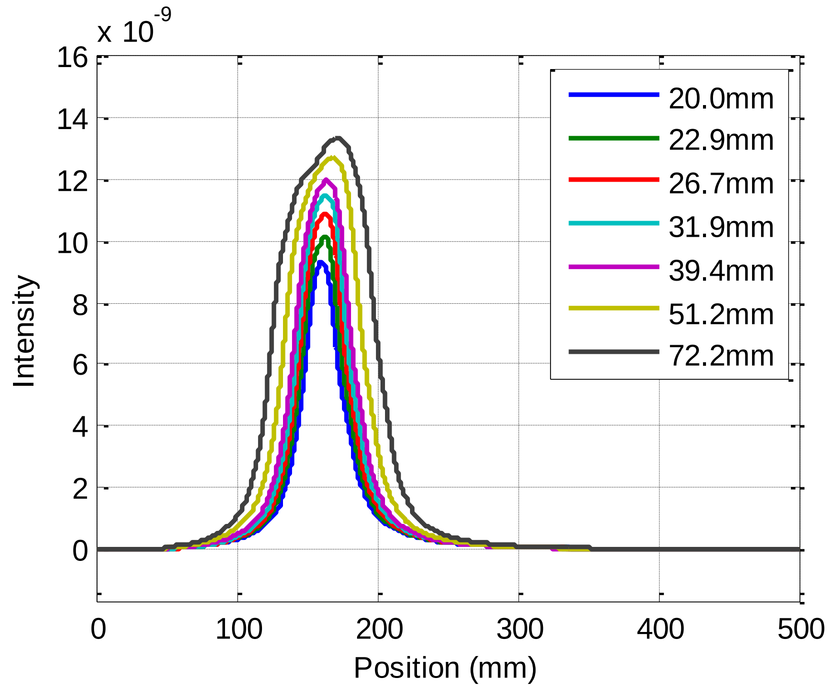

Figure 3-12. Intensity curves from the migration images.

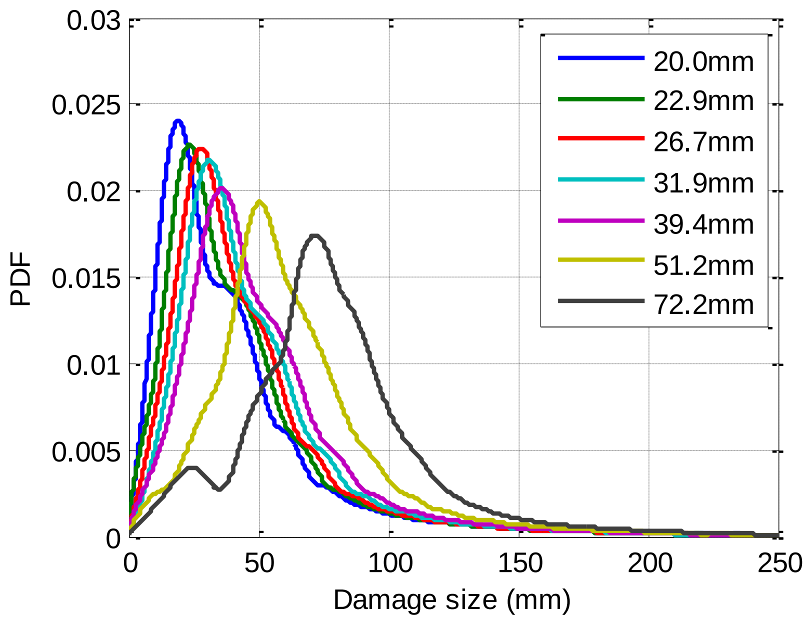

Figure 3-13. Extracted PDFs of damage size.

3.4 Improvements and Extensions

3.4.1 Improvement by Combined Gaussian Spaced Sampling

The distribution of crack size from the above 3-step procedure is widely applied in damage prognosis and model parameter updating[11]. A Gaussian modulated sampling ratio is designed to narrow the distribution of damage size. Figure 3-14 illustrates that the sampling ratio varies with the value of intensity. For the normalized intensity curve, when the sampling procedure is carried out with a varying sampling ratio with 0.5 mean and 0.05 standard deviation. The PDF of damage size can be obtained with the last two steps of the 3-step procedure.

Table 3-2 and Table 3-3 are the statistics of the obtained distribution from evenly spaced sampling and Gaussian modulated sampling. On the one hand, the PDF with evenly sampling rate can reflect the most likely (most possible) crack size accurately since evenly sampling rate takes an equal observation for the whole range of intensity curve, thus captures the information where the most possible damage size is. However, the 3-step procedure with evenly sampling rate introduces large deviation in the final probability density function because all the intensity levels are evenly sampled, thus introduces many samples with small size (e.g. at the high intensity level close to 1) and large size (e.g. at the low intensity level close to 0). These samples will disperse the obtained distribution of crack size.

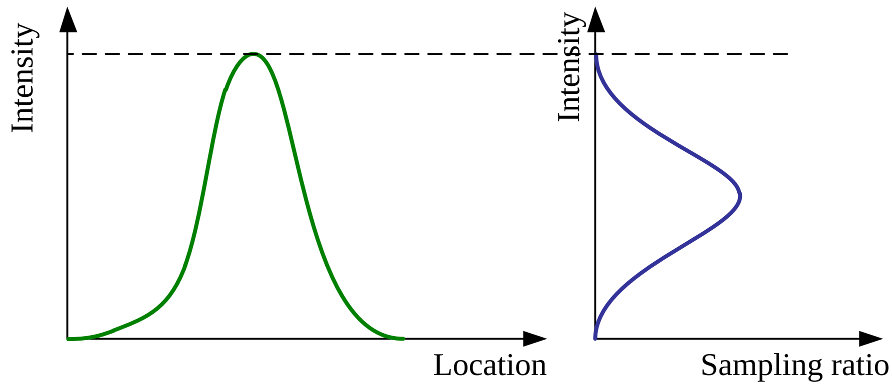

Figure 3-14. Illustration of Gaussian sampling ratio.

On the other hand, the PDFs from Gaussian modulated sampling ratio share small deviation of the distribution, because Gaussian modulated sampling assumes that the true crack size is close to the one with intensity value at 0.5, and the probability of damage size of zero (high intensity) or very large (low intensity) is very small. However, as we know, the true crack size does not have to be around where the intensity is 0.5. This is why Gaussian distributed sampling method introduces larger error in the PDF results.

The two sampling methods have their own advantages and disadvantages, thus a combined scheme is developed to take advantage of merit of each. First, use evenly sampling to find the max PDF crack size, focus on the max PDF, and then use Gaussian sampling to calculate the PDF of crack size. The statistics of the combined scheme shown in Table 3-4 indicate that the accuracy is enhanced and precision is highly improved.

Table 3-2. Statistical properties of evenly sampling method (Unit: *mm*).

True	***Max PDF***	***Mean***	***STD***
20.00	19	42.2	40.60
22.88	24	44.6	39.23
26.68	28	46.8	37.98
31.87	33	49.6	37.40
39.39	37	52.9	37.41
51.20	51	64.7	37.84
72.19	72	80.2	39.98

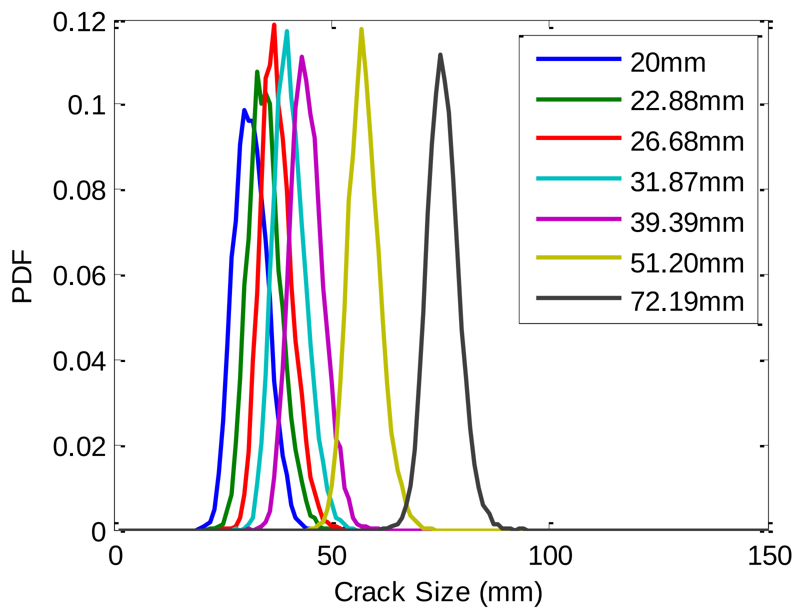

Figure 3-15. PDFs obtained from Gaussian sampling ratio.

Table 3-3. Statistical properties of Gaussian sampling method (Unit: *mm*).

True	***Max PDF***	***Mean***	***STD***
20	30	31.4	3.26
22.88	34	34.6	3.14
26.68	37	37.3	2.93
31.87	40	40.3	3.04
39.39	44	44.3	3.11
51.2	58	57.5	3.02
72.19	75	75.6	3.06

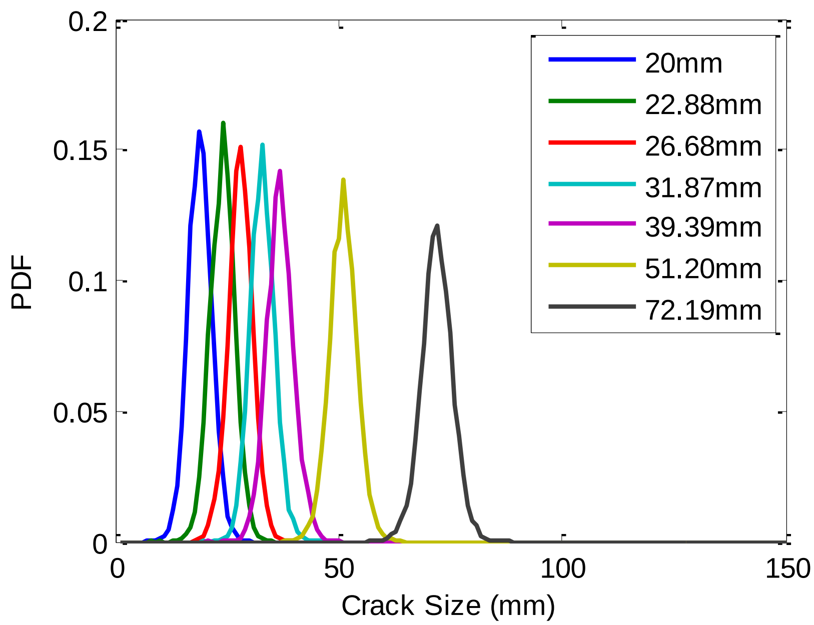

Figure 3-16. PDFs of damage size from combined method.

Table 3-4. Statistical properties of combined method (Unit: *mm*).

True	***Max PDF***	***Mean***	***STD***
20	19	19.1	2.23
22.88	24	24.2	2.21
26.68	28	28.2	2.36
31.87	33	33.0	2.34
39.39	37	36.9	2.54
51.2	51	51.0	2.64
72.19	72	72.0	2.96

3.4.2 Improvement by Morphological Gradient prior

The objective of introducing morphological gradient prior in this section is to obtain a narrower distribution of crack. It is known in the field of image processing the variations of the intensity characterize the object boundaries, which is located around the high variation regions. The variation of intensity can be represented by morphological gradient. For 2D image processing, the morphological gradient is two dimensional, however, the damage quantification from the intensity curve described in the previous sections is one dimensional. The objective boundaries are characterized by grey-level intensity transitions.

Gradient operators are generally used for edge detection because they enhance the intensity variation in the images. Rivest *et al.* gave a comprehensive survey about the morphological framework of the gradient operator[89]. Qu *et al.* developed a morphological gradient technique using directional component to detect and isolate the wafer detectors[90]. Angulo and Serra employed morphological approach to calculate the texture gradients, achieving the segmentation according to the textures[91]. Noyel *et al.* developed a general methodology for morphological segmentation of hyper-spectral images[92].

In this section, the morphological gradients are assumed to be correlated with the objective boundaries in the intensity curve, thus the morphological gradients of the curves are employed to govern the sampling procedure as discussed in the PDF extraction section. The basic idea of this implementation is that the gradients enhance high-frequency events, which may be caused by damage edges in the images.

Assume f is a differentiable function on the Euclidean plane $\boldsymbol{R}^2$. The gradient ∇ of f is the 2D vector, which can be defined as,

$$\nabla f = \left(\frac{\partial f}{\partial x}, \frac{\partial f}{\partial y} \right). \tag{3-10}$$

The modulus of the gradient is

$$\left| \nabla f \right| = \sqrt{\left(\frac{\partial f}{\partial x} \right)^2 + \left(\frac{\partial f}{\partial y} \right)^2}. \tag{3-11}$$

The azimuth of the gradient is

$$\mathrm{dir}(f) = \arctan\left[\left(\frac{\partial f}{\partial y} \right) \Big/ \left(\frac{\partial f}{\partial x} \right) \right]. \tag{3-12}$$

And the morphological gradient g of a is defined as,

$$g(x) = \lim_{\rho \to 0} \frac{\delta_{\rho B}(f) - \varepsilon_{\rho B}(f)}{2\rho}, \tag{3-13}$$

where $\delta_{\rho B}(f)$ is the dilation of f with a disk of radius ρ, and $\varepsilon_{\rho B}(f)$ is the erosion of f of the same disk. Dilation and erosion are basic morphological operations. Dilation adds pixels to the boundaries of the objects in an image, while erosion removes pixels on the object boundaries. The number of pixels added or removed from the objects in an image depends on the size and shape of the structuring element used to process the image. In the morphological dilation and erosion operations, the state of any given pixel in the output image is determined by applying a rule to the corresponding pixel and its neighbors in the input image. The rule used to process the pixels defines the operation as dilation or erosion.

For 1D intensity curve depicted in Figure 3-17, the gradient is only considered along the *x*-direction. The gradient of the intensity curve can be simplified as

$$\begin{aligned} g(x) &= \left|\nabla I(x)\right|, \\ &= \lim_{\sigma \to 0} \left| \frac{I(x_0 + \Delta x) - I(x_0 - \Delta x)}{2\Delta x} \right|. \end{aligned} \tag{3-14}$$

The objective of the PDF extraction procedure is to obtain the crack size represented by the intensity curve. Observations show that the crack boundaries reside around the regions with large values of gradients, such as the transition regions e_1 and e_2 as shown in Figure 3-17(a). Figure 3-17(b) gives the intensity curve and its corresponding gradient function. Those with small values of gradient are less possible to be the true crack size.

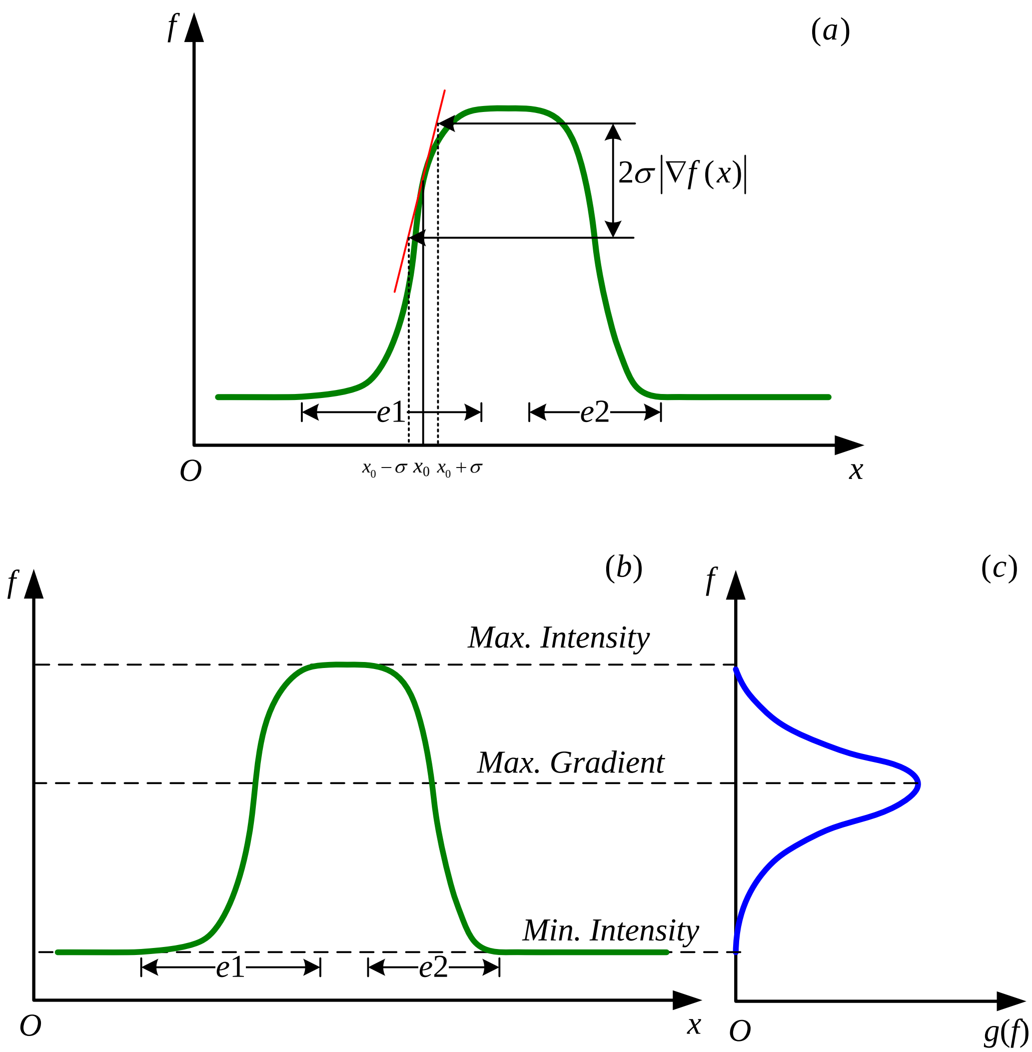

Figure 3-17. Gradient definition on a 1D intensity curve.

The evenly sampling procedure assumes that the probability of the crack sizes equaling to all possible size is the same. However, the edge of crack resides in the higher gradient regions more possibly than in the lower gradient regions. The morphological gradient enhances the intensity variation, so the gradient will be employed to govern the sampling procedure to focus on the observation to the crack edge regions in the Bayesian framework.

Due to the assumption that the damage boundary or damage edge is close to the high gradient region in the intensity range, the morphological gradient is employed in the following study as prior information to narrow the distribution of damage size in the Bayesian updating framework as in Eq.(3-15),

$$p(b \mid s) = \frac{p(s \mid b)\, p(b)}{p(s)}, \tag{3-15}$$

where $p(b)$ is the prior function, which is the PDF of the crack size at each intensity level before the observation (e.g. evenly spaced sampling). The prior is defined as the summation of the morphological gradients at the increment and decrement. $p(s \mid b)$ is the observed sample number from equally spaced sampling at each intensity level. And $p(b \mid s)$ is the posterior probability, which is the PDF of crack size at each intensity level after the observation (evenly spaced sampling). $p(s)$ is the normalization item. Eq. (3-15) updates the PDF of crack size at each intensity level by the observation of evenly spaced sampling. In other words, the morphological gradient reflects the probability of the damage edge at crack size of each intensity level. For practical computation, it should be noticed that the crack sizes of each intensity level is non-linear.

$$p(b) = \frac{g(f(x))}{G(f)}, \tag{3-16}$$

where $g(f)$ is gradient function, and $G(f)$ is the normalized item.

For the images with the same crack size as used in section 3.3, the distribution of crack size can be obtained as shown in Figure 3-18. The statistics of these distributions are shown in Table 3-5. The standard deviation is around 4mm, which is highly improved by 3-step procedure (standard deviation is around 40mm) investigated in section 3.2. Therefore, the morphological gradient prior introduced by Bayesian updating highly improves the PDF extraction procedure for damage sizing. Furthermore, as observed in Table 3-5, the most likely crack sizes (also Maximum PDF crack sizes) are more conservative than estimation from the original 3-step procedure.

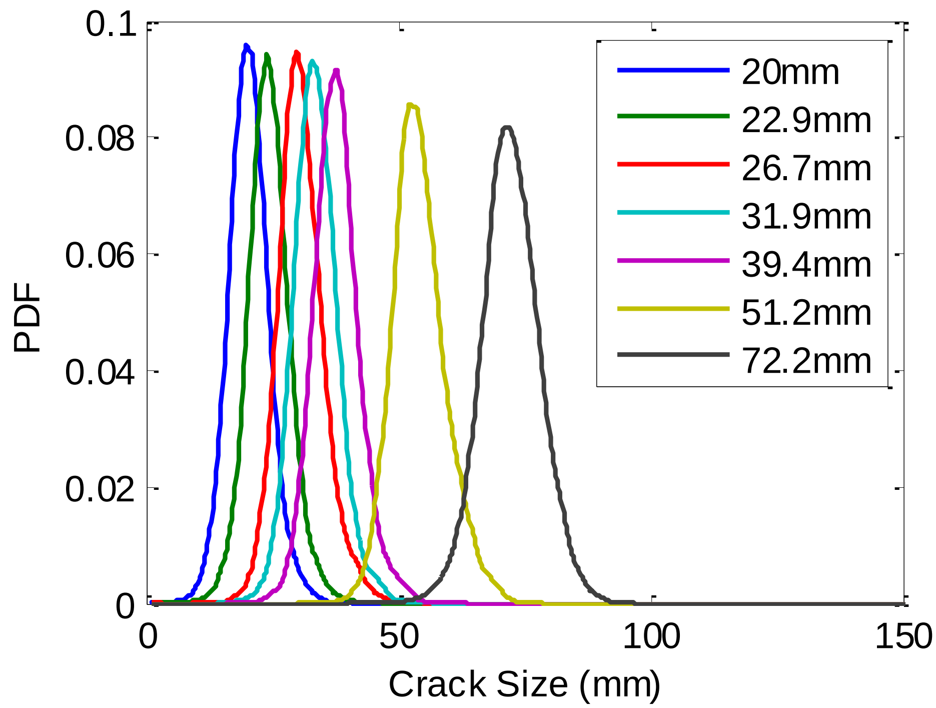

Figure 3-18. Distribution of crack size with gradient prior.

Table 3-5. Statistical properties of distribution with gradient prior (Unit: *mm*).

True	***Max PDF***	***Mean***	***STD***
20	21.8	21.9	3.06
22.88	23.6	23.9	3.28
26.68	27.8	27.8	3.84
31.87	32.8	33.0	4.23
39.39	36.8	36.9	4.68
51.2	51.0	51.0	4.92
72.19	72.1	72.1	5.02

3.4.3 Extension to 2D PDF of damage region

Since the purpose of our research is to provide the PDF of crack size for damage prognosis, the 2D image is reduced to 1D curve by a simple cut along the crack orientation with image processing algorithm, such as ridge detection, which can track the curvature of ridges in images.

In order to extend the PDF method to more general applications, the PDF of damage area can be obtained through a similar procedure. A minor variation from the previous 1D intensity curves is that what we measure now is not the crack length but the damage area.

Figure 3-19 (a) is a migration image with damage for PDF extraction. The samples of damage area can be collected as described in the first step.

Figure 3-19 (b) is the constructed CDF using empirical CDF (ECDF) method and

Figure 3-19 (c) is the converted PDF. The units are pixels, and the size of each pixel is 2.5mm by 2.5mm. Therefore, the result indicates the probability of damaged area. The PDF extraction procedure for obtaining PDF of damage area can be used to determine the damage size for metal corrosion or composite delamination.

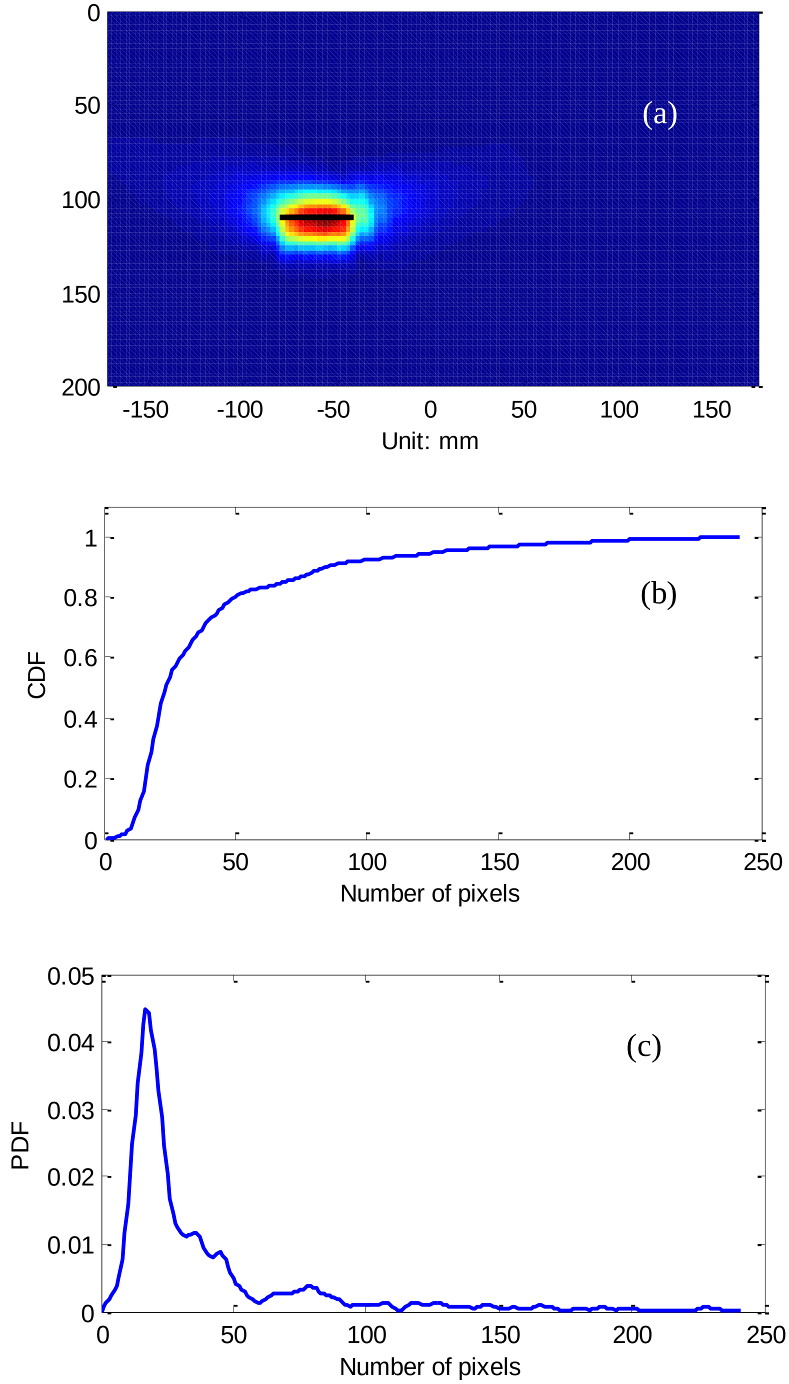

Figure 3-19. Extracted PDF of damage region.

Besides the application in the field of structural health monitoring, this PDF extraction procedure can also be adopted in other image processing fields, e.g. medical image processing to determine the probabilistic tumor size, cancer area, bone size, and etc.

3.5 Summary

The 3-step PDF extraction method was proposed for quantifying local damage in airframe structures in probabilistic manner, and two improving measures with Gaussian sampling method or gradient-based prior are developed to narrow the distribution. With the obtained PDF, the probability of damage size larger than the pre-defined critical damage size can be calculated. The results also provide probabilistic measurements for damage prognosis in the framework of structure health management by calculating the distribution of the remaining useful life. This procedure operates on the images and quantifies the characteristics with probabilistic concepts. However through this procedure the location of the damage will be ignored. The probabilistic PDF extraction method discussed in this paper can be extended to 2D and 3D problems. The following conclusions may be drawn:

1) The PDF extraction procedure is from the collected data, which implies that no standard model (e.g. Lognormal distribution, or Gaussian distribution) is assumed;
2) The distribution of damage size is quantified from one image, indicating the damage information and resolution of the detection;

3) The entire 3-step procedure is intuitive and easy to implement;
4) The proposed PDF extraction method also provides a framework for selecting the best damage imaging technique;
5) Different resolutions of images can lead to different PDFs for the same damage, and improving the damage imaging technique will yield high-reliability damage sizing;
6) The PDF of damage size from the morphological gradient prior enhanced PDF extraction is ready for updating in the post-procedure under the Bayesian framework to improve the accuracy and precision of the on-line detection. The damage size and material parameters in Paris law can be updated simultaneously.

4 Damage Prognosis

4.1 Paris Law for Crack Growth

Aircraft structures are experiencing fatigue loading, periodically or non-periodically. In this work, the periodical fatigue loading is studied for its simplicity and predictability. For periodical fatigue loading, it is possible to model the crack growth under various loading conditions. Although many crack growth models are available in the literatures[93-98], a simple Paris model [62] is used in this paper to show how the PDF of damage size can be applied for damage prognosis. According to the Paris law the crack growth under Model-I fatigue loading condition can be described as:

$$\frac{da}{dN} = C(\Delta K(a))^m, \tag{3-17}$$

$$\Delta K(a) = \sigma\sqrt{\pi a}, \tag{3-18}$$

where:

a is the half crack size,

N is the fatigue loading cycles,

$\Delta K(a)$ is the range of the stress intensity factor (SIF) in loading cycles,

σ is the stress differential in the structure,

and C and m are structural or material parameters determined experimentally.

However, it is difficult to obtain specific C and m for each panel on the airframe due to large amount of panels and the geometrical complexity of the panels. Coppe *et al.*[11] developed a parameter updating method based on the Bayesian framework. It is essential to have a good estimation of damage size while carrying out the parameter updating, where a probabilistic damage estimation method is developed in Chapter 3. Before the procedure of damage prognostics, the relationship of fatigue loading cycle and the growth of crack size from Paris Law will be deducted as shown in the following.

Substitute Eq.(3-18) into Eq. (3-17),

$$\frac{da}{dN} = C(\sigma\sqrt{\pi a})^m. \tag{3-19}$$

When $a = a_c$,where a_c is the critical crack size), the corresponding loading cycle is N, which relates to the remaining useful life. Therefore, the remaining useful life can be calculated as given in Eq.(3-20), with the initial loading cycle N_0, the critical half crack size a_c, and the initial half crack size a_0:

$$N - N_0 = \frac{a_c^{1-\frac{m}{2}} - a_0^{1-\frac{m}{2}}}{C(1-\frac{m}{2})(\sigma\sqrt{\pi})^m}. \tag{3-20}$$

Through rearrangement of Eq. (3-20), the half crack size at the Nth cycles, a_N, can be obtained as a function of the initial half crack size a_0 at N_0 cycles,

$$a_N = \left((N - N_0)(1-\frac{m}{2})(\sigma\sqrt{\pi})^2 + a_0^{1-\frac{m}{2}} \right)^{\frac{2}{2-m}}. \tag{3-21}$$

Thus, from Eq.(3-21) and Eq.(3-20), the remaining loading cycles can be obtained when the critical crack size, loading condition and model parameters are given, and the crack size can also be calculated once the loading cycles, loading condition and model parameters are given.

To simulate the true crack size of a given plate structure under fatigue loading experiment for further evaluating the estimation and prediction, a series of crack size is obtained as in Table 4-2 by substituting these parameters into Eq. (3-21) with parameters listed in Table 4-1.

Table 4-1. Simulation input parameters for Paris law.

Parameters	***Values***
C	1.5×10^{-10}
σ	60.9 MPa
a_0	10 *mm*
m	3.8
ΔN	1000

Table 4-2. Crack sizes calculated from Paris law.

Loading Cycles	0	1000	2000	3000	4000	5000	6000
Crack Size (*mm*)	20.0	22.9	26.7	31.9	39.4	51.2	72.2

The critical crack size, which is the maximum crack size of the simulation, can be calculated as Eq. (3-22),

$$a_c = \left(\frac{K_{IC}}{\sigma\sqrt{\pi}} \right)^2. \tag{3-22}$$

where K_{IC} is the plane-strain fracture toughness, which represents the ability of the material to resist fracture in the presence of cracks.

In the last chapter, the distribution of crack size are obtained by the proposed 3-step procedure, at the meantime, the samples or seed of the resultant distribution are provided in the PDF extraction. The samples of RUL can be obtained first by substituting the crack sizes from the PDF extraction procedure into a_0 in Eq.(3-20) to yield samples of RUL ($N - N_0$). Then by following the second and the third steps, the PDF of RUL can also be constructed, thus obtain the distribution of remaining useful life. For the distribution with the morphological gradient prior, the seeds can be generated by the distribution of crack size by random number generator.

4.2 Distribution Updating

Improving estimation of damage size and prediction of remaining useful life is of much importance. For the method employing damage imaging technique, when the damage is detected, the improvement of damage estimation and RUL prediction reside on two angles,

(1) Improving the damage estimation algorithm. Chapter 2 and Chapter 3 are mainly focus on this angle.

(2) Updating the current information and previous detected information. (Which Chapter is mainly focus on this?)

Bayesian updating, as we discussed before, is one of the most promising data fusion techniques to update the distribution of damage size, narrowing the distribution and providing more confidential results. Bayesian updating theory has been discussed in Chapter 2 in detail. Figure 4-1 gives an illustration of Bayesian-based distribution updating procedure. The solid line is the prior distribution which is from knowledge before the observation or detection; the dash line is the observed likelihood, which is of low confidence. However, after the Bayesian updating, the result is narrowed as indicated as the dash-point line.

4.3 Enhance Diagnostics with Prognostics

In this section, the damage propagation model and the current estimation are used to predict the distribution in the near future. And the prediction then will be employed to improve the future detection under the framework of Bayesian updating. Undertaking the fatigue loading as discussed in the previous study, seven detections/measurements are carried out to image the damage using *f-k* migration technique. The intensity curves are cut at the global maximum point horizontally. Seven intensity curves are obtained from seven intensity images, and a morphological gradient prior enhanced PDF extraction method is designed to extract the PDF of damage size. To improve the precision of diagnosis, Bayesian updating is employed in the following study to introduce the previous information as a prior.

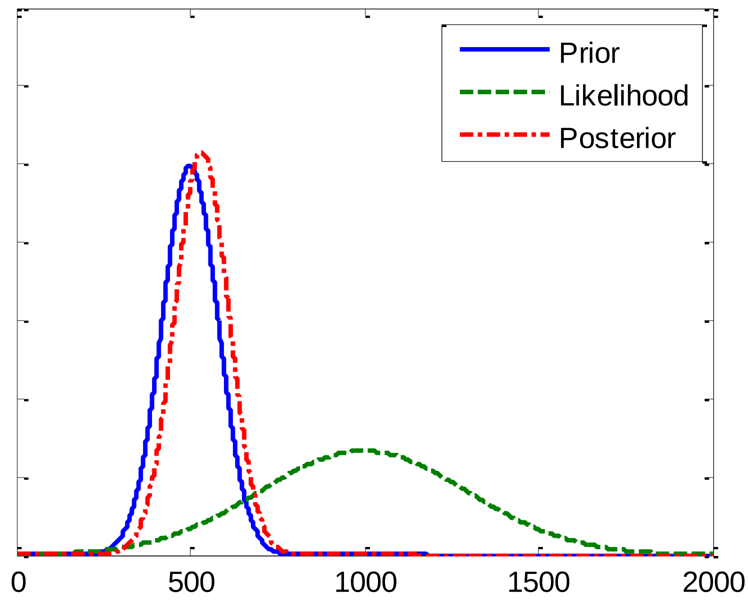

Figure 4-1. Demonstration of Bayesian updating for narrowing distribution.

According to the Bayesian equation,

$$p(x \mid y) = \frac{p(y \mid x)\,p(x)}{p(y)}. \tag{3-23}$$

where, $p(y|x)$ is defined the current observation, which is the current distribution of crack size;

$p(x)$ is prior information, which is the distribution of crack size from the previous detection and damage growth model;

$p(x|y)$ is the posterior, which indicate the distribution of crack size combining the current observation and prior information;

and $p(y)$ is a normalized item to make sure the probability density function unity.

The damage growth model used here is Paris law. The measurements are carried out up to 6000 cycles with 1000 increment each time. Table 4-3 listed the loading cycles applied, and the true crack sizes at the beginning and the end of the duration. Figure 4-2 to Figure 4-7 give the procedure of crack growth and corresponding estimation by Bayesian updating. As observed, the distributions after Bayesian updating is narrower than the ones before Bayesian updating, and the most possible estimated crack size is corrected by the previous detection and the Paris model. Table 4-4 shows the comparison between the most possible crack sizes before and after using the prognostics model.

Table 4-3. True crack size growth under fatigue simulation.

Duration	Loading Cycles	Crack Growth
Period 1	0-1000	'20mm'-->'22.88mm'
Period 2	1001-2000	'22.88mm'-->'26.68mm'
Period 3	2001-3000	'26.68mm'-->'31.87mm'
Period 4	3001-4000	'31.87mm'-->'39.39mm'
Period 5	4001-5000	'39.39mm'-->'51.20mm'
Period 6	5001-6000	'51.20mm'-->'72.19mm'

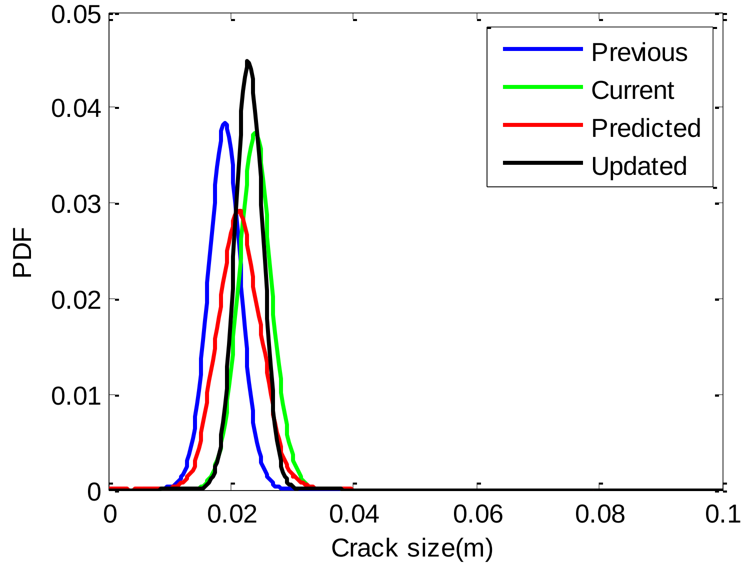

Figure 4-2. Bayesian-based crack size updating for *Period 1 :* '20mm'-->'22.88mm'.

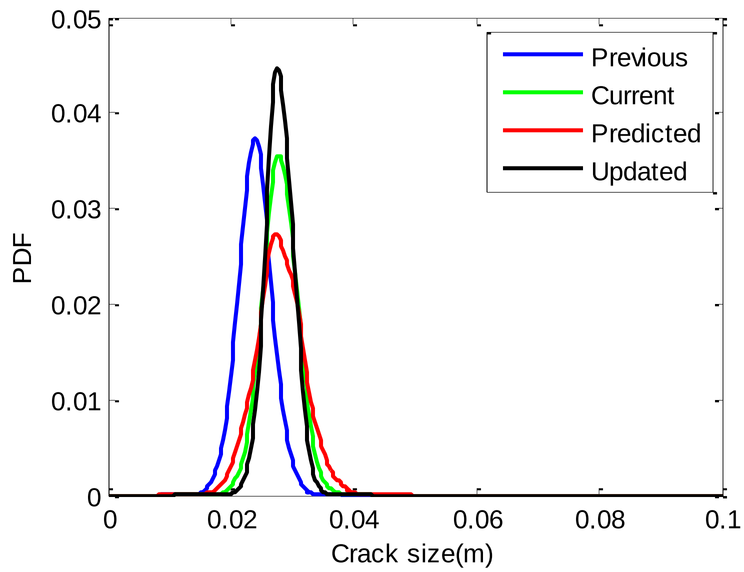

Figure 4-3. Bayesian-based crack size updating for *Period 2 :*'22.88mm'-->'26.68mm'.

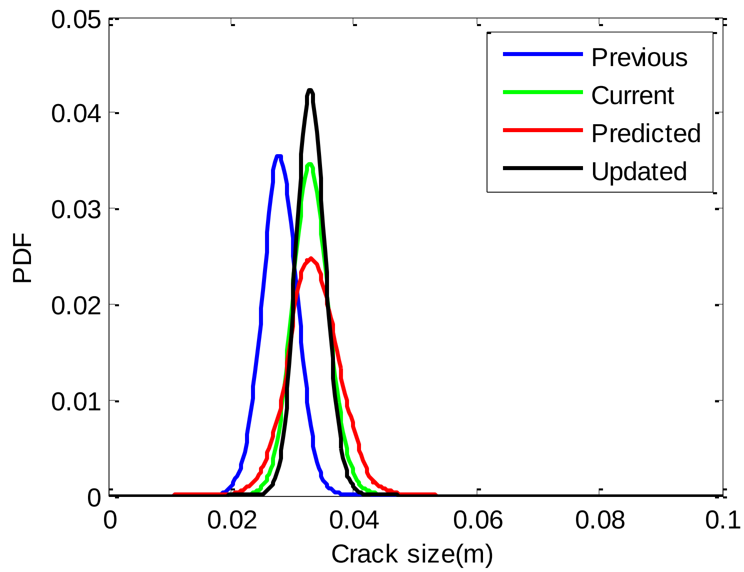

Figure 4-4. Bayesian-based crack size updating for *Period 3 :*'26.68mm'-->'31.87mm'.

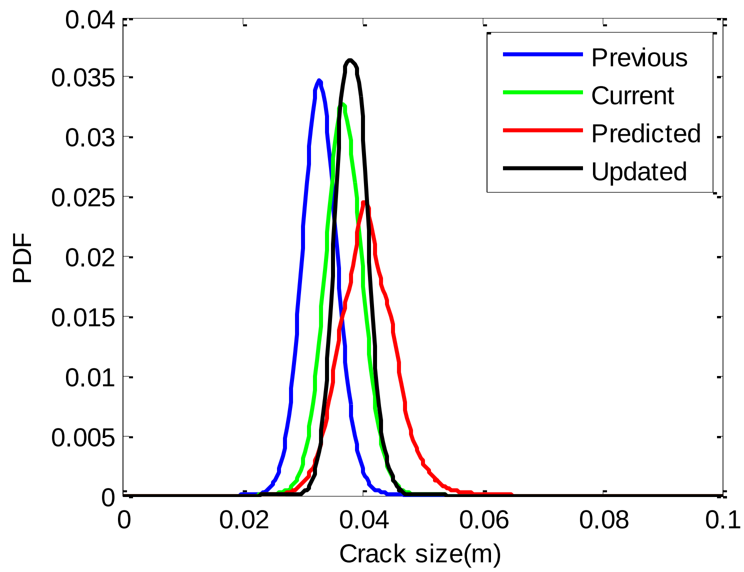

Figure 4-5. Bayesian-based crack size updating for *Period 4 :*'31.87mm'-->'39.39mm'.

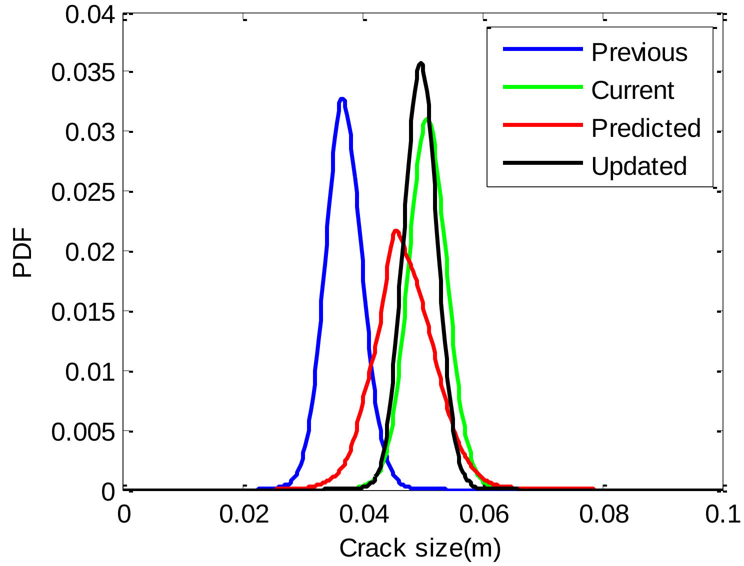

Figure 4-6. Bayesian-based crack size updating for *Period 5 :*'39.39mm'-->'51.20mm'.

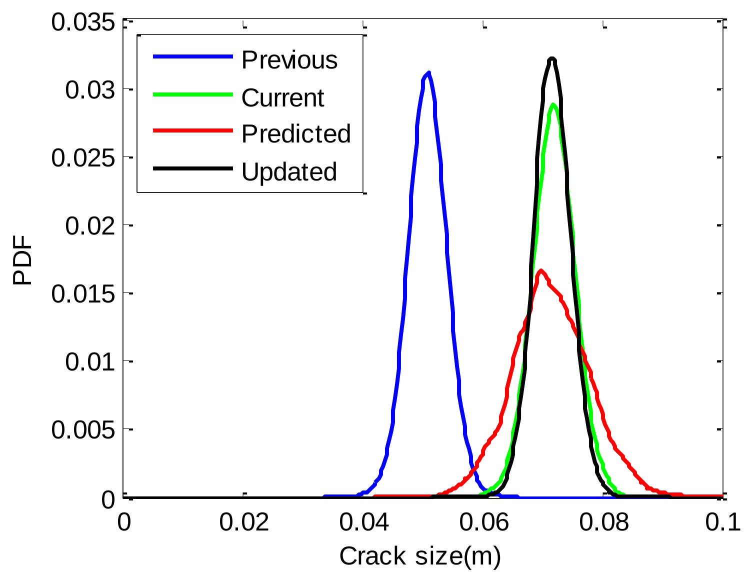

Figure 4-7. Bayesian-based crack size updating for *Period 6 :*'51.20mm'-->'72.19mm'.

Table 4-4. Comparison of estimated crack size before and after Bayesian updating.

Loading Cycle	**True crack size** (*mm*)	**Before Bayesian** (*mm*)	**After Bayesian** (*mm*)
1000	22.88	24.0	22.8
2000	26.68	27.8	27.5
3000	31.87	32.8	32.8
4000	39.39	36.8	38.1
5000	51.20	51.0	49.8
6000	72.19	72.1	72.1

4.4 Remaining Useful Life Prediction

In Chapter 2, the distribution of crack size can be achieved by a 3-step procedure as the form of PDFs, accompanied with the samples following the corresponding distribution. The samples of crack size can be substituted into Eq. (3-20) to calculate the samples of remaining useful life and total structural life. Using the last two steps of the 3-step procedure proposed in Chapter 2, the distribution of remaining useful life and total structural life can be achieved using the obtained samples. Since the remaining useful life is decaying while the total structural life is converged to the designed structural failure time, distribution of total structural life is selected to validate the performance of the whole procedure.

For the 1D correlation-based detection method described in Section 3.2, the total life of structure can be calculated as indicated in Section 3.3. Since the intensity curves are calculated from the same transfer function, the PDFs of damage sizes are similar. Note that this feature will be lost in the 2D imaging detection in the next subsection, because the limitation of the sensor number and data processing scheme will introduce other uncertainties. The distribution of total structural life is narrowed and approaches the true value as show in Figure 4-8. Figure 4-9 shows the RUL with 90% confidence.

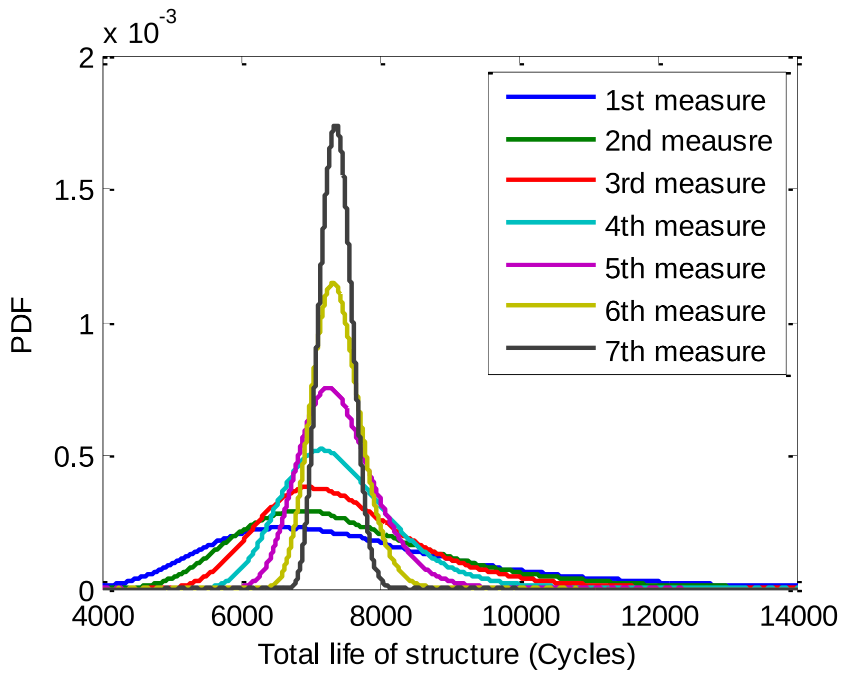

Figure 4-8. Total structure life convergence with correlation-based detection.

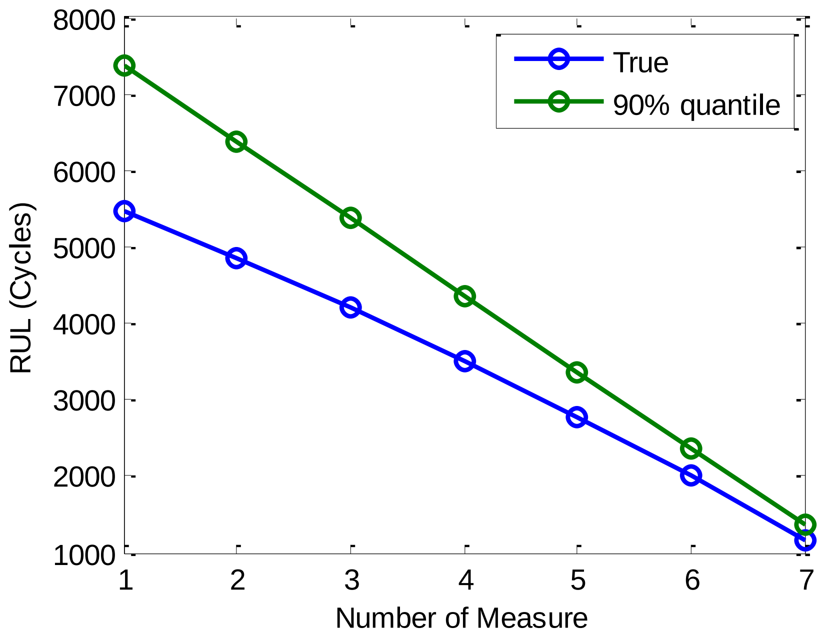

Figure 4-9. RUL with 90% confidence from correlation-based detection.

For the migration imaging method, the total life of structure can be obtained as shown in Figure 4-10. When the damage propagates, the PDF of damage size becomes wider as indicated in Figure 3-13. However, the RUL or total life of structure is narrowed and approaches the true value. Figure 4-11 shows the RUL with 90% confidence. Table 4-5 lists the remaining loading cycles after each inspection, and the total life of the structure, which converges to the true structural life, i.e. 7367 life cycles. These results show that continually detection and cumulating information for online SHM system increases not only the precision but also the accuracy of the structural condition prediction.

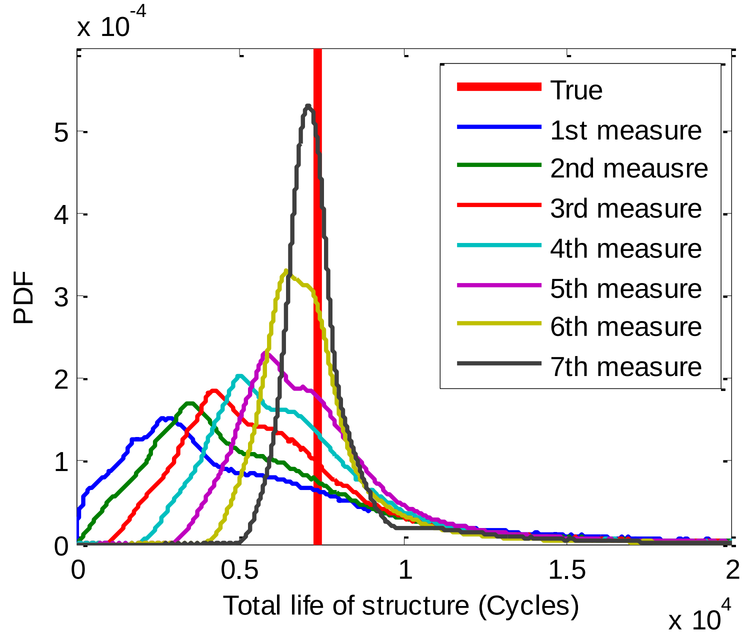

Figure 4-10. Distribution of remaining useful life by migration imaging results.

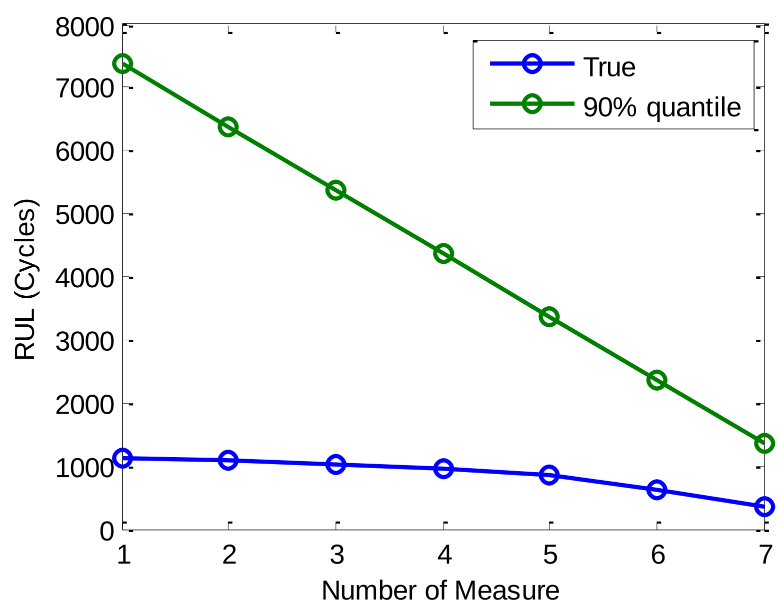

Figure 4-11. RUL with 90% confidence by migration imaging results.

Table 4-5. Convergence of total life of the structure (Unit: cycles).

Applied Cycles	**RUL**	**Total**	**Error %**
0	2936	2936	60.15
1000	2438	3438	53.33
2000	2273	4273	42.00
3000	2065	5065	31.25
4000	1832	5832	20.84
5000	1449	6449	12.46
6000	1115	7115	3.42

* True value of total life of structure is N=7367.

The extracted PDFs of damage size well reflect the true damage size, and the RUL converges to the structural life under a certain loading. However, during the calculation of the RUL, the uncertainty of parameters in Eq. (3-20) may lead to distorted PDF of the RUL. Multivariable Bayesian updating is suggested here since it has the potential to narrow the distribution, therefore to achieve more reliable estimation for future study.

5 Conclusions and Future Work

5.1 Conclusions

For the purpose of structural health management, damage diagnostics and prognostics are two major topics in this study. As a summary of this work, the following several parts of integrated structural health management system are mainly investigated.

(1) A Bayesian-based damage segmentation method with Markov random field (MRF) is developed for the purpose of separating damage region from the image background. Compared with the conversional *k*-means segmentation method, the Bayesian-based segmentation method is noise resistible, and more accurate. Before the damage segmentation, a histogram-based damage identification procedure is suggested to confirm the existence of damage in the SHM images.

(2) A 3-step procedure is developed to probabilistically quantify the damage size in the image obtained from the SHM system. The procedure is intuitive and easy to implement. Several examples, including ideal detecting method, and four comparative cases, are given to verify the proposed method. It is also applied to *f*-*k* migration imaging results, and the extracted PDF curves not only reflect the most possible damage size but also provide the confidence of estimation.

(3) Morphological gradient prior is introduced in the Bayesian framework to enhance the distribution from the 3-step procedure, thus reduce the uncertainty of damage estimation. The morphological gradient prior emphasizes the high

frequency/fast variation region in the images, so distribution obtained focuses around the region of the true crack size, highly narrowing the distribution and improving the estimation accuracy.

(4) Damage prognosis based on the probabilistic damage estimation is carried out with a damage propagation model – Paris Law. The remaining useful life is calculated based on the crack size distribution and the Paris model. The results show that the proposed damage estimation provides good input for the damage prognosis, in which distribution of the remaining useful life converges to its true value.

(5) The damage diagnostics procedure has been improved using the prognostics. The distribution of crack size detected by imaging, and quantified by morphological gradient prior enhanced PDF extraction procedure is updated with the predicted distribution from the previous detection in the Bayesian framework, and the updated estimation gives more conservative estimation with higher confidence.

5.2 Future Work

Possible future studies are suggested as following for the successive researchers on damage prognosis for the purpose of structural health management system based on damage imaging techniques. To make the validation procedure clear, parts of the damage model in my study is assumed to be determined. However, in practical procedure of damage prognosis, there are uncertainty in the input and the model themselves, e.g. the loading conditions, and the model parameters.

5.2.1 *Uncertainty of Loading*

Loads applied to the practical structures cannot be treated as deterministic in practice. Generally, statistical information can be measured with certain loading conditions, and furthermore, there may be accidental events applying non-ignorable load on the structures, and these loading events may lead to the structure fail immediately. For those accidental events, it is not included in the study of the structure remaining useful life prediction. However, for those statistically known fatigue loading conditions, it is possible to predict the structure remaining useful life with certain complicated models which is not included in this thesis.

5.2.2 *Multivariable Optimization*

For a certain material, the damage growth parameters, such as the m and C mentioned in Chapter 3, are given. However, it is not possible for user to measure each damage parameter for a specified airframe and a specified panel on a specified airframe. These damage growth parameters can be reflected by the damage images detected. Multivariable optimization can be carried out to optimize the estimation for both current damage size and parameters in damage propagation models.

5.2.3 *Condition Controlled Diagnostics*

In current study, the detections are carried out with pre-defined intervals (1000 loading cycles). At the beginning of the structural life, the increment of the crack size is hard to be distinguished, while during the period close to the end life of the structure, the speed of the crack growth is too fast to guarantee the safety issue. Therefore, it is dangerous to use the same sampling interval for damage detection in practice. The condition-controlled diagnostics can be carried out based on the current detection and the prediction model. The parameters in the model may be selected randomly at the beginning; however, with more data available, the model will be more and more accurate in reflecting the real structure state. Thus, it is possible to use the same crack growth to determine inspection intervals. And this type of detection has the potential to increase the frequency of diagnostics during the high crack growth period, and thus to decrease the safety risk.

References

[1] P. C. Hoffman, "Fleet Management Issues and Technology Needs," *International Journal of Fatigue,* vol. 31, pp. 1631-1637, 2009.

[2] R. J. Gran, F. D. O. Jr., P. C. Paris, G. R. Irwin, *et al.*, "Investigation and Analysis Development of Early Life Aircraft Structural Failures," Universal Technology Corp.1971.

[3] J. J. Coleman, "Reliability of Aircraft Structures in Resisting Chance Failure," *Operations Research,* vol. 7, pp. 639-645, 1959.

[4] C. Boller, F. K. Chang, and Y. Fujino, *Encyclopedia of Structural Health Monitoring*: John Wiley & Sons, 2009.

[5] D. White and R. Vaughan, "Fleet Usage Monitoring is Essential in Improving Aging U.S. Helicopter Safety, Availability, and Affordability," *the 9th joint FAA/DoD/NASA Aging Aircraft Conference,* 2006.

[6] L. Fixter and C. Williamson, "State of the Art Review -- Structural Health Monitoring," *QINETIQ/S&DU/T&P/E&M/TR0601122,* 2006.

[7] J. D. Achenbach, "Structural Health Monitoring - What Is the Prescription?," *Mechanics Research Communications,* vol. 36, pp. 137-142, 2009.

[8] D. J. Inman, C. R. Farrar, V. L. Junior, and V. S. Junior, *Damage Prognosis: For Aerospace, Civil and Mechanical Systems*: Wiley, 2005.

[9] S. W. Doebling and F. M. Hemez, "Overview of Uncertainty Assessment for Structural Health Monitoring," *The 3rd International Workshop on Structural Health Monitoring,* Stanford, USA, 2001.

[10] Y. K. Lin and J. N. Yang, "A Stochastic Theory of Fatigue Crack Propagation," *AIAA Journal,* vol. 23, pp. 117-124, 1985.

[11] A. Coppe, R. T. Haftka, and N. H. Kim, "Optimization of Distribution Parameters for Estimating Probability of Crack Detection," *AIAA Journal of Aircraft,* vol. 46, pp. 2090-2097, 2009.

[12] D. Banjevic and A. K. S. Jardine, "Calculation of Reliability Function and Remaining Useful Life for a Markov Failure Time Process," *IMA Journal of Management Mathmatics*, vol. 17, pp. 115-130, 2006.

[13] B. Saha, K. Goebel, S. Poll, and J. Christophersen, "A Bayesian Framework for Remaining Useful Life Estimation," *AIAA Journal*, pp. 96-101, 2007.

[14] C. Boller, "Ways and Options for Aircraft Structural Health Management," *Smart Materials and Structures*, vol. 10, pp. 432–440, 2001.

[15] T. Monnier, "Lamb Waves-based Impact Damage Monitoring of a Stiffened Aircraft Panel using Piezoelectric Transducers," *Journal of Intelligent Material Systems and Structures*, vol. 17, pp. 411-421, 2006.

[16] S. S. Kessler, S. M. Spearing, M. J. Atalla, C. E. S. Cesnik, *et al.*, "Damage Detection in Composite Materials Using Frequency Response Methods," *Composites Part B: Engineering*, vol. 33, pp. 87-95, 2002.

[17] C. Y. Shih, Y. G. Tsuei, R. J. Allemang, and D. L. Brown, "A Frequency Domain Global Parameter Estimation Method for Multiple Reference Frequency Response Measurements," *Mechanical Systems and Signal Processing*, vol. 2, pp. 349-365, 1988.

[18] L. Shi, X. Wang, L. Gang, and L. Zhang, "Wideband Lamb Wave Analysis Based on Continuous Wavelet Transform," *Smart Structures and Systems*, vol. 1, 2005.

[19] N. Xu, S. Rangwala, K. K. Chintalapudi, D. Ganesan, *et al.*, "A Wireless Sensor Network for Structural Monitoring," presented at the Proceedings of the 2nd International Conference on Embedded Networked Sensor Systems, Baltimore, MD, USA, 2004.

[20] J. M. Ko and Y. Q. Ni, "Technology Developments in Structural Health Monitoring of Large-Scale Bridges," *Engineering Structures*, vol. 27, pp. 1715-1725, 2005.

[21] S. Dhar, R. Sethuraman, and P. M. Dixit, "A Continuum Damage Mechanics Model for Void Growth and Micro Crack Initiation," *Engineering Fracture Mechanics*, vol. 53, pp. 917-928, 1996.

[22] P. C. Paris, H. Tada, and J. K. Donald, "Service Load Fatigue Damage -- A Historical Perspective," *International Journal of Fatigue*, vol. 21, pp. 35-46, 1999.

[23] H. Ghonem and S. Dore, "Experimental Study of the Constant-Probability Crack Growth Curves under Constant Amplitude Loading," *Engineering Fracture Mechanics,* vol. 27, pp. 1-25, 1987.

[24] C. R. Farrar and K. Worden, "An Introduction to Structural Health Monitoring," *Philosophical Transactions of the Royal Society A: Mathematical, Physical and Engineering Sciences,* vol. 365, pp. 303-315, 2007.

[25] O. Gnawali, K.-Y. Jang, J. Paek, M. Vieira, *et al.*, "The Tenet Architecture for Tiered Sensor Networks," presented at the Proceedings of the 4th International Conference on Embedded Networked Sensor Systems, Boulder, Colorado, USA, 2006.

[26] W. Staszewski, BollerC. , and T. G. R., *Health Monitoring of Aerospace Structures: Smart Sensor Technologies and Signal Processing* Wiley, 2004.

[27] V. Giurgiutiu, *Structural Health Monitoring: with Piezoelectric Wafer Active Sensors* 2007.

[28] A. M. Sutin, J. A. TenCate, and P. A. Johnson, "Single-Channel Time Reversal in Elastic Solids," *Journal of the Acoustical Society of America,* vol. 116, pp. 2779-2784, 2004.

[29] R. Sicard, "A SAFT Algorithm for Lamb Wave Imaging of Isotropic Plate-like Structures," *Ultrasonics,* vol. 39, pp. 487-494, 2002.

[30] J. K. Van Velsor, "Guided-Wave Tomographic Imaging of Defects in Pipe Using a Probabilistic Reconstruction Algorithm," *Insight - Non-Destructive Testing and Condition Monitoring,* vol. 49, pp. 532-537, 2007.

[31] C. H. Wang, J. T. Rose, and F. K. Chang, "A Synthetic Time-Reversal Imaging Method for Structural Health Monitoring," *Smart Materials and Structures,* vol. 13, pp. 415-423, 2004.

[32] F. Wu, J. L. Thomas, and M. Fink, "Time Reversal of Ultrasonic Fields. Il. Experimental Results," *IEEE Transactions on Ultrasonics, Ferroelectrics and Frequency Control,* vol. 39, pp. 567-578, 1992.

[33] L. Yu, V. Giurgiutiu, and J. R. Kendall, "Omnidirectional Guided Wave PWAS Phased Array for Thin-wall Structure Damage Detection," *SPIE Conference*, San Diego, California, USA, 2007, pp. 652939-12.

[34] X. Zhao, H. Gao, G. Zhang, B. Ayhan, *et al.*, "Active Health Monitoring of an Aircraft Wing with Embedded Piezoelectric Sensor/actuator Network: I. Defect Detection, Localization and Growth Monitoring," *Smart Materials and Structures*, vol. 16, pp. 1208-1217, 2007.

[35] G. Derveaux, G. Papanicolaou, and C. Tsogka, "Time Reversal Imaging for Sensor Networks with Optimal Compensation in Time," *The Journal of the Acoustical Society of America,* vol. 121, pp. 2071-2085, 2007.

[36] E. Kerbrat, C. Prada, D. Cassereau, and M. Fink, "Imaging in the Presence of Grain Noise Using the Decomposition of the Time Reversal Operator," *The Journal of the Acoustical Society of America,* vol. 113, pp. 1230-1240, 2003.

[37] J. E. Michaels, J. S. Hall, and T. E. Michaels, "Adaptive Imaging of Damage from Changes in Guided Wave Signals Recorded from Spatially Distributed Arrays," *SPIE Conference,* San Diego, CA, USA, 2009, pp. 729515-11.

[38] Z. Su, L. Cheng, X. Wang, L. Yu, *et al.*, "Predicting Delamination of Composite Laminates Using an Imaging Approach," *Smart Materials and Structures,* vol. 18, pp. 074002, 2009.

[39] H. Lamb, "On Waves in an Elastic Plate," *Proceedings of the Royal Society of London. Series A, Containing Papers of a Mathematical and Physical Character,* vol. 93, pp. 114-128, 1917.

[40] P. N. T. Wells, "Ultrasound Imaging," *Physics in Medicine and Biology,* vol. 51, pp. R83-R98, 2006.

[41] L. Wang and F. G. Yuan, "Damage Identification in a Composite Plate using Prestack Reverse-time Migration Technique," *Structural Health Monitoring,* vol. 4, pp. 195-211, 2005.

[42] X. Lin and F. G. Yuan, "Damage Detection of a Plate Using Migration Technique," *Journal of Intelligent Material Systems and Structures,* vol. 12, pp. 469-482, 2001.

[43] J. B. Ihn and F. K. Chang, "Pitch-catch Active Sensing Methods in Structural Health Monitoring for Aircraft Structures," *Structural Health Monitoring,* vol. 7, pp. 5-19, 2008.

[44] G. Li, F. G. Yuan, R. Haftka, and N. H. Kim, "Bayesian Segmentation for Damage Image Using MRF Prior," *SPIE Conference,* San Diego, CA, USA, 2009, pp. 72920J-12.

[45] X. Lin and F. G. Yuan, "Experimental Study Applying a Migration Technique in Structural Health Monitoring," *Structural Health Monitoring,* vol. 4, pp. 341-353, 2005.

[46] D. Cassereau and M. Fink, "Time-reversal of Ultrasonic Fields. III. Theory of the Closed Time-Reversal Cavity," *IEEE Transactions on Ultrasonics, Ferroelectrics and Frequency Control,* vol. 39, pp. 579-592, 1992.

[47] M. Fink, "Time Reversal of Ultrasonic Fields. I. Basic Principles," *IEEE Transactions on Ultrasonics, Ferroelectrics and Frequency Control,* vol. 39, pp. 555-566, 1992.

[48] H. W. Park, S. B. Kim, and H. Sohn, "Understanding a Time Reversal Process in Lamb Wave Propagation," *Wave Motion,* vol. 46, pp. 451-467, 2009.

[49] B. Jill and H. Mark, "Lamb Wave Characterization of Corrosion-Thinning in Aircraft Stringers: Experiment and Three-Dimensional Simulation," *The Journal of the Acoustical Society of America,* vol. 126, pp. 103, 2009.

[50] R. K. Ing and M. Fink, "Time-reversed Lamb Waves," *IEEE Transactions on Ultrasonics, Ferroelectrics and Frequency Control,* vol. 45, pp. 1032-1043, 1998.

[51] J. R. Taylor, *An Introduction to Error Analysis: The Study of Uncertainties in Physical Measurements*: University Science Books, 1999.

[52] R. B. Thompson, "A Unified Approach to the Model-Assisted Determination of Probability of Detection," *Material Evaluation,* vol. 66, pp. 667-673, 2008.

[53] J. B. Ihn and F. K. Chang, "Detection and Monitoring of Hidden Fatigue Crack Growth Using a Built-in Piezoelectric Sensor/actuator Network: I. Diagnostics," *Smart materials & structures,* vol. 13, pp. 609-620, 2004.

[54] G. Eggeler, "Microstructural Parameters for Creep Damage Quantification," *Acta Metallurgica et Materialia,* vol. 39, pp. 221-231, 1991.

[55] J. A. Nychka and D. R. Clarke, "Damage Quantification in TBCs by Photo-Stimulated luminescence Spectroscopy," *Surface and Coatings Technology,* vol. 146-147, pp. 110-116, 2001.

[56] Z. Y. Shi, S. S. Law, and L. M. Zhang, "Improved Damage Quantification from Elemental Modal Strain Energy Change," *Journal of Engineering Mechanics,* vol. 128, pp. 521-529, 2002.

[57] F. K. Choy, J. Zhou, M. J. Braun, and L. Wang, "Vibration Monitoring and Damage Quantification of Faulty Ball Bearings," *Journal of Tribology,* vol. 127, pp. 776-783, 2005.

[58] M. Ohtsu and H. Watanabe, "Quantitative Damage Estimation of Concrete by Acoustic Emission," *Construction and Building Materials,* vol. 15, pp. 217-224, 2001.

[59] A. F. Christensen, B. Nyhuus, M. B. Nielsen, and H. Christensen, "Three-Dimensional Anal Endosonography May Improve Diagnostic Confidence of Detecting Damage to the Anal Sphincter Complex," *British Journal of Radiology,* vol. 78, pp. 308-311, 2005.

[60] D. G. Harlow and R. P. Wei, "Probabilities of Occurrence and Detection of Damage in Airframe Materials," *Fatigue & Fracture of Engineering Materials & Structures,* vol. 22, pp. 427, 1999.

[61] J. Kim and N. Stubbs, "Model-Uncertainty Impact and Damage-Detection Accuracy in Plate Girder," *Journal of Structural Engineering,* vol. 121, pp. 1409-1417, 1995.

[62] T. L. Anderson, *Fracture Mechanics: Fundamentals and Applications,* 3rd ed.: CRC Press, 2005.

[63] R. J. Cross, "Inference and Updating of Probabilistic Structural Life Prediction Models," PhD, Department of Aerospace and Engineering, Georgia Institute of Technology, 2007.

[64] J. Lemaitre, "Micro-Mechanics of Crack Initiation," *International Journal of Fracture,* vol. 42, pp. 87-99, 1990.

[65] J. C. Newman, "A Crack Opening Stress Equation for Fatigue Crack Growth," *International Journal of Fracture,* vol. 24, pp. R131-R135, 1984.

[66] J. Gomberg, "The Failure of Earthquake Failure Models," *Journal of Geophysical Research,* vol. 106, pp. 16253-16263, 2001.

[67] A. Shipsha, S. Hallstrom, and D. Zenkert, "Failure Mechanisms and Modelling of Impact Damage in Sandwich Beams - A 2D Approach: Part II - Analysis and Modelling," *Journal of Sandwich Structures and Materials,* vol. 5, pp. 33-51, 2003.

[68] S. S. Kulkarni and J. D. Achenbach, "Structural Health Monitoring and Damage Prognosis in Fatigue," *Structural Health Monitoring,* vol. 7, pp. 37-49, 2008.

[69] S. Mohanty, S. Das, A. Chattopadhyay, and P. Peralta, "Gaussian Process Time Series Model for Life Prognosis of Metallic Structures," *Journal of Intelligent Material Systems and Structures,* vol. 20, pp. 887-896, 2009.

[70] C. R. Farrar and N. A. J. Lieven, "Damage Prognosis: the Future of Structural Health Monitoring," *Philosophical Transactions of the Royal Society A: Mathematical, Physical and Engineering Sciences,* vol. 365, pp. 623-632, 2007.

[71] A. Ray, "Stochastic Measure of Fatigue Crack Damage for Health Monitoring of Ductile Alloy Structures," *Structural Health Monitoring,* vol. 3, pp. 245-263, 2004.

[72] D. E. Adams and C. R. Farrar, "Classifying Linear and Nonlinear Structural Damage Using Frequency Domain ARX Models," *Structural Health Monitoring,* vol. 1, pp. 185-201, 2002.

[73] W. Hwang and K. S. Han, "Cumulative Damage Models and Multi-Stress Fatigue Life Prediction," *Journal of Composite Materials,* vol. 20, pp. 125-153, 1986.

[74] C. A. Bouman and M. Shapiro, "A Multiscale Random Field Model for Bayesian Image Segmentation," *IEEE Transactions on Image Processing,* vol. 3, pp. 162-177, 1994.

[75] C. Carson, S. Belongie, H. Greenspan, and J. Malik, "Blobworld: Image Segmentation Using Expectation-Maximization and Its Application to Image Querying," *IEEE Transactions on Pattern Analysis and Machine Intelligence,* vol. 24, pp. 1026-1038, 2002.

[76] K. Held, E. R. Kops, B. J. Krause, W. M. Wells, III, *et al.*, "Markov Random Field Segmentation of Brain MR Images," *IEEE Transactions on Medical Imaging*, vol. 16, pp. 878-886, 1997.

[77] G. Kuntimad and H. S. Ranganath, "Perfect Image Segmentation Using Pulse Coupled Neural Networks," *IEEE Transactions on Neural Networks,* vol. 10, pp. 591-598, 1999.

[78] J. A. Noble, "Ultrasound Image Segmentation: A Survey," *IEEE Transactions on Medical Imaging,* vol. 25, pp. 987-1010, 2006.

[79] S. D. Olabarriaga and A. W. M. Smeulders, "Interaction in the Segmentation of Medical Images: A Survey," *Medical Image Analysis,* vol. 5, pp. 127-142, 2001.

[80] T. N. Pappas, "An Adaptive Clustering Algorithm for Image Segmentation," *IEEE Transactions on Signal Processing,* vol. 40, pp. 901-914, 1992.

[81] D. L. Pham and J. L. Prince, "An Adaptive Fuzzy C-means Algorithm for Image Segmentation in the Presence of Intensity Inhomogeneities," *Pattern Recognition Letters,* vol. 20, pp. 57-68, 1999.

[82] Y. Zhang, "Segmentation of Brain MR Images Through a Hidden Markov Random Field Model and the Expectation-Maximization Algorithm," *IEEE Transactions on Medical Imaging,* vol. 20, pp. 45-57, 2001.

[83] S. Geman and D. Geman, "Stochastic Relaxation, Gibbs Distributions, and the Bayesian Restoration of Images," *IEEE Transactions on Pattern Analysis and Machine Intelligence,* vol. PAMI-6, pp. 721-741, 1984.

[84] A. H.-S. Ang and W. H. Tang, *Probability Concepts in Engineering Planning and Design*. New York: Wiley, 1975.

[85] M. H. DeGroot, *Optimal Statistical Decisions*. New York,: McGraw-Hill, 1969.

[86] T. E. Michaels, M. Ruzzene, and J. E. Michaels, "Frequency-Wavenumber Domain Methods for Analysis of Incident and Scattered Guided Wave Fields," *SPIE Conference*, San Diego, CA, USA, 2009, pp. 729513-12.

[87] Y. Lu, L. Ye, Z. Su, and N. Huang, "Quantitative Evaluation of Crack Orientation in Aluminium Plates Based on Lamb Waves," *Smart Materials and Structures,* vol. 16, pp. 1907-1914, 2007.

[88] J. F. Claerbout, *Fundamentals of Geophysical Data Processing*: Blackwell Science Inc., 1986.

[89] J.-F. Rivest, P. Soille, and S. Beucher, "Morphological Gradients," San Jose, CA, USA, 1992, pp. 139-150.

[90] G. Qu, S. L. Wood, and C. Teh, "Wafer Defect Detection Using Directional Morphological Gradient Techniques," *Journal on Applied Signal Processing,* vol. 2002, pp. 686-703, 2002.

[91] J. Angulo and J. Serra, "Modelling and Segmentation of Colour Images in Polar Representations," *Image and Vision Computing,* vol. 25, pp. 475-495, 2007.

[92] G. Noyel, J. Angulo, and D. Jeulin, "Morphological Segmentation of Hyperspectral Images," *Image Analysis & Stereology,* vol. 26, pp. 101-109, 2007.

[93] A. Hillerborg, M. Modéer, and P. E. Petersson, "Analysis of Crack Formation and Crack Growth in Concrete by Means of Fracture Mechanics and Finite Elements," *Cement and Concrete Research,* vol. 6, pp. 773-781, 1976.

[94] T.-J. Chuang, "A Diffusive Crack-Growth Model for Creep Fracture," *Journal of the American Ceramic Society,* vol. 65, pp. 93-103, 1982.

[95] E. Castillo and A. Fernández-Canteli, "Crack Growth Models," ed, 2009, pp. 129-157.

[96] V. Tvergaard and J. W. Hutchinson, "The Relation Between Crack Growth Resistance and Fracture Process Parameters in Elastic-Plastic Solids," *Journal of the Mechanics and Physics of Solids,* vol. 40, pp. 1377-1397, 1992.

[97] A. Afaghi-Khatibi, L. Ye, and Y.-W. Mat, "An Effective Crack Growth Model for Residual Strength Evaluation of Composite Laminates with Circular Holes," *Journal of Composite Materials,* vol. 30, pp. 142-163, 1996.

[98] A. Tsurui and H. Ishikawa, "Application of the Fokker-Planck Equation to a Stochastic Fatigue Crack Growth Model," *Structural Safety,* vol. 4, pp. 15-29, 1986.

Appendices

A.1 *K*-means Clustering

A.1.1 Basic of k-means clustering

The *k*-means clustering algorithm is a classification method to divide *n* objects based on their attributes into *k* ($k < n$) partitions, each of which holds similar attribute. The objective it tries to achieve is to minimize total intra-cluster variance, or the squared error function as formulated in Eq. (A-1).

$$V = \sum_{i=1}^{k} \sum_{x_j \in S_i} (x_j - \mu_i)^2 \qquad \text{(A-1)}$$

Where there are *k* clusters S_i, $i = 1, 2, ...k, k \le n$ and μ_i is the centroid or mean value of all the members in each cluster.

K-means clustering procedure can be executed as the following four steps:

1) Randomly select *k* cluster centers, however careful selection of initial clustering center will lead to lesser computation.
2) Assign each object to the cluster centers by calculating the distance between the object and the cluster centers, and the object is assign to the closest cluster center temporarily.
3) Adjust the cluster centers by calculating the mean of all the temporary cluster members for all clusters.
4) Repeat the step 2-3 until the convergence is achieved.

This distance could be defined in various ways such as the subtraction between two scale values, Eucidean distance between two points in 2D or 3D space. The following are two demonstrative examples illustrating how the *k*-means clustering works. The first example is the scale value clustering, and the second example is points clustering in 2D space.

A.1.2 Two illustrative cases

(1) Scale case

One hundred samples with mean value 10 are generated as a scale-value sample pool. *K*-means clustering algorithm are used to category all the samples into two classes, which means k=2. The procedure starts with the initial clustering centers, which can be selected randomly and here the value 1 above and below the mean value (9 and 11) are selected as the clustering centers. Along the *k*-mean clustering procedure, the two cluster centers keep changing and finially converge to stable values, 6.625 and 16.538, as shown in Figure A-2 after 6 iterations.

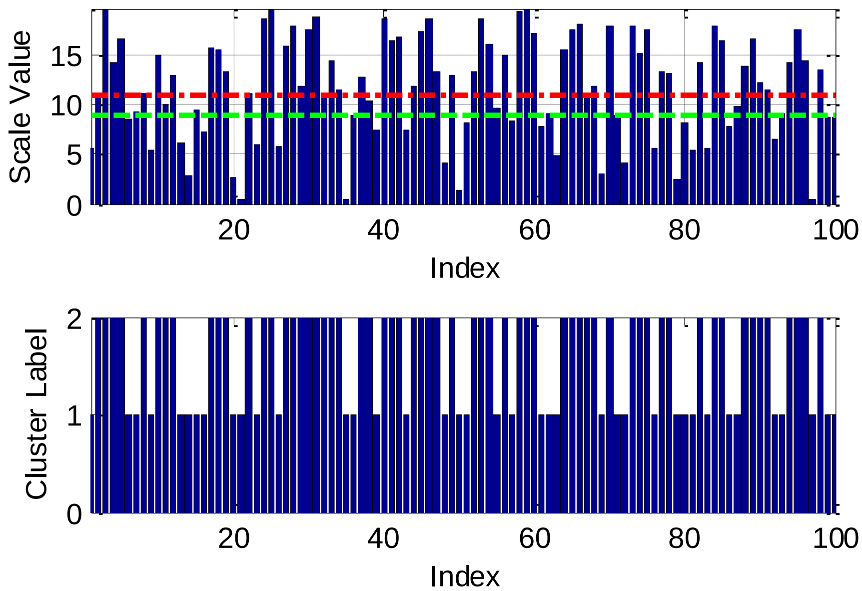

(a) Initial clustering centers for 100 random sample pool

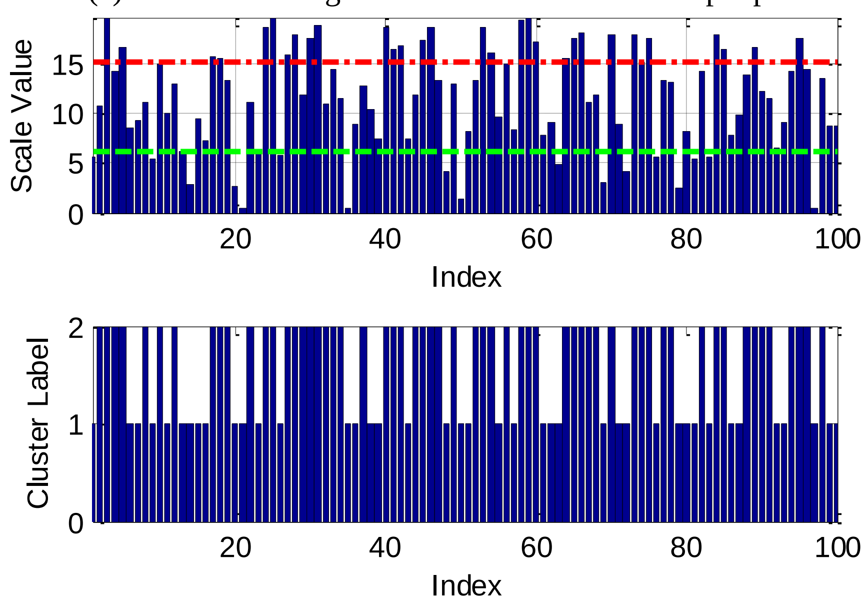

(b) Final clustering centers after 10 interations

Figure A-1. One dimensional scale example of *k*-means clustering.

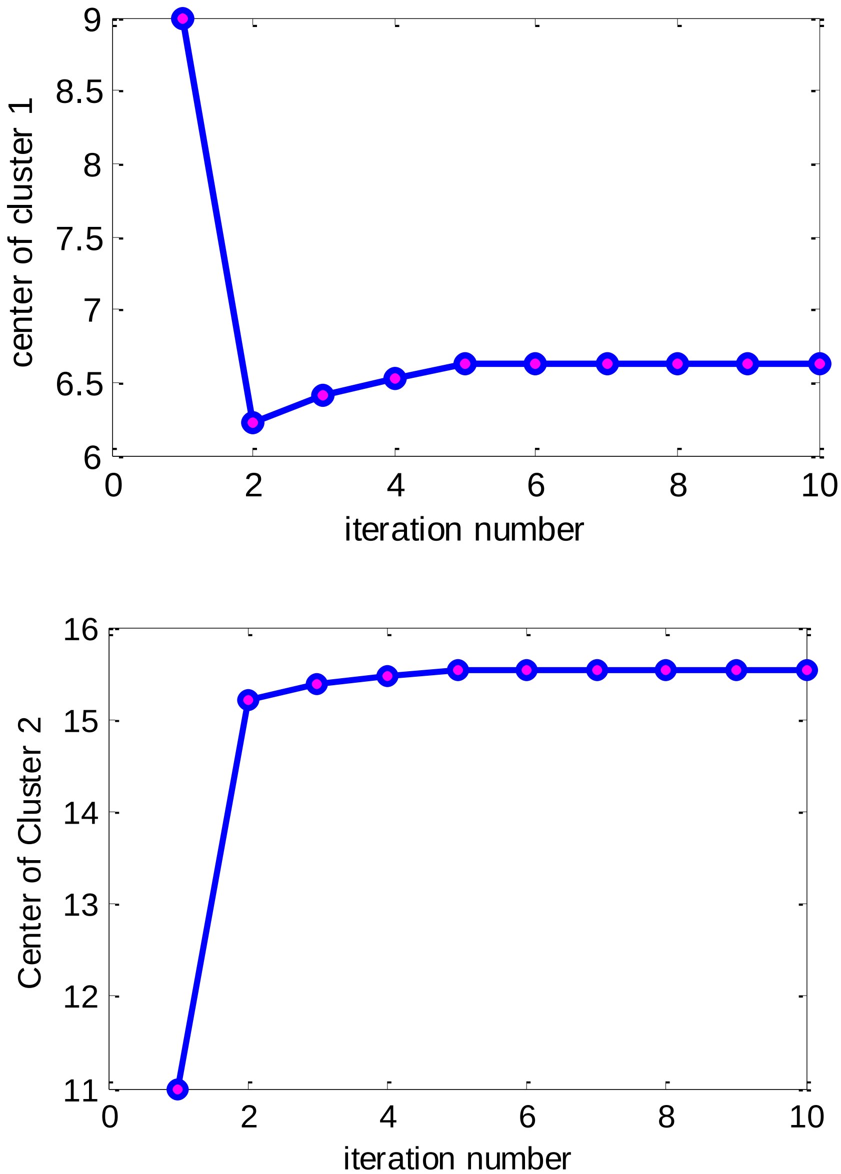

Figure A-2. Cluster center variation correspond to the iteration numbers.

The *k*-means clustering divides the entire data into clusters by calculating the difference between each data and the clustering centers. The cluster center will converge to the final clustering centers. And Table A-1 lists the variation of clustering centers, number of each cluster and the summation of variance of each step.

Table A-1 Parameters in *k*-means example of scale value

Iteration number	**Center of cluster 1**	**Center of cluster 2**	**Member of cluster 1**	**Member of cluster 2**	**Sum of variance**
0	9	11	NA	NA	NA
1	6.218	15.213	39	61	774.657
2	6.415	15.382	41	59	754.679
3	6.521	15.459	42	58	753.410
4	6.625	15.538	43	57	752.472
5	6.625	15.538	43	57	752.472

(2**) Vector case in Cartesian coordinate**

This example demonstrates the *k*-mean clustering procedure of 2D space points. The data points are generated with Eq.(A-2), by which the ideal cluster center of these points should be (-1,-1) and (1,1).

$$\Psi(x,y) \to \begin{cases} x = \mathrm{N}(x)+1 \\ y = \mathrm{N}(y)-1 \end{cases} \tag{A-2}$$

in which N(x) and N(y) are variables with standard normal distribution respectively. The cluster centers are changing with the iterations, although the number in each cluster does not change after the first iteration. The final cluster center and convergence of variance are achieved after 4 iterations. The intermediate results from each step are shown in Figure A-2, in which the red and blue dots are clustered sample points, and the crossed-circles are two clustering centers. Table A-2 lists the variation of clustering centers, number of each cluster and the summation of variance from each iteration. The difference from the first example is that the summation of variance is calculated based on Euclidian distance. The *k*-means clustering method trends to divide random points with spatial repulsion force.

Table A-2. K-means example of Euclidean distance.

Iteration number	Center of cluster 1	Center of cluster 2	Member of cluster 1	Member of cluster 2	Sum of variance
0	(-3,0)	(3,0)	NA	NA	NA
1	(-1.20, -0.77)	(1.17, 0.64)	100	100	241.29
2	(-1.20, -0.96)	(1.17, 0.83)	96	104	228.31
3	(-1.19, -0.98)	(1.16, 0.85)	96	104	227.99
4	(-1.19, -0.98)	(1.16, 0.85)	96	104	227.99

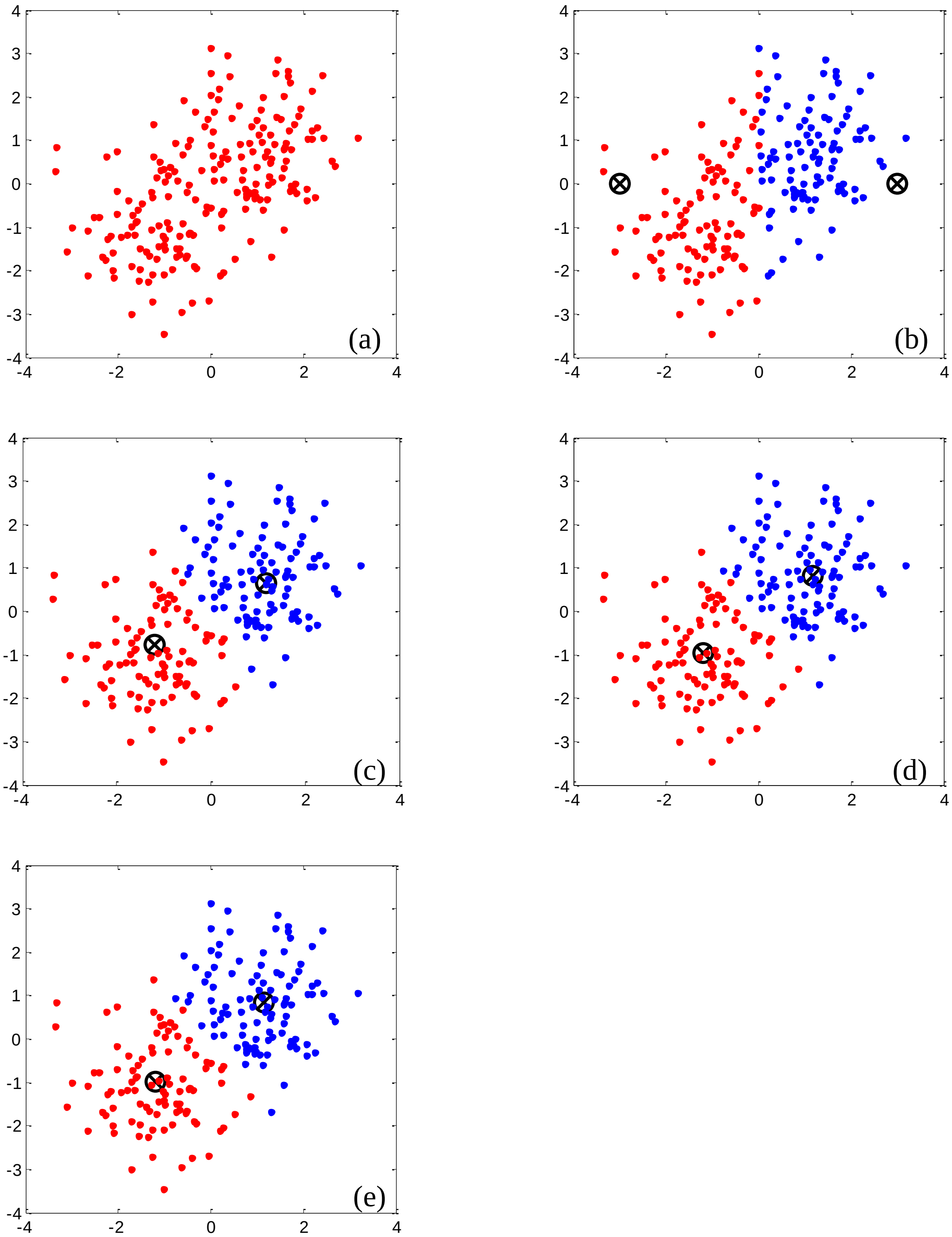

Figure A-3. 2D *k*-means clustering (four loops).